ISSN : 2349-6495(P) | 2456-1908 (O)

International Journal of Advanced Engineering Research and Science

(IJAERS)

An Open Access Peer-Reviewed International Journal

Journal DOI: 10.22161/ijaers

Issue DOI: 10.22161/ijaers.1111

AI PUBLICATIONS

Vol.- 11 | Issue - 11 | Nov 2024

editor.ijaers@gmail.com | editor@ijaers.com | https://www.ijaers.com/

International Journal of Advanced Engineering Research and Science (IJAERS)

(ISSN: 2349-6495(P)| 2456-1908(O))

DOI: 10.22161/ijaers

Vol-11, Issue-11

November, 2024

Publisher

AI Publication

Email: editor.ijaers@gmail.com; editor@ijaers.com

Web: www.ijaers.com

International Editorial/ Reviewer Board

Editor in Chief

- **Dr. Swapnesh Taterh (Chief-Editor),** Amity University, Jaipur, India

Cheif Executive Editor

- **S. Suman Rajest,** Vels Institute of Science, Technology & Advanced Studies, India
  chief-executive-editor@ijaers.com

Associate Editors

- **Dr. Ram Karan Singh,** King Khalid University, Guraiger, Abha 62529, Saudi Arabia
- **Dr. Shuai Li,** University of Cambridge, England, Great Britain

Editorial Member

- **Behrouz Takabi,** PhD, Texas A&M University, Texas, USA
- **Dr. Gamal Abd El-Nasser Ahmed Mohamed Said,** Port Training Institute (PTI), Arab Academy For Science, Technology and Maritime Transport, Egypt
- **Dr. Hou, Cheng-I ,** Chung Hua University, Hsinchu Taiwan
- **Dr. Ebrahim Nohani,** Islamic Azad University, Dezful, IRAN.
- **Dr. Ahmadad Nabih Zaki Rashed,** Menoufia University, EGYPT
- **Dr. Rabindra Kayastha ,** Kathmandu University, Nepal
- **Dr. Dinh Tran Ngoc Huy,** Banking and Finance, HCM, Viet Nam
- **Dr. Engin NAS,** Duzce University, Turkey
- **Dr. A. Heidari,** California South University (CSU), Irvine, California, USA
- **Dr. Uma Choudhary,** Mody University, Lakshmangarh, India
- **Dr. Varun Gupta,** National Informatic Center, Delhi, India
- **Dr. Ahmed Kadhim Hussein,** University of Babylon, Republic of Iraq
- **Dr. Vibhash Yadav,** Rajkiya Engineering College, Banda. UP, India
- **Dr. M. Kannan,** SCSVMV University, Kanchipuram, Tamil Nadu, India
- **José G. Vargas-Hernández,** University of Guadalajara Periférico Norte 799 Edif. G201-7, Núcleo Universitario Los Belenes, Zapopan, Jalisco, 45100, México
- **Dr. Sambit Kumar Mishra,** Gandhi Institute for Education and Technology, Baniatangi, Bhubaneswar, India
- **DR. C. M. Velu,** Datta Kala Group of Institutions, Pune, India
- **Dr. Deependra Pandey,** Amity University, Uttar Pradesh, India
- **Dr. K Ashok Reddy,** MLR Institute of Technology, Dundigal, Hyderabad, India
- **Dr. S.R.Boselin Prabhu,** SVS College of Engineering, Coimbatore, India
- **N. Balakumar,** Tamilnadu College of Engineering, Karumathampatti, Coimbatore, India
- **R. Poorvadevi,** SCSVMV University, Enathur, Kanchipuram, Tamil Nadu, India
- **Dr. Subha Ganguly,** Arawali Veterinary College, Sikar, India
- **Dr. P. Murali Krishna Prasad,** GVP College of Engineering for Women, Visakhapatnam, Andhra Pradesh, India
- **Anshul Singhal,** Bio Instrumentation Lab, MIT, USA
- **Mr. Lusekelo Kibona,** Ruaha Catholic University, Iringa, Tanzania
- **Sina Mahdavi,** Urmia Graduate Institute, Urmia, Iran
- **Dr. N. S. Mohan,** Manipal Institute of Technology, Manipal, India
- **Dr. Zafer Omer Ozdemir,** University of Health Sciences,Haydarpasa, Uskudar, Istanbul, TURKIYE
- **Bingxu Wang,** 2721 Patrick Henry St Apt 510, Auburn Hills, Michigan, United States

Vol-11, Issue-11, November 2024

(10.22161/ijaers.1111)

Detail with DOI (CrossRef)

International Journal of Advanced Engineering Research and Science (IJAERS)
Peer-Reviewed Journal
ISSN: 2349-6495(P) | 2456-1908(O)
Vol-11, Issue-11; Nov, 2024
Journal Home Page Available: https://ijaers.com/
Article DOI: https://dx.doi.org/10.22161/ijaers.1111.1

Production of Artificial Liquid Hydrogen on Mars for Nuclear Thermal Propulsion

Luiza Ramos Ferauche[1], Eleonore Cassandra Poli[2]

[1]Ewgis Research Institute, Community of Madrid, ES
luizarferauche@gmail.com
[2]Department of Materials & Metallurgy, University of Cambridge, UK
ecp40@cam.ac.uk

Received: 07 May 2023,

Receive in revised form: 20 Oct 2023,

Accepted: 28 Sep 2024,

Available online: 05 Nov 2024

***Keywords*— Artificial Liquid Hydrogen, Mars, Nuclear Thermal Propulsion.**

***Abstract*—** *Besides being a renewable fuel, liquid hydrogen would potentiate nuclear thermal propulsion systems on missions to Mars. However, using liquid hydrogen requires carrying large tanks on space trips, which is challenging since rockets have a limited volume available and space related travel costs are mass related, with increased costs for increasing mass. Therefore, producing liquid hydrogen on Mars becomes fundamental for missions back to Earth. Previous research has primarily relied on producing Martian carbon dioxide fuel, however, a pioneer system of artificial liquid hydrogen production on Mars was studied to feasibly make trips to the red planet and lower the costs of space missions. The system involves extracting water from Martian artificial glaciers to produce artificial hydrogen through water electrolysis. Analyzing the system under Martian conditions proved that the model could theoretically be deployed on Mars. With theoretical and practical research, it will be possible to build a safe, effective, and realistic system of artificial liquid hydrogen production on Mars for nuclear thermal propulsion.*

I. INTRODUCTION

The eagerness to leave Earth and explore vast space has challenged the traditional propulsion systems, which lack infrastructure for long-duration space trips. However, the dream of traveling to Mars is taking shape due to an alternative propulsion system called Nuclear Thermal Propulsion (NTP) [1]. NTP engines produce heat by atomic fission, whereas conventional chemical rocket engines add warmth through combustion [2].

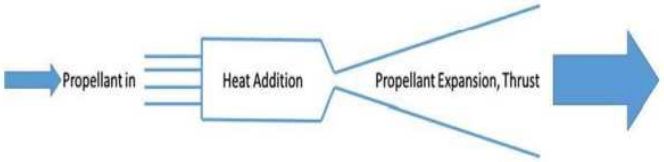

Fig. 1: Basic propulsion system [1]

The studies on NTP began in the United States as an Air Force program to develop nuclear reactors to propel intercontinental ballistic missiles in 1947. Then, from 1958 until 1972, NASA managed a program called Nuclear Engine for Rocket Vehicle Application (NERVA) to explore space. NERVA´s highest thrust and specific impulse (*I*sp) were 890 kN and 835 s, while the J-2 engine used by the Saturn Vat was 1000 kN and 424 s [2]. That

way, NTP promotes faster travel times, almost doubling the specific impulse of the hydrogen-oxygen chemical engines [1].

$$I_{SP}[s] \propto \sqrt{\frac{T_{cbr}[k]}{MW[kg/Kmol]}}$$

Eq. 1: Calculation of Isp from propellant "chamber" temperature (Tcbr) and molecular weight (MW) [1]

Equation n°1 states that low-molecular-weight propellants produce high *I*sp, considering hydrogen the propellant with the lowest molecular weight at 2 kg/kmol. In chemical rockets, hydrogen reacts with oxygen to produce water molecules (18 kg/kmol), whereas NTP uses hydrogen molecules alone, providing higher *I*sp [2]. Moreover, the energy density of hydrogen is 140 MJ/kg, whereas typical solid fuels have an energy density of 50 MJ/kg [3]. Despite the positive results of NTP, the NERVA program ended due to the redirection of government funds to the Vietnam War. However, interest in the Mars mission and NTP system returned in 1989 [2], currently being studied by NASA.

Hydrogen is the primary fuel of NTP engines due to its low molecular weight. It must be stored in its liquid state, with a pressure of 2 atm and a temperature of 20 K, for the propellant tanks to be of an appropriate storage volume [1]. Although it is a sustainable and renewable fuel [4], liquid hydrogen is challenging because of its storage density. It is highly compressible but also much less dense than hydrogen. Therefore, carrying large tanks to store the ideal mass of liquid hydrogen is required for space trips. In addition, the rocket volume increases for long-duration travel like a mission to Mars since more propellant mass is necessary [1]. Considering the limited volume of rockets, the high cost of space trips, and the required mass in low Earth orbit, liquid hydrogen production on Mars becomes crucial for return missions to Earth [5].

II. MATERIALS AND METHODS

2.1 Process of Building Artificial Glaciers

As there is very little gaseous hydrogen on Mars, an alternative way to acquire it would be in liquid form through water (2%) [6]. Considering the low temperatures on the red planet, a solution for its extraction would be to build artificial glaciers. Unlike natural glaciers, artificial glacier pools change states seasonally. They collect and store seasonal water from existing natural glaciers for use later in the year [7] since the meltwater of winters would remain unutilized [8]. Thus, they capture glacial meltwater in October and November, directing it to a specific site through pipes and channels, where it freezes for use in March and April [9]. They do not freeze water from the top down; instead, they are produced by freezing thin layers of water, creating overlapping sheets of ice. Artificial glaciers´ ice storage capacity varies between 17,000 to 23,500 m³ [10]. Engineer Chewang Norphel and his research team developed this technology to solve the unavailability of irrigation water for agriculture in the cold arid deserts of Ladakh, India [8]. However, artificial glaciers do not increase the available water but rather promote the efficient use of water sources [9].

Fig. 2: Structure of an artificial glacier [11]

On Earth, these artificial glaciers are placed at an altitude of nearly 4,000 m in a north-facing valley or at least shaded less than one mile from a village for operational access and maintenance. Their structure includes diversion channels (generally made of concrete or stone masonry), regulator gates, silting tanks/distribution chambers, and retaining pools enclosed by stonewalls.

Diversion channels carry a part of the natural glacier´s meltwater toward a silting tank/distribution chamber or directly into the retaining pools to store ice until spring. Regulator gates control the amount of water that enters the diversion channels at different times of the year. It remains closed in the summer due to the high volume and velocity of the water. Water passes through the distribution chamber after the silting tank and enters the retaining pools through tiny openings in the metal pipes on the side of the distribution chamber closest to the retaining collections. Distribution chambers ensure that water flows into different locations in the retaining pools to freeze uniformly [7].

Mars under the remote supervision of an astronaut crew. The system includes an auger apparatus, a down-hole heating system, a peristaltic pump with a fine mesh filter, and sensors providing data.

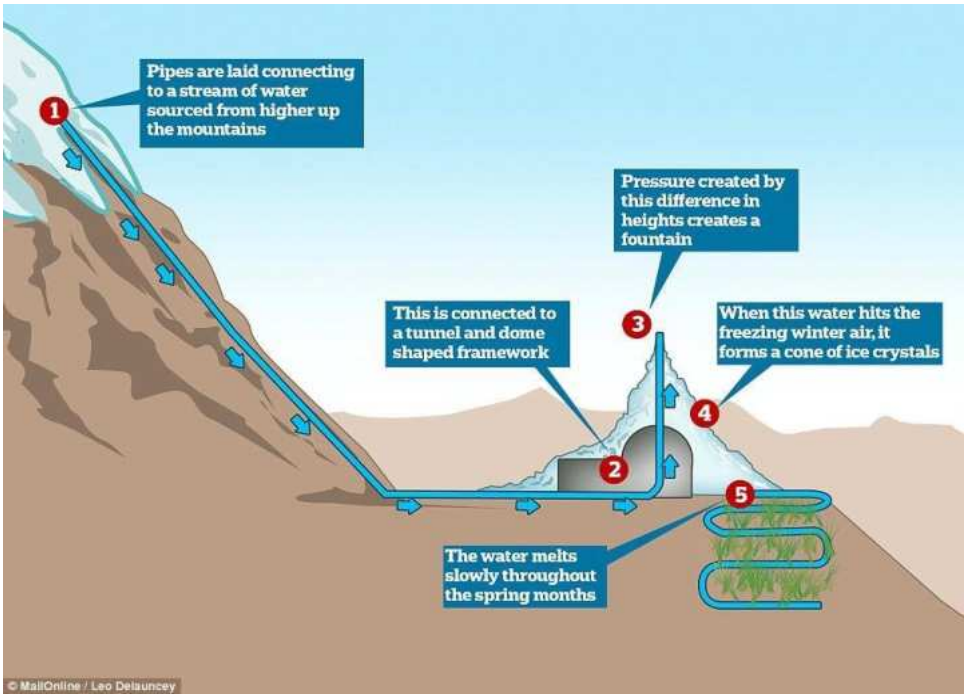

Fig. 3: Process of building artificial glaciers [12]

2.2 Process of Extracting Water

Building artificial glaciers on Mars would rely on extracting water from ice at the poles, vapor in the atmosphere, or liquid in subglacial layers [13]. Unfortunately, Mars has no rainfall due to its thin atmosphere, low temperature, and lack of a magnetosphere [14]. The Earth and Mars conditions are compared in figure 4.

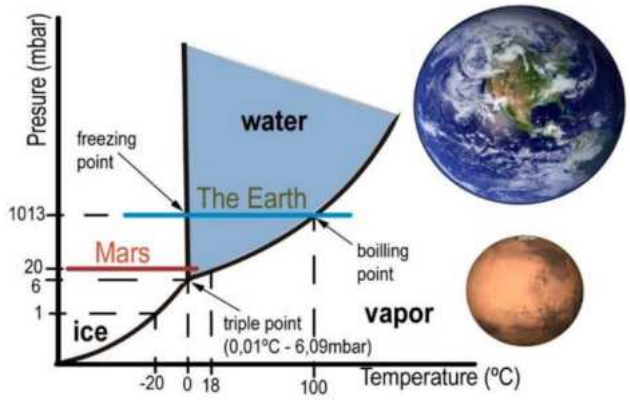

Fig. 4: Relation between pressure and temperature of the water on Earth and Mars [13]

A method for water extraction on Mars is suggested by the MIT HYDRATION III project [15], extracting water from the polar ice. HYDRATION III is an Earth-based analog system that will enable water extraction on

A drill is activated and lowered over the selected place. Controlling the drill bit to produce only the required amount of water is necessary to prevent it from freezing in the hole. The excavation finishes when the drill penetrates nearly 400 mm into the ice. Then, the auger is withdrawn and translated by a distance of 132 mm to position the stack of water

production over the borehole. Inside, the heater melts the ice sheet before the peristaltic pump pumps the meltwater out of the hole. During these two stages, 2 liters of water can be extracted in 25 minutes. Once water production slows down to almost no display, the stack collects the water and is removed [16].

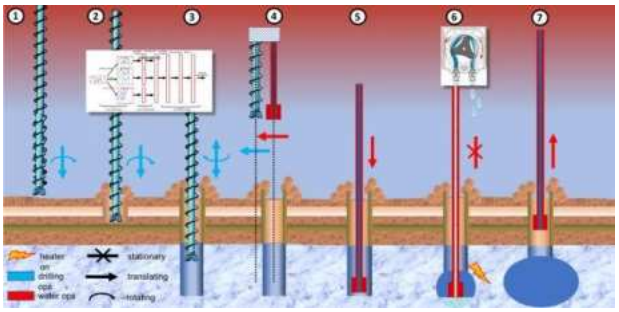

Fig. 5: Water production and extraction through HYDRATION III: (1) position drill bit (2) drill through overburden while collecting sensor data (3) drill through the ice layer and extract the drill bit (4) translate heater stack over the borehole (5) lower heater stack into ice borehole (6) activate the heater and the peristaltic pump to produce and collect water (7) remove the heater stack from the empty borehole [16]

The building of artificial glaciers on the red planet would rely on the water collected through the HYDRATION III system. Due to the shallow temperatures, artificial glacier pools would not change states seasonally, and the process of building them would occur at any time of the year. Thus, diversion channels would carry the water collected toward a silting tank/distribution chamber or directly into the retaining pools. Regulator gates would control the amount of water that enters the diversion channels at all times of the year. Then, the water would pass through the distribution chamber after the silting tank, enter the retaining pools, and freeze [7].

2.3 Process of Artificial Liquid Hydrogen Production

Liquid hydrogen can be produced by condensing gaseous hydrogen from water electrolysis. That way, a required amount of ice should be extracted from artificial glaciers and melted at temperatures above 32° F (0° C) to produce water for electrolysis. The Proton Exchange Membrane Water Electrolysis (PEMWE) is an alternative to producing hydrogen since it emits zero carbon dioxide (CO2), provides fast responses, has a compact design, and has a purity of 99.9% of the hydrogen produced. Water is the reactant dissociated into hydrogen and oxygen [3]. The system consists of a proton-conducting membrane with electrodes containing catalysts on both sides. Thus, the porous transport layers (PTL) and the bipolar plates (flow field for water and gas) clamp the membrane electrode assembly (MEA).

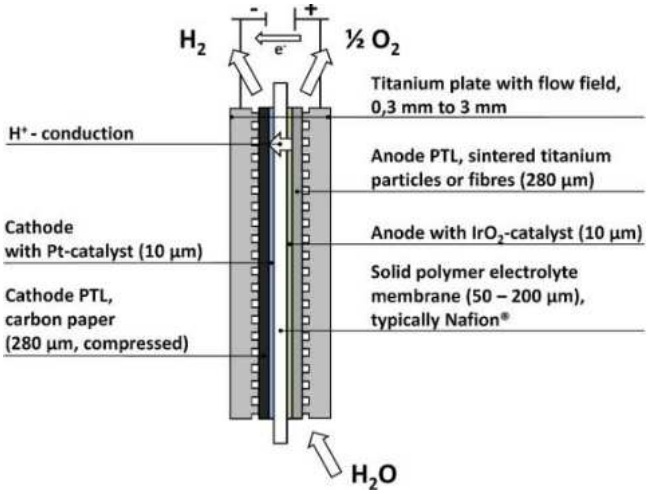

Fig. 6: Parts of a PEMWE cell [17]

The anode side receives deionized water. The cathode produces hydrogen, and the anode produces oxygen. For supplying the overall reaction enthalpy of +286 kJ/mol, the minimum voltage must be 1.48 V.

$$\text{Anode: } H_2O \rightarrow \frac{1}{2}O_2 + 2e^- + 2H^+$$

$$\text{Cathode: } 2H^+ + 2e^- \rightarrow H_2$$

$$\text{Sum: } H_2O \rightarrow \frac{1}{2}O_2 + H_2 \quad (\Delta H^0_{298} = +286\ \text{kJ/mol})$$

Eq. 2: Water electrolysis equation [17]

The protons are conducted from the anode to the cathode through the membrane. At the same time, the electrons are driven through the external electric circuit.

The PEMWE stack is a connection of cells in a series. The system adds upper and lowers current collectors and end plates. The former is made of copper or aluminum for the electrical connection, and the latter is made of aluminum or steel with bolts and sets of stacked flat springs for a uniform compression of the cells [17].

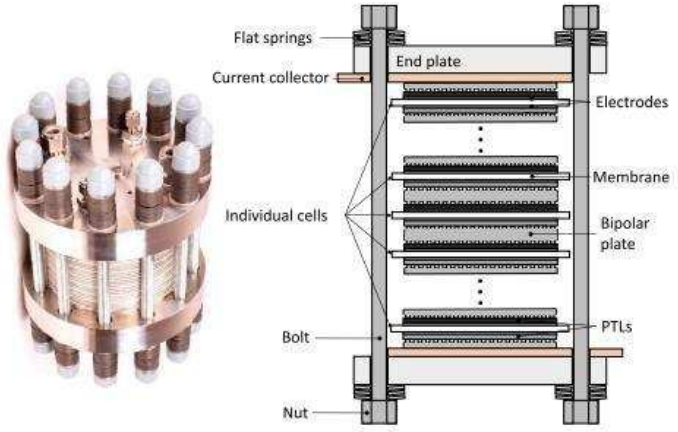

Fig. 7: Parts of a PEMWE stack of the lower power class up to 100 kW [17]

The hydrogen gas produced would be converted to a liquid at -252,87 °C. At -252,87 °C and 1.013 bar, liquid hydrogen has nearly 71 kg/m³ density. At this pressure, 5 kg of hydrogen can be stored in a 75-liter tank to be used later as fuel for nuclear thermal propulsion engines [18].

III. RESULTS

3.1 Process of Building Artificial Glaciers

Artificial glaciers in Ladakh showed they need reinforced masonry walls, stakeholder participation, and dispersing multiple retention walls to increase their effectiveness and durability. They also need glaciercameras to monitor the systems from afar and enclosed pipes, concrete dams, and on/off valves to reduce water losses. However, funding limits improvements.

Future goals include better field data, enhanced collection of and access to hydrological information, a more streamlined design approach, and metal mesh and

earth-buttressed walls to strengthen the pool structure. Nonetheless, researchers must still quantify this technology's benefits and relative cost analysis [7].

3.2 Process of Extracting Water

MIT´s HYDRATION III project showed it could handle a range of regolith substrates and clays. However, some sublimation will occur before sealing the hole on Mars, requiring analysis in adding an inflatable packer to the water stack to seal the borehole before the melting stage. Instead of causing significant water loss, the sublimation will help to clean the spot, purify the water, and reduce operational risk. A scroll compressor and a cold trap will replace the peristaltic pump and filter to pressurize the water vapor and cool the steam into a liquid. The water will be gravity-fed to a collection tank, and the pressure from the scroll compressor will inflate a choke around the rod housing the downhole equipment. However, extensive testing will be required.

The system will likely have a longer life since it has fewer moving parts, and water production is expected to be higher. Other factors to consider when developing the final product are the presence of dust, perchlorates, and regoliths on the red planet, the radiation and launch environment, the reduction of gravity, and the need for simplicity and water filtering [16].

3.3 Process of Artificial Liquid Hydrogen Production

A PEMWE commercial product developed in 1978 presented a higher operating density than other alkaline water electrolysis technologies. Besides, balancing PEMWE plants is much simpler and provides faster responses. Even though the precious metals that are used make it more expensive than alkaline electrolysis, the cost of a PEMWE may reduce to 1/4 of the current price when hydrogen production reaches 1000 kg/d.

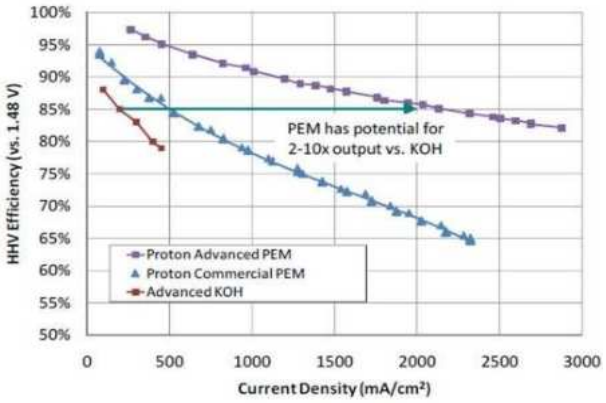

Fig. 8: Comparison of efficiency and operating current density of alkaline electrolysis and PEMWE [3]

Using top catalysts for PEMWE, such as RuO2 and IrO2, can enhance water-splitting performance. Thus, investing in research on electrocatalysts for oxygen evolution reaction (OER) with high activation, durability, and low cost can increase energy efficiency and electrolyzer stability.

Introducing a second cheaper metal, such as Ru, Sn, and Co, can reduce the electrode cost and improve the effectiveness. Along with electrode preparation methods that enhance morphology at the nanoscale, cheaper metals could lead to improvements in electrocatalyst performance toward OER [3].

IV. DISCUSSION

4.1 Process of Building Artificial Glaciers

Results indicate that deploying artificial glaciers on the red planet would achieve the goal of joining the raw material for producing artificial liquid hydrogen [7]. Furthermore, the estimated erosion rates on Mars of 10^{-2}-10^{-1} nm/yr during the Hesperian and Amazonian periods [19] would corroborate their effectiveness. However, it is crucial to be aware that there is no evidence of artificial glacier tests under Martian conditions, which challenges the expectation of their operation. Moreover, they would not reach their high potential for effectiveness since the funding is still a problem to evaluate their benefits and costs and implement enhancements. Thus, tests under Martian conditions and financial support are needed to build safe, durable, accurate, and practical artificial glaciers on Mars [7].

4.2 Process of Extracting Water

Results indicate that the HYDRATION III project would achieve the goal of extracting water from the ice at the poles to build artificial glaciers on Mars, which then in return create more water and ice readily available for hydrogen extraction than drilling alone. Through its simulation, it was defined what structures should be withdrawn, replaced, or added for the project could perform efficiently under Martian conditions. However, it is crucial to be aware that tests were not made to ensure the new structure. Moreover, other factors should be considered while developing the final product. Thus, simulations that test new changes and deployments are needed to create a compelling and accurate final product that will work on Mars [16].

4.3 Process of Artificial Liquid Hydrogen Production

Results indicate that PEMWE would achieve the goal of producing gaseous hydrogen to be converted to a liquid for nuclear thermal propulsion. Besides its plants being easy to balance and providing fast responses, PEMWE

costs may be reduced. However, it is crucial to be aware that PEMWE is currently more expensive than other alkaline water electrolysis technologies and that there is no evidence of PEMWE tests under Martian conditions. Furthermore, using top catalysts, introducing a second cheaper metal, investing in research on electrocatalysts for OER, and using electrode preparation methods that enhance morphology at the nanoscale are necessary to improve PEMWE performance and reduce its costs. Thus, simulations under Martian conditions and scientific research are needed to test improvements and develop an effective, cheap, and feasible PEMWE that will work on Mars [3].

V. CONCLUSION

The research involved preexisting and successful equipment in a single system of liquid hydrogen production on Mars for NTP engines. In addition, it studied the system's applicability, considering adaptive changes in the model for Martian conditions. From a theoretical standpoint, the scientific analysis proved that the system could be deployed on Mars.

With financial support, future studies should closely simulate the system under Martian conditions, considering suggested improvements. Then, with theoretical and practical research, it will be possible to build a realistic system of artificial liquid hydrogen production on Mars for NTP.

ACKNOWLEDGEMENTS

The author gratefully acknowledges her mentor Eleonore Poli for her guidance in the research process and the Ewgis Research Institute for the opportunity.

REFERENCES

[1] Nikitaev, D., & Thomas, L. D. (2021). Seeded Hydrogen in Mars Transfer Vehicles Using Nuclear Thermal Propulsion Engines. *Journal of Spacecraft and Rockets*, *58*(1), 124–133. https://doi.org/10.2514/1.a34722

[2] Aueron, A. L., Thomas, D., & Cassibry, J. (2019). Analytical Modeling of Heat Deposition in Propellant for Nuclear Thermal Rockets. *Journal of Spacecraft and Rockets*. https://doi.org/10.2514/1.a34389

[3] Chi, J., & Yu, H. (2018). Water electrolysis based on renewable energy for hydrogen production. *Chinese Journal of Catalysis*, *39*(3), 390–394. https://doi.org/10.1016/s1872-2067(17)62949-8

[4] Prasad, P., Selvan, D., & Chakraborty, S. (2020). Biosynthetic Approaches towards the Design of Artificial Hydrogen-Evolution Catalysts. *Chemistry: A European Journal*, *26*(55), 12494–12509. https://doi.org/10.1002/chem.202001338

[5] French, J. R. (1989, April 1). *Rocket propellants from Martian resources*. NASA Technical Reports Server (NTRS). Retrieved October 20, 2022, from https://ntrs.nasa.gov/citations/19890050426

[6] Garber, M. (2013, September 27). *Water on Mars: A Brief (and Extremely Long) History*. The Atlantic. Retrieved October 20, 2022, from https://www.theatlantic.com/technology/archive/2013/09/water-on-mars-a-brief-and-extremely-long-history/280066/

[7] Clouse, C., Anderson, N. E., & Shippling, T. (2017). Ladakh's artificial glaciers: climate-adaptive design for water scarcity. *Climate and Development*, *9*(5), 428–438. https://doi.org/10.1080/17565529.2016.1167664

[8] Dar, S. A., Norphel, C., Akhoon, M. M., Zargar, K., Ahmed, N., Yabgo, M. A., Dar, K. A., Hussain, N., Thomas, T. L., Singh, M., Kumar, A., Hussain, S., Kumar, B., & Baba, A. Y. (2017). Man's artificial glacier—a way forward toward water harvesting for pre and post sowing irrigation to facilitate early sowing of wheat in cold arid Himalayan deserts of Ladakh. *Renewable Agriculture and Food Systems*, *34*(04), 363–372. https://doi.org/10.1017/s1742170517000527

[9] Clouse, C. (2014b). Learning from artificial glaciers in the Himalaya: design for climate change through low-tech infrastructural devices. *Journal of Landscape Architecture*, *9*(3), 6–19. https://doi.org/10.1080/18626033.2014.968411

[10] Nüsser, M., Dame, J., Kraus, B., Baghel, R., & Schmidt, S. (2019). Socio-hydrology of "artificial glaciers" in Ladakh, India: assessing adaptive strategies in a changing cryosphere. *Regional Environmental Change*, *19*(5), 1327–1337. https://doi.org/10.1007/s10113-018-1372-0

[11] Selfie, S. (2018, May 9). *Ice Stupas: Artificial glaciers provide fresh water in Ladakh, Himalayas*. Startup Selfie. Retrieved October 24, 2022, from https://www.startupselfie.net/2018/05/09/ice-stupas- artificial-glaciers-provide-fresh-water-ladakh-himalayas/

[12] Collins, T. (2017, July 20). *Artificial glaciers grown in a high altitude desert in India*. Mail Online. Retrieved October 24, 2022, from https://www.dailymail.co.uk/sciencetech/article-4713574/Artificial-glaciers-grown-high-altitude- desert.html

[13] Sobrado, J. M. (2020). Mimicking the Martian Hydrological Cycle: A Set-Up to Introduce Liquid Water in Vacuum. *Sensors*, *20*(21), 6150. https://doi.org/10.3390/s20216150

[14] Williams, M. (2017, February 1). *What is the Weather like on Mars? - Universe Today*. Universe Today. Retrieved October 20, 2022, from https://www.universetoday.com/14941/mars-weather/#:~:text=Due%20to%20its%20thin%20atmosphere%2C%20low%20temperatures%20and

[15] Strickland, A. (2021, December 16). *'Significant amounts of water' found in Mars' massive version of the Grand Canyon*. CNN. Retrieved October 20, 2022, from https://edition.cnn.com/2021/12/16/world/exomars-water-mars-grand-canyon-scn/index.html

[16] Lordos, G., Vanderhout, A. R., Adams, A. B., Alowayed, M., De Filippi, R., Hoffman, J. A., De Weck, O., &

Takahashi, R. (2021). HYDRATION: Mining Water Ice on the Moon and Mars Using Downhole Radiative Heating. In *Earth and Space 2021*. https://doi.org/10.1061/9780784483374.044

[17] Bareiß, K., De La Rúa, C., Möckl, M., & Hamacher, T. (2019). Life cycle assessment of hydrogen from proton exchange membrane water electrolysis in future energy systems. *Applied Energy*, *237*, 862–872. https://doi.org/10.1016/j.apenergy.2019.01.001

[18] *Storing Hydrogen | Air Liquide Energies*. (n.d.-b). Air Liquide. Retrieved October 24, 2022, from https://energies.airliquide.com/resources-planet-hydrogen/how-hydrogen-stored#:~:text=A%20state-of-theart%20technique%20for%20storing%20maximum%20hydrogen%20in

[19] Golombek, M. P., & Bridges, N. T. (2000). Erosion rates on Mars and implications for climate change: Constraints from the Pathfinder landing site. *Journal of Geophysical Research*, *105*(E1), 1841–1853. https://doi.org/10.1029/1999je001043

International Journal of Advanced Engineering Research and Science (IJAERS)
Peer-Reviewed Journal
ISSN: 2349-6495(P) | 2456-1908(O)
Vol-11, Issue-11; Nov, 2024
Journal Home Page Available: https://ijaers.com/
Article DOI: https://dx.doi.org/10.22161/ijaers.1111.2

Fuzzy PID Controller Analysis for the Hexacopter Aircraft Using Simulink Simulation

Jiahui Feng[1], Yuhui Luo[2], Zixian Huang[3], Rueiyuan Wang[4], Rongguei Tsai[5], Raojun Luo[6], Chaoxiong Su[7], Hosheng Chen[*8]

[1,2,3,5,6,7,8]School of Sciences, Guangdong University of Petrochem Technology (GDUPT), Maoming 525000, China
[5]Guangdong University of Science and Technology, China
*Corresponding author

Received: 23 Sep 2024,
Receive in revised form: 25 Oct 2024,
Accepted: 01 Nov 2024,
Available online: 06 Nov 2024

***Keywords*— Hexacopter Aircraft, Unmanned Aerial Vehicle (UAV), Classical PID (Proportion Integration Differentiation) Control, Fuzzy PID Control, Simulink Simulation**

***Abstract*—** *This study aims to investigate the control benefits of rotary wing aircraft systems through the Simulink simulation platform. A hexacopter aircraft is a small unmanned aerial vehicle (UAV) powered by the operation of six rotors, which has important theoretical and practical application value. Firstly, the body structure and working principle of the hexacopter aircraft are proposed. Then, a mathematical model of the hexacopter aircraft is established to support the design of subsequent control strategies. Next, compare the differences between the classical PID controller design and the fuzzy PID controller design methods for aircraft control systems and verify them through simulation experiments. The simulation results show that compared with the classical PID controller, the fuzzy PID controller can stabilize the aircraft at the target position faster when subjected to various types of disturbances and have good practicality, stability, speed, and accuracy. Based on this, future research can further explore the application of other advanced control strategies in aircraft control systems and their prospects in practical engineering.*

I. INTRODUCTION

Nowadays, various aircraft are gradually popularized in various application fields of human beings, such as post-disaster rescue [8, 10], water quality sampling [5], military logistics [11], aerial photography [9], and other fields, playing an important role. With the continuous development of aircraft, the attention to their related products in today's society is gradually increasing. Therefore, more and more different types of aircraft are appearing on the market. The research object of this article, the hexacopter aircraft, is one of its derivative products.

The hexacopter arm of this study is installed according to the layout of a conventional X-shaped body, with the motor components and propeller distributed in the same position. The propeller has a fixed pitch, and although the angle between the rotating plane and the fuselage cannot be changed arbitrarily, the reverse torque can be balanced by changing the direction of adjacent motors. The six motors of the hexacopter control the attitude and altitude changes by changing the speed. Number the motors as M1~M6, and the direction of rotation of the motors is shown in Figure 1. [1,3,4,14,15]

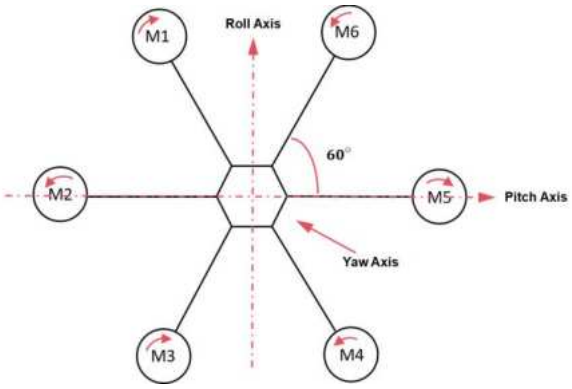

Fig.1 Schematic diagram of the rotational posture of the hexacopter motor

When the six motors of a quadcopter operate in synergy, the aircraft can achieve various motion controls such as roll, pitch, translation, yaw, and hover during flight [7]. The flight control of drones is usually achieved through a built-in flight control system, which calculates and adjusts the rotor speed based on data provided by sensors such as gyroscopes, accelerometers, and compasses to achieve stable flight.

The purpose of this article is to study the motion control system of a hexacopter aircraft, establish mathematical models for the kinematics and dynamics of the hexacopter, and consider the attitude and altitude information of the hexacopter. The main approach is based on the functions of MATLAB software, classical PID control, and fuzzy PID control [2, 6, 12], as well as the anti-interference attitude controller designed with anti-interference control ideas [13]. The mathematical models derived from mathematical and physical theories are imported into Matlab software for simulation, which can effectively test the stability, speed, and accuracy of the six-rotor aircraft system, obtain relevant data, and compare the data of classical PID control and fuzzy PID control to verify the superiority of the fuzzy PID control system in all aspects.

II. ESTABLISH MATHEMATICAL MODEL FOR HEXACOPTER AIRCRAFT

2.1 Coordinate System and Attitude Representation of Hexacopter Drones

The coordinate system of a hexacopter aircraft is divided into a ground coordinate system and an aircraft coordinate system, mainly using a three-dimensional Cartesian coordinate system to define the two coordinate systems of the drone. The ground coordinate system refers to the coordinates of the motion state and spatial position relative to the ground. The X-Y-Z inertial coordinates of the aircraft are taken in the north-east ground direction of the earth and represented by G. The aircraft coordinate system is represented by B, with the center of the aircraft represented by OB. The X-Y-Z of the aircraft coordinate system corresponds to the front right bottom direction of the hexacopter aircraft. The transformation between the ground coordinate system and the aircraft coordinate system is shown in Figure 2.

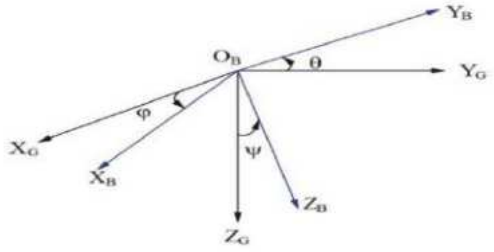

Fig.2: Transformation of Ground Coordinates Systems and Aircraft Coordinate Systems

The rotation angle of the aircraft coordinate system around the X-Y-Z axis of the ground coordinate system can obtain three Euler angles, namely yaw angle φ, roll angle θ, and pitch angle ψ. The Euler angle is commonly used to represent the relationship between the ground coordinate system and the aircraft coordinate system and is an intuitive attitude representation method for UAV. According to Euler's theorem, the rotation of a rigid body around a fixed point is the synthesis of several finite rotations around that point. Therefore, the motion of a rigid body rotating around a fixed point can be decomposed into a series of individual rotations around that point, with the rotation angle being Euler's angle. Thus, the attitude matrix is represented by the product of three basic rotation matrices, making the ground coordinate system and the aircraft coordinate system exactly the same.

When XB rotates around the XG axis, the obtained yaw angle is φ, and the transformation matrix RX (φ) is:

$$R_X(\varphi)=\begin{bmatrix}1 & 0 & 0\\ 0 & \cos\varphi & -\sin\varphi\\ 0 & \sin\varphi & \cos\varphi\end{bmatrix}$$

When YB rotates around the YG axis, the roll angle θ is obtained, and the transformation matrix Ry (θ) is obtained as follows:

$$R_X(\theta)=\begin{bmatrix}\sin\theta & 0 & -\sin\theta\\ 0 & 1 & 0\\ \sin\theta & 0 & \cos\theta\end{bmatrix}$$

When ZB rotates around the ZG axis, the resulting pitch angle is denoted as ψ. The transformation matrix RZ (ψ) is obtained as follows:

$$R_X(\psi)=\begin{bmatrix}\cos\psi & \sin\psi & 0\\ -\sin\psi & \cos\psi & 0\\ 0 & 0 & 1\end{bmatrix}$$

When the hexacopter rotates in the three-axis position during flight, according to Newton's second theorem M=Jω̇, the conversion relationship of angular velocity S=$\begin{bmatrix}\dot{\varphi} & \dot{\theta} & \dot{\psi}\end{bmatrix}$ in the ground coordinate system can be obtained as follows:

$$R(\psi、\theta、\varphi)=\begin{bmatrix}\cos\psi\cos\theta & \cos\psi\sin\theta\sin\varphi-\sin\psi\cos\varphi & \cos\psi\sin\theta\cos\varphi+\sin\psi\sin\varphi\\ \sin\psi\cos\theta & \cos\psi\cos\varphi+\sin\psi\sin\theta\sin\varphi & \sin\psi\sin\theta\cos\varphi-\cos\psi\sin\varphi\\ -\sin\theta & \cos\theta\sin\psi & \cos\theta\cos\varphi\end{bmatrix} \quad (1)$$

2.2 Mathematical Model of Hexacopter Aircraft

The hexacopter aircraft in this article is a mathematical model of the "X" type, but in actual flight, it is subject to uncertain factors such as its own gravity, air resistance, and changes in its own torque. If the flight speed of the aircraft is relatively low, the following assumptions are made to simplify the modeling of the aircraft:

(1) Hexacopter aircraft should be treated as rigid bodies, and the structural elasticity and deformation of the body should be ignored.

(2) The mass and moment of inertia of the aircraft are assumed to be almost constant, only subjected to gravity and propeller tension, ignoring unknown disturbances.

(3) The geometric center of the hexacopter is not only the same as but also coincides with the position of gravity.

(4) Neglecting the influence of the Earth's rotation and revolution on the forces acting on a hexacopter UAV.

According to physical theory, force analysis shows that the lift is mainly affected by the body's gravity and the generated lift. Lift is generated by six motors driving the rotor to rotate, namely F1, F2, F3, F4, F5, and F6. The combined force of a six rotor UAV is F; the angular velocity is ω, the moment of inertia is J, the body weight is m, the velocity is v, and the resultant moment is M. The lift generated by the hexacopter is defined as UZ, the lift coefficient is defined as b, and the arm length is defined as L. Define E=[xyz] T as the position motion vector of the hexacopter body in the ground coordinate system, and Ë as the acceleration vector; $\omega=[p\quad q\quad r]^T$ is the vector on the X-Y-Z axis in the ground coordinate system, and ω̇ is the angular acceleration. When the hexacopter undergoes translational motion during three-axis flight, according to Newton's second law F=ma, it can be obtained that:

$$\begin{bmatrix}\ddot{x}\\ \ddot{y}\\ \ddot{z}\end{bmatrix}=F+\begin{bmatrix}0\\ 0\\ mg\end{bmatrix} \quad (2)$$

When the lift direction generated by the six rotors of a hexacopter is consistent and perpendicular to the ground coordinate ZG direction, then:

$$Uz=F=F1+F2+F3+F4+F5+F6$$
$$=b(\omega_1^2+\omega_2^2+\omega_3^2+\omega_4^2+\omega_5^2+\omega_6^2) \quad (3)$$

According to F=[0 0 -UZ]T as the vector of the total lift of the hexacopter, the mathematical model of the nonlinear kinematics of the hexacopter aircraft is obtained by substituting equations (1) and (2) as follows:

$$\begin{cases}\ddot{x}=-\frac{(\cos\psi\sin\theta\cos\varphi+\sin\psi\sin\varphi)U_z}{m}\\ \ddot{y}=-\frac{(\cos\psi\sin\theta\cos\varphi-\sin\psi\sin\varphi)U_z}{m}\\ \ddot{z}=-\frac{(\cos\theta\cos\varphi)U_z-mg}{m}\end{cases} \quad (4)$$

When the hexacopter rotates in the three-axis position during flight, according to Newton's second theorem M=Jω̇, the conversion relationship of the angular velocity S=$[\dot{\varphi}\quad\dot{\theta}\quad\dot{\psi}]^T$ in the ground coordinate system can be obtained as follows:

$$\begin{bmatrix}\dot{\varphi}\\ \dot{\theta}\\ \dot{\psi}\end{bmatrix}=\begin{bmatrix}1 & \sin\varphi\tan\theta & \cos\varphi\tan\theta\\ 0 & \cos\varphi & -\sin\varphi\\ 0 & \sin\varphi\sec\theta & \cos\varphi\sec\theta\end{bmatrix}\begin{bmatrix}p\\ q\\ r\end{bmatrix}=$$

$$\begin{bmatrix}\frac{p\sin\theta+q\sin\varphi\sin\theta+r\cos\varphi\sin\theta}{\cos\theta}\\ q\cos\theta-r\sin\varphi\\ \frac{q\sin\varphi+r\cos\theta}{\cos\theta}\end{bmatrix} \quad (5)$$

When a hexacopter aircraft performs roll, pitch, and yaw movements during flight, according to the conservation of angular momentum M=Ia, the relationship between the rotational moments M_X, M_Y, M_Z in the x, y, z directions of the body coordinate axes and the rotational inertia I_X, I_Y, I_Z can be analyzed. It can be concluded that:

$$\begin{cases} M_X = I_X\dot{p} + qr\,(I_Y - I_Z) = I_X\ddot{\varphi} + \dot{\theta}\dot{\psi}(I_Y - I_Z) \\ M_Y = I_Y\dot{q} + pr\,(I_Z - I_X) = I_Y\ddot{\theta} + \dot{\psi}\dot{\varphi}(I_Z - I_X) \\ M_Z = I_Z\dot{p} + qp\,(I_X - I_Y) = I_Z\ddot{\psi} + \dot{\theta}\dot{\varphi}(I_X - I_Y) \end{cases} \quad (6)$$

The assumption of a hexacopter aircraft is decomposed from a mathematical model using four independent control channels. The variables for vertical (altitude) control input are defined as U_Z, lateral control input as U_H, pitch control input as U_F, and yaw input as U_P. From this, it can be inferred that the changes between each control channel and lift are:

$$\begin{cases} U_Z = F_1 + F_2 + F_3 + F_4 + F_5 + F_6 \\ U_H = F_1 + F_3 - F_4 - F_6 \\ U_F = F_6 - F_1 + F_3 - F_4 \\ U_P = F_1 + F_2 - F_3 - F_4 - F_5 + F_6 \end{cases} \quad (7)$$

Assuming all assumptions are met and wind resistance is ignored, based on the above calculations, the mathematical model of the theoretical dynamics of a hexacopter aircraft can be obtained as follows:

$$\begin{cases} \ddot{x} = -\frac{(\cos\psi\sin\theta\cos\varphi - \sin\psi\sin\varphi)U_Z}{m} \\ \ddot{y} = -\frac{(\sin\psi\sin\theta\cos\varphi - \cos\psi\sin\varphi)U_Z}{m} \\ \ddot{z} = -\frac{(\cos\theta\cos\varphi)U_Z - mg}{m} \\ \ddot{\varphi} = \frac{lU_H - \dot{\theta}\dot{\psi}(I_Y - I_Z)}{I_X} \\ \ddot{\theta} = \frac{lU_F - \dot{\varphi}\dot{\psi}(I_Z - I_X)}{I_Y} \\ \ddot{\psi} = \frac{lU_P - \dot{\theta}\dot{\varphi}(I_X - I_Y)}{I_Z} \end{cases} \quad (8)$$

The measured parameters of the hexacopter aircraft studied in this article are shown in Table 1.

Table 1 Parameters of Physical Measurement Values for Hexacopter Aircraft

Physical meaning	Parameter symbols	Parameter values
Total mass of hexacopter（kg）	m	6
Gravitational acceleration（m/s^2）	g	9.8
Inertia of rotation around the X-axis（kg·m^2）	I_X	0.6217
Inertia of rotation around the Y-axis（kg·m^2）	I_Y	0.6217
Inertia of rotation around the Z-axis（kg·m^2）	I_Z	1.0845
Hexacopter fuselage radius（1/2 wheelbase，m）	L	0.4025

III. CONTROL SYSTEM DESIGN AND FUZZY LOGIC ESTABLISHMENT

3.1 Control System Design

The control system is generally composed of multiple components, and the flow structure of the control system for a hexacopter aircraft is shown in Figure 3.

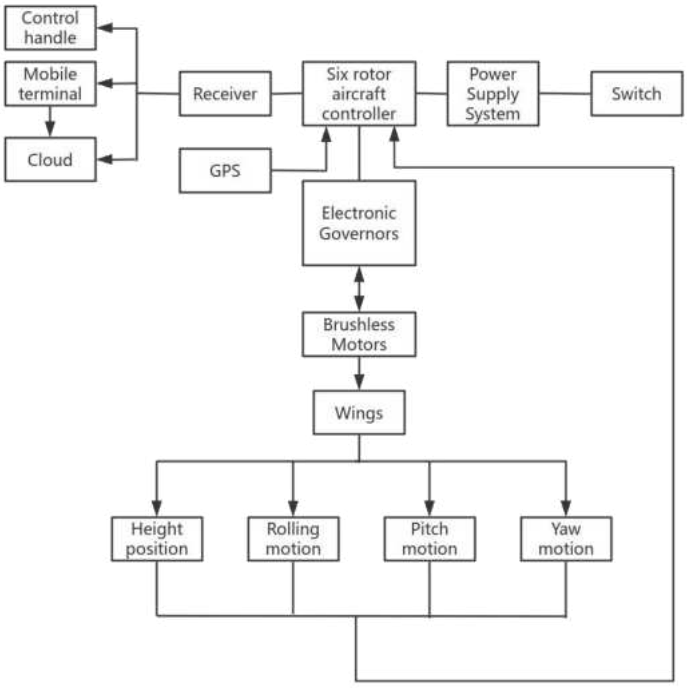

Fig.3 Flow Chart of Control System for Hexacopter Aircraft

3.2 Classic PID Control Principle

The most common control method in general control systems is classical PID control. The classic PID control system is shown in Figure 4.

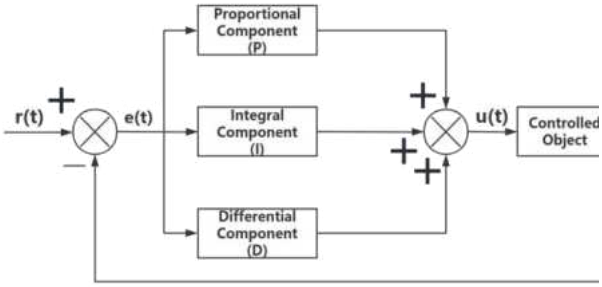

Fig.4 PID Control System Structure Diagram

The expression for the classic PID controller is:

$$e(t) = x(t) - y(t) \qquad (9)$$

$$u(t) = K_P e(t) + K_i \int_0^t e(t)dt + K_d \frac{d}{dt} e(t) \qquad (10)$$

In Figure 4, P, I, D represent proportional control, integral control, and differential control, respectively, corresponding to the proportional coefficient K_P, integral coefficient K_i, and differential coefficient K_d in equation (10). The proportional coefficient is the amplification factor of the difference between the preset value and the feedback value; the larger the proportional coefficient, the higher the adjustment sensitivity. The integral coefficient accumulates the difference between the preset value and the feedback value over time, but there is a significant lag. The differential coefficient is the rate of change of the research object, which can make corresponding adjustments in advance based on the rate of change of the difference.

3.3 PID Controller Transfer Function

After simplifying the model of the hexacopter aircraft, equation (8) can be obtained. The nonlinear equation can be processed to obtain a linearized equation. According to the system construction of this study, the six degrees of freedom of the aircraft can be reduced to four degrees of freedom, so only the height, pitch, roll, and yaw conditions of the vertical aircraft need to be considered during operation. The control variables for these four situations are represented by U_Z as variables perpendicular to X, Y, and Z, U_H as variables for roll, U_F as variables for pitch, and U_P as variables for yaw. The attitude change of the drone during flight is achieved through the variation of control angles ψ, θ, and φ. When $\cos\theta$ and $\cos\varphi$ are approximately 1 during flight, the drone is in hover or low-speed motion. The controller of a hexacopter aircraft

can convert the dynamic model into a state space expression through the LPV method, which is manifested as:

$$\begin{cases} \dot{X} = AX + BU_T \\ Y = CX + DU_T \end{cases} \quad (11)$$

where:

$U_T = [U_Z \quad U_H \quad U_F \quad U_P]^T$

$$\mathrm{X} = \begin{bmatrix} \dot{\mathrm{X}} & \dot{\mathrm{Y}} & \dot{\mathrm{Z}} & \dot{\varphi} & \dot{\theta} & \dot{\psi} & \varphi & \theta & \psi \end{bmatrix}^{\mathrm{T}}$$

$$\mathrm{Y} = \begin{bmatrix} \dot{\mathrm{Z}} & \varphi & \theta & \psi \end{bmatrix}^{\mathrm{T}}$$

$$\mathrm{A} = \begin{bmatrix} 0 & 0 & 0 & 0 & 0 & 0 & 0 & 0 & 0 \\ 0 & 0 & 0 & 0 & 0 & 0 & 0 & 0 & 0 \\ 0 & 0 & 0 & 0 & 0 & 0 & 0 & 0 & 0 \\ 0 & 0 & 0 & 0 & 0 & 0 & 0 & 0 & 0 \\ 0 & 0 & 0 & 0 & 0 & 0 & 0 & 0 & 0 \\ 0 & 0 & 0 & 0 & 0 & 0 & 0 & 0 & 0 \\ 0 & 0 & 0 & 1 & 0 & 0 & 0 & 0 & 0 \\ 0 & 0 & 0 & 0 & 1 & 0 & 0 & 0 & 0 \\ 0 & 0 & 0 & 0 & 0 & 1 & 0 & 0 & 0 \end{bmatrix}$$

$$\mathrm{B} = \begin{bmatrix} \frac{(\cos\psi \sin\theta \cos\varphi + \sin\psi \sin\varphi)}{\mathrm{m}} & 0 & 0 & 0 \\ \frac{(\sin\psi \sin\theta \cos\varphi + \cos\psi \sin\varphi)}{\mathrm{m}} & 0 & 0 & 0 \\ \frac{(\cos\theta \sin\varphi)}{\mathrm{m}} & 0 & 0 & 0 \\ 0 & \frac{\mathrm{L}}{\mathrm{I_X}} & 0 & 0 \\ 0 & 0 & \frac{\mathrm{L}}{\mathrm{I_Y}} & 0 \\ 0 & 0 & 0 & \frac{\mathrm{L}}{\mathrm{I_Z}} \\ 0 & 0 & 0 & 0 \\ 0 & 0 & 0 & 0 \\ 0 & 0 & 0 & 0 \end{bmatrix}$$

$$\mathrm{C} = \begin{bmatrix} 0 & 0 & 1 & 0 & 0 & 0 & 0 & 0 & 0 \\ 0 & 0 & 0 & 1 & 0 & 0 & 0 & 0 & 0 \\ 0 & 0 & 0 & 0 & 1 & 0 & 0 & 0 & 0 \\ 0 & 0 & 0 & 0 & 0 & 1 & 0 & 0 & 0 \end{bmatrix}$$

$$\mathrm{D} = \begin{bmatrix} 0 & 0 & 0 & 0 \\ 0 & 0 & 0 & 0 \\ 0 & 0 & 0 & 0 \\ 0 & 0 & 0 & 0 \end{bmatrix}$$

The transfer function is obtained by applying Laplace transform to equation (11), which is:

$$G_1(s) = C[sl - A]^{-1} + D = \begin{bmatrix} \frac{(1)}{\frac{m}{s}} & 0 & 0 & 0 \\ 0 & \frac{\frac{L}{I_X}}{s} & 0 & 0 \\ 0 & 0 & \frac{\frac{L}{I_Y}}{s} & 0 \\ 0 & 0 & 0 & \frac{\frac{L}{I_Z}}{s} \end{bmatrix}$$

(12)

The brushless motor used in hexacopter drones is a small motor, and the inductance coefficient inside the brushless motor is relatively small. Thus, the inductance coefficient can be ignored. Therefore, using an approximate first-order inertia link brushless motor mathematical model, the transfer function of the brushless motor can be expressed as:

$$G_2(s) = \begin{bmatrix} \frac{0.75}{0.1s+1} & 0 & 0 & 0 \\ 0 & \frac{0.75}{0.1s+1} & 0 & 0 \\ 0 & 0 & \frac{0.75}{0.1s+1} & 0 \\ 0 & 0 & 0 & \frac{0.75}{0.1s+1} \end{bmatrix}$$

(13)

The transfer function of the system is obtained by multiplying equation (11) with equation (12):

$$G(s) = G_1(s)G_2(s) = \begin{bmatrix} \frac{0.75}{sm0.1s+1} & 0 & 0 & 0 \\ 0 & \frac{0.75}{sm0.1s+1} & 0 & 0 \\ 0 & 0 & \frac{0.75}{sm0.1s+1} & 0 \\ 0 & 0 & 0 & \frac{0.75}{sm0.1s+1} \end{bmatrix} \quad (14)$$

According to the actual measured parameters of the hexacopter in Figure 2, the transfer functions of the altitude channel G_Z, roll channel G_H, pitch channel G_F, and yaw channel G_P of the hexacopter aircraft can be obtained as (15) by substituting them into equation (14)

$$\begin{cases} G_z(s) = \frac{0.4025}{6s(0.1s+1)} \\ G_H(s) = \frac{0.4025}{0.6217s(0.1s+1)} \\ G_F(s) = \frac{0.4025}{0.6217s(0.1s+1)} \\ G_P(s) = \frac{0.4025}{1.0845s(0.1s+1)} \end{cases} \quad (15)$$

The input values for defining the attitude angle are ψ_a, θ_a, and φ_a, and the output feedback angles are ψ, θ, and φ. Therefore, the expression for the error values of e_ψ, e_θ, and e_φ is obtained as (16):

$$\begin{cases} e_\psi = \psi_a - \psi \\ e_\theta = \theta_a - \theta \\ e_\varphi = \varphi_a - \varphi \end{cases} \quad (16)$$

By substituting equation (11) into the PID control expression (10), the control law for attitude angle can be obtained as follows:

$$\begin{cases} \ddot{\psi} = K_p e_\psi + K_i \int_0^t e_\psi \, dt + K_d \frac{d}{dt} e_\psi \\ \ddot{\theta} = K_p e_\theta + K_i \int_0^t e_\theta \, dt + K_d \frac{d}{dt} e_\theta \\ \ddot{\varphi} = K_p e_\varphi + K_i \int_0^t e_\varphi \, dt + K_d \frac{d}{dt} e_\varphi \end{cases} \quad (17)$$

3.4 Fuzzy PID Control Principle

When there are nonlinear models and unknown uncertainties in the control of the system, it is necessary to provide more flexible and intelligent control strategies for the system. In fuzzy PID controllers, fuzzy logic is used to dynamically adjust PID parameters, enabling the controller to adaptively adjust based on the real-time state of the system, thereby improving control. The structure of the fuzzy PID control system is shown in Figure 5.

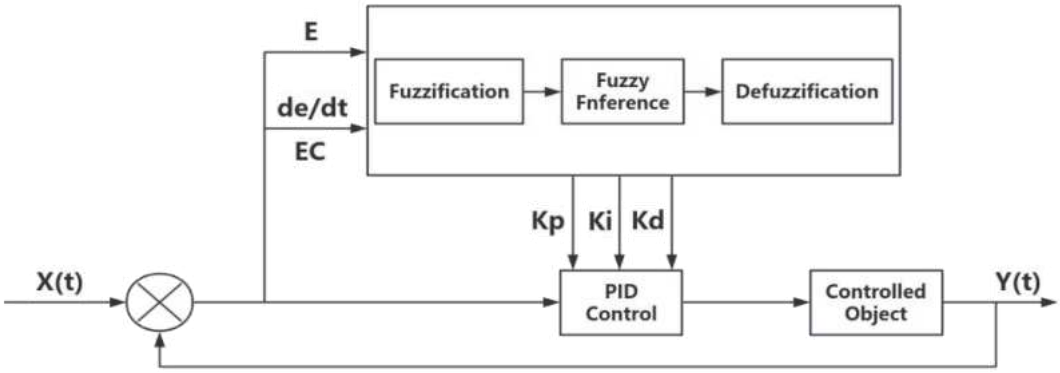

Fig.5 Fuzzy PID Control System Structure Framework Diagram

As shown in Figure 5, fuzzy PID control mainly consists of three steps: fuzzification, fuzzy inference, and deblurring. In a fuzzy PID control system, error E and error rate of change EC are the two inputs of the fuzzy PID controller, while Kp, Ki, and Kd are the three outputs of the controller.

Assuming that the original values Kp1, Ki1, and Kd1 obtained in the classical PID controller are quantized in E and EC, and the correction parameters are determined based on the established fuzzy rules, the resulting correction values are ΔKp, ΔKi, and ΔKd. Finally, they are multiplied by the scaling factor to output Kp, Ki, and Kd. Therefore, the representation of PID parameters is:

$$\begin{cases} K_p = K_{p1} + \Delta K_p \\ K_i = K_{i1} + \Delta K_i \\ K_d = K_{d1} + \Delta K_d \end{cases} \quad (18)$$

Set the input domain of the fuzzy sets E and EC to [-3 3], and their fuzzy subsets are E=ES={negative large, negative medium, negative small, zero, positive small, median, positive large}={NB, NM, NS, ZO, PS, PM, PB}, with a scaling factor of 1. All inputs and outputs use triangular wave-type membership functions. Establish fuzzy rules based on the fuzzy rule table (Table 2).

Table 2 Fuzzy Rules Table for ΔKp, ΔKi, and ΔKd

$K_P\Delta K_i\Delta K_d$		ES						
		NB	NM	NS	Z0	PS	PM	PB
E	NB	PB NB PS	PB NB NS	PM NM NB	PM NM NB	PS NB NB	Z0 Z0 NM	Z0 Z0 PS
	NM	PB NB PS	PB NB NS	PM NM NB	PS NS NM	PS NS NM	Z0 Z0 NS	NS Z0 Z0
	NS	PM NB Z0	PM NM NS	PM NS NM	Z0 NS NM	Z0 Z0 NS	NS PS NS	NS PS Z0
	Z0	PM NM Z0	PM NM NS	PS NS NS	Z0 Z0 NS	NS PS NS	NM PM NS	NM PM Z0
	PS	PS NM Z0	PS PS Z0	Z0 Z0 Z0	PS NS Z0	NS NS Z0	NM PM Z0	NM PB Z0
	PM	PS Z0 PB	Z0 Z0 NS	PS PS PS	PS NM PS	NM PM PS	NB PB PS	NB PB PB
	PB	Z0 Z0 PB	Z0 Z0 PM	NM PS PM	PM NM PM	NM PM PS	NB PB PS	NB PB PB

3.5 Comparison between Classical PID Control and Fuzzy PID Control

Through Simulink simulation, the control effects of classical PID control systems and fuzzy PID systems can be more intuitively observed, leading to more convincing results. Based on the mathematical model of the dynamics of the hexacopter aircraft calculated in the previous text, substitute the simplified and calculated transfer function equation (15) into the Simulink module. Due to the similarity of the roll channel and pitch channel models, these two channels share a simulation model, and three classical PID control models and three fuzzy PID control models are established. The four channel simulations of classical PID control are shown in Figures 6, 7, and 8. In addition, the simulation models of fuzzy PID control built in Matlab are shown in Figures 9, 10, and 11.

Fig.6 Altitude Channel Simulation Diagram of Classic PID Control for Hexacopter Aircraft

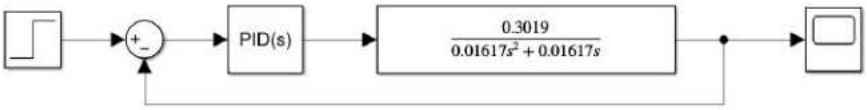

Fig.7 Simulation Diagrams of Roll Channel and Pitch Channel of Classic PID Control for Hexacopter Aircraft

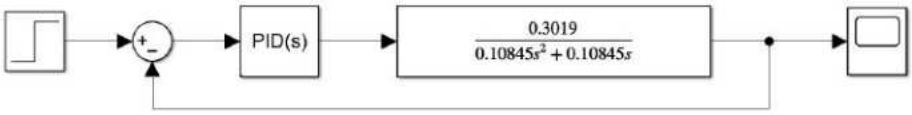

Fig.8 Simulation Diagram of Yaw Channel for Classic PID Control of Hexacopter Aircraft

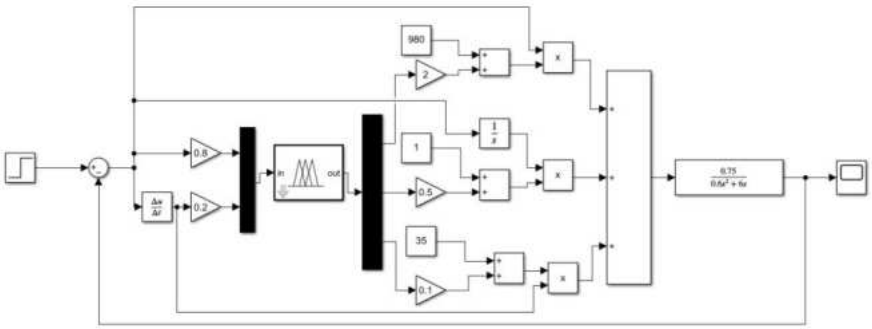

Fig.9 Altitude Channel Simulation of Fuzzy PID Control for Hexacopter Aircraft

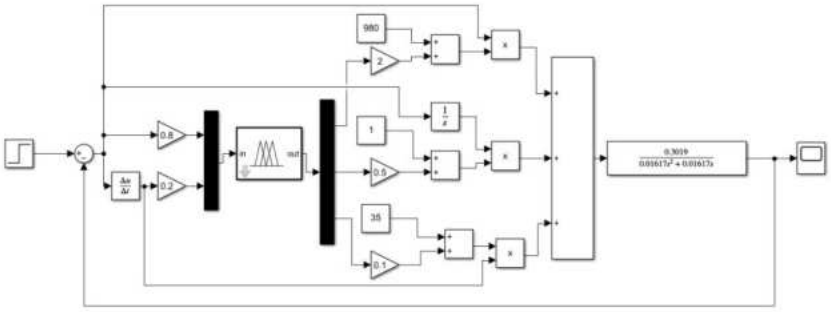

Fig.10 Simulation Diagrams of Roll Channel and Pitch Channel of Fuzzy PID Control for Hexacopter Aircraft

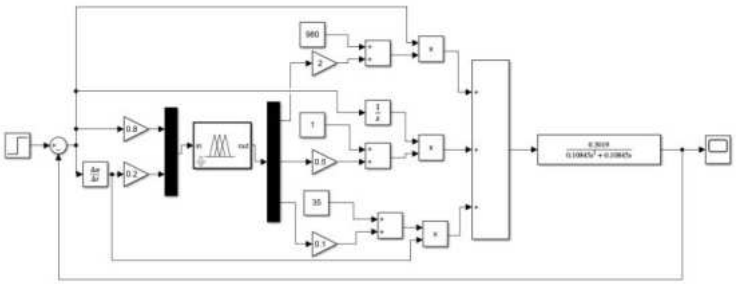

Fig.11 Simulation Diagram of Yaw Channel for Fuzzy PID control of Hexacopter Aircraft

3.6 Hexacopter Simulation Results and Comparison

The K_p, K_i, and K_d values of the classic PID control for the height channel are 180, 12, and 15, respectively; the values of ΔKp, ΔKi, and ΔKd for fuzzy PID control are 1500, 8, and 34, respectively. At a unit-step response, the height channel introduces pulse interference at 0.5 seconds (Figure 12). According to the analysis of the curve changes, it can be seen that fuzzy PID control has a faster response, and under pulse interference, the descent speed is faster. The time to recover stable values is similar, and the time to reach stability is slightly faster than classical PID control.

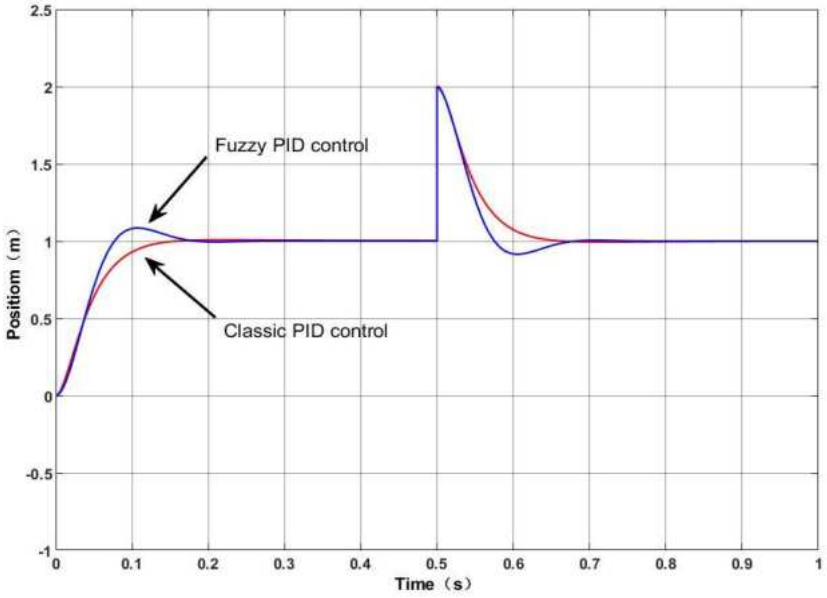

Fig.12 Effect Diagram of Height Channel Pulse Interference Control

The roll channel and pitch channel introduce pulse interference at 0.5 seconds under unit step response (Figure 13). According to the analysis of the curve changes, it can be seen that fuzzy PID control has a faster response, a faster descent speed in the presence of pulse interference, a shorter time required to recover stable values, and a faster time to reach stability than classical PID control.

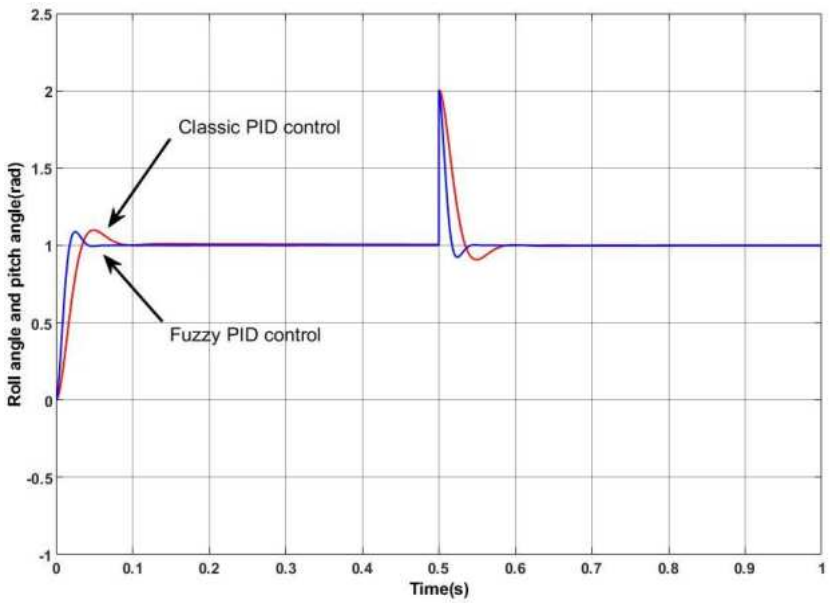

Fig.13 Effect Diagram of Pulse Interference Control for Roll and Pitch Channels

The values of ΔK_p, ΔK_i, ΔK_d for the fuzzy PID control of the yaw channel are 2400, 1, and 38.5, respectively. The yaw channel introduces pulse interference at 0.5 seconds under unit step response (Figure 14). According to the analysis of the curve changes, it can be seen that fuzzy PID control has a faster response. Under pulse interference, its descent speed is faster, and it takes less time to recover stable values. It can be clearly seen that the time to stabilize is faster than classical PID control.

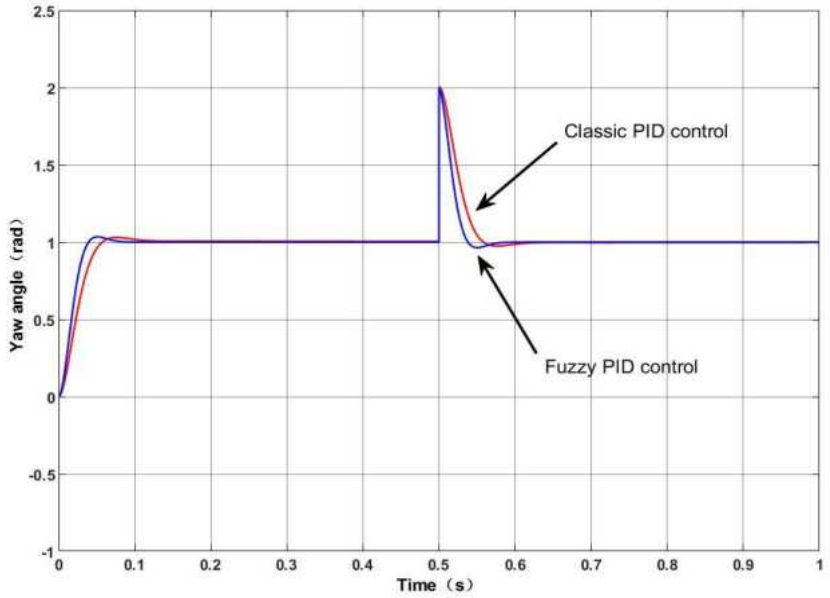

Fig.14 Yaw Channel Pulse Interference Control Effect Diagram

Due to the various uncontrollable factors in the air environment that affect the flight of a hexacopter drone, two continuous signals were selected as interference simulation experiments. Cosine and random numbers were used as input interference signals in Matlab/Simulink simulation, and interference signals were given to the controller at the beginning of the simulation to verify the stability of the control.

According to the simulation curves of the cosine and random interference signals controlled by the height

channel (Figure 15, Figure 16), when the controller is disturbed by the cosine signal, the overshoot of fuzzy PID control is slightly lower than that of classical control, and the adjustment time is shorter. Fuzzy PID can almost be in a relatively stable state, and the response speed of the two is not significantly different. When the controller is disturbed by random signals, although the adjustment time of classical PID control is shorter than that of fuzzy PID control in some areas, the adjustment time of fuzzy PID is shorter than that of classical PID in most areas. From this, it can be seen that the height channel is relatively stable under fuzzy PID control and can maintain stability by adjusting the interference encountered by the drone in a timely manner.

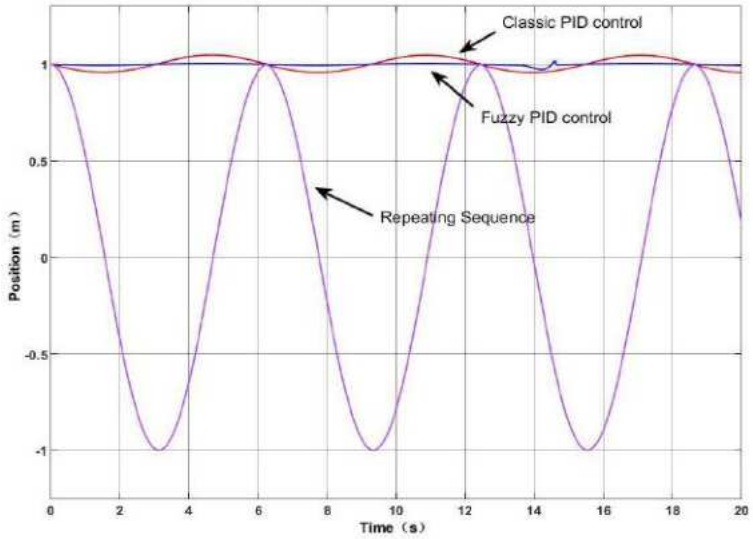

Fig.15 Control Effect Diagram of Cosine Interference Signal in Height Channel

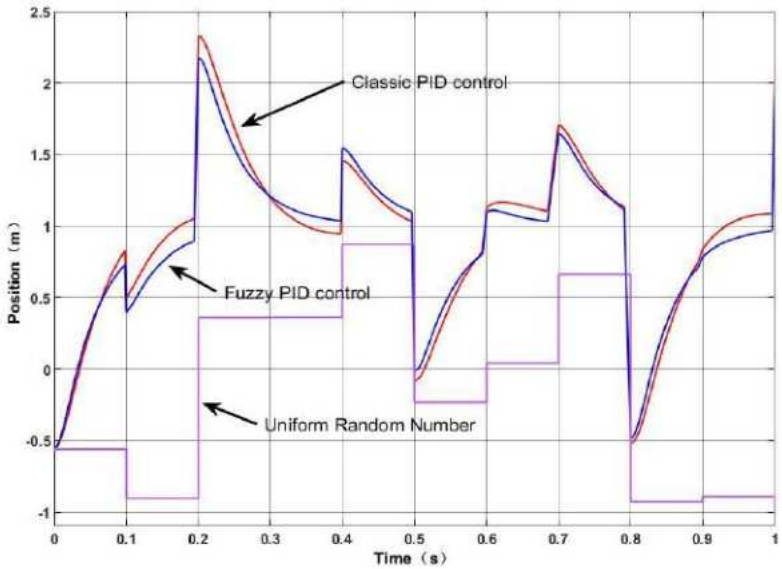

Fig.16 Control Effect of Random Interference Signal in Height Channel

According to the simulated curve changes of cosine and random interference signals for roll and pitch channel control (Figures 17, Figures 18), when the controller is disturbed by cosine signals, the overshoot of fuzzy PID control is slightly smaller than that of classical control, and the adjustment time is slightly shorter. Fuzzy PID can almost be in a relatively stable state, but there may be slightly larger overshoot, and the response speed of the two is not significant. When the controller is disturbed by random signals, fuzzy PID control has slightly lower

overshoot, faster response speed, and significantly shorter adjustment time than classical control, with shorter rise and fall times, quickly maintaining a stable state. From this, it can be seen that the roll and pitch channels are relatively stable in fuzzy PID control with a small amplitude difference due to the interference of cosine signals, while the interference comparison effect of random signals is very obvious.

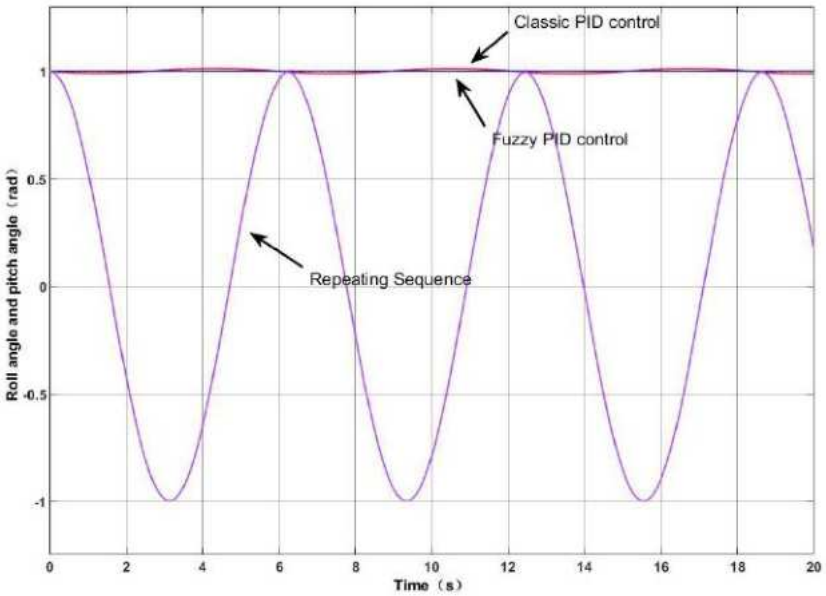

Fig.17 Control Effect Diagram of Cosine Interference Signal in Roll and Yaw Channels

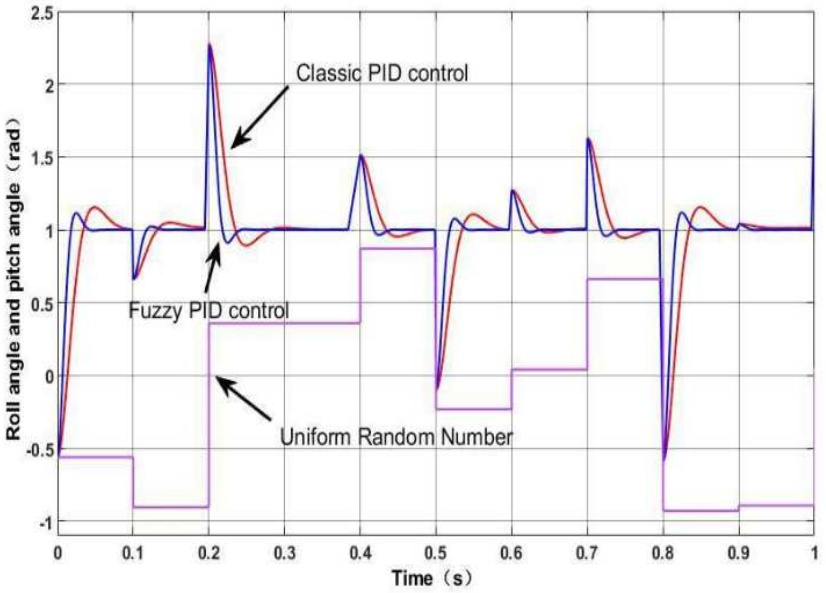

Fig.18 Control Effect Diagrams of Random Interference Signals in Roll and Yaw Channels

According to the simulated curve changes of cosine and random interference signals for yaw channel control input (Figures 19 and Figures 20), when the controller is disturbed by cosine signals, the overshoot of fuzzy PID control is slightly smaller than that of classical control, and the adjustment time is slightly shorter. Fuzzy PID is almost in a relatively stable state, and the response time of the two is not significantly different. When the controller is disturbed by random signals, the overshoot of fuzzy PID control is almost the same as that of classical control, with relatively fast response speed and shorter adjustment time. The rise and fall times are also significantly shorter, which

can quickly maintain a stable state. From this, it can be seen that the yaw channel is relatively stable under fuzzy PID control.

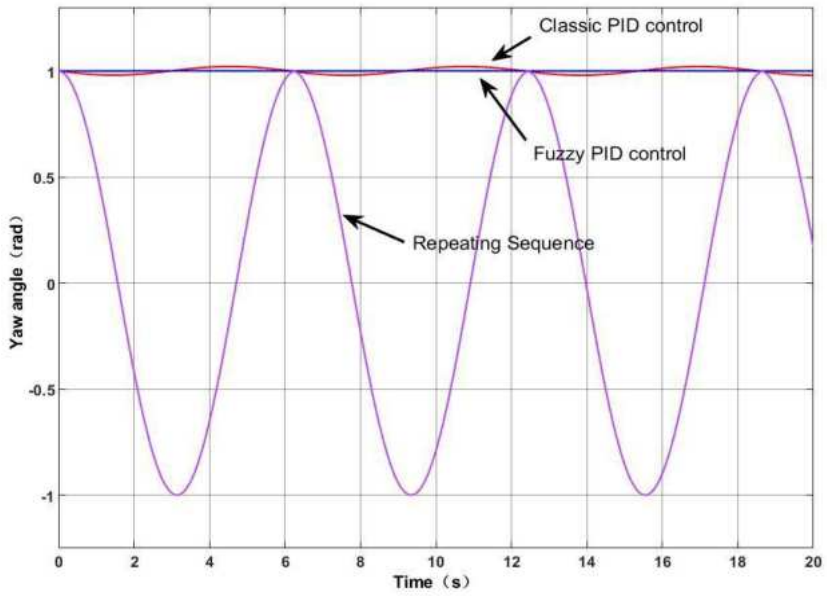

Fig.19 Control Effect Diagram of Cosine Interference Signal in Yaw Channel

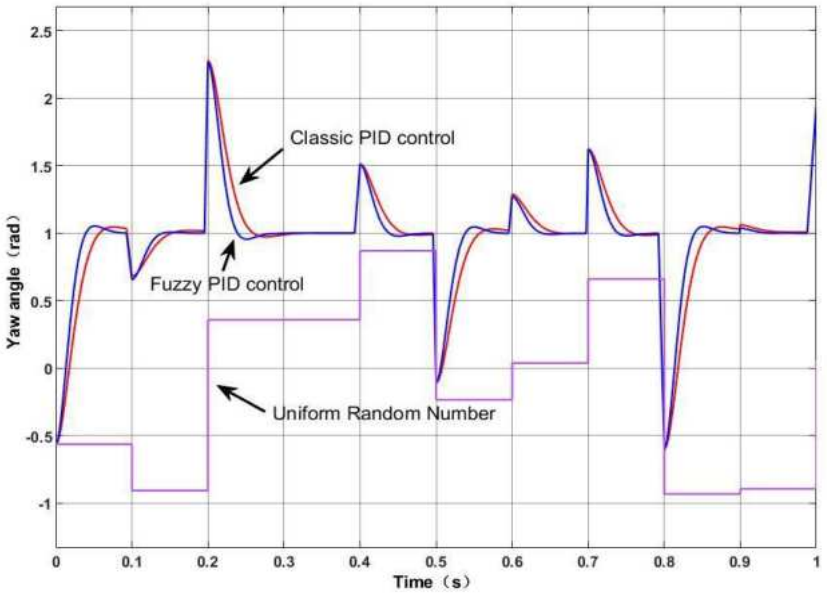

Fig.20 Control Effect of Random Interference Signal in Yaw Channel

IV. CONCLUSIONS

In terms of simulation of hexacopter aircraft under changing real-world conditions, during the actual flight process, drones are subject to many unknown interferences, such as sudden changes in signals, wind resistance, and magnetic fields, which can affect their flight conditions. Therefore, through simulation, problems can be effectively discovered, the design effectiveness of drones can be improved, and the performance of drones can be enhanced.

From the simulation results, it can be seen that if the control system adopts fuzzy PID control, the performance, stability, and anti-interference ability of the hexacopter aircraft are superior to classical PID control. A hexacopter aircraft needs to control the rotation of six motors, and each motor and controller can quickly self-regulate when deviations occur, reducing interference to the drone and

effectively maintaining its ability to fly normally in the air. Overall, the system control is the key to the design of a hexacopter UAVs system. Through the simulation experiment results of this study, ideal scientific data can be obtained to design suitable controllers.

REFERENCES

[1] Alaimo, A., Artale, V., Milazzo, C.L.R. et al., PID Controller Applied to Hexacopter Flight. J Intell Robot Syst. 2014, 73, 261–270. https://doi.org/10.1007/s10846-013-9947-y

[2] Chen, W., Tu, C., Liu, J., Yan, Z., Ren, Y. & Ju, T. Research on Fuzzy PID Flight Control Strategy for Oil Electric Hybrid Hexacopter Unmanned Aerial Vehicle, Journal of Chongqing Jiaotong University (Natural Science Edition). 2024, 43(08):124-132.

[3] Tu, P. Research on fault-tolerant control method for tiltable six rotor unmanned aerial vehicle, East China Jiaotong University. 2023. DOI:10.27147/d.cnki.ghdju.2023.000373.

[4] Lopez-Franco, C., Gomez-Avila, J., Alanis, A.Y., Arana-Daniel, N., and Villaseñor, C., Visual Servoing for an Autonomous Hexarotor Using a Neural Network Based PID Controller. Sensors. 2017, 17(8):1865. https://doi.org/10.3390/s17081865

[5] Tang, M., Fesign of Water Quality Sampling Unmanned Aerial Vehicle System Based on Fuzzy PID, Nanjing University of Information Science and Technology. 2021. DOI:10.27248/d.cnki.gnjqc.2021.000861.

[6] Yao, S., Research on Hardware Control System Design and Attitude Control Optimization of Six rotor Agricultural Patrol Carrier Drone, Xinjiang Agricultural University. 2023. DOI:10.27431/d.cnki.gxnyu.2023.000213.

[7] Zhao, J., Chen, Z., and Zhang, R. Research on Multi rotor Precise Fixed point Hover Control Based on Cascade PID. 2021, 28(08):17-20+30.

[8] Perez-Saura, D., Fernandez-Cortizas, M., Perez-Segui, R. et al. Urban Firefighting Drones: Precise Throwing from UAV. J Intell Robot Syst. 2023, 108, 66. https://doi.org/10.1007/s10846-023-01883-6

[9] Shen, W. Research on pose detection of hexacopter unmanned aerial vehicle based on visual assistance. 2021. DOI: 10.27234/d.cnki.gnhuu.2021.000401.

[10] Yang, B. Research on the Application and Development of Multi rotor Drones in the Rescue Field. Computer Products and Distribution. 2020, (05):130.

[11] Wang, C., Application and Development Trend Analysis of Multi rotor Drones in Military Logistics Field, Winged missile. 2021, (08):56-60. DOI:10.16338/j.issn.1009-1319.20200334.

[12] He, Z. Research on UAV flight control and communication method based on fuzzy adaptive. Wireless Netw. 2024, 30, 6105–6113. https://doi.org/10.1007/s11276-023-03408-3

[13] Li, S., He, D., and Liao, F. Attitude stabilization backstepping control of a six rotor unmanned aerial vehicle based on nonlinear feedforward compensation. 2024, 1-21. https://doi.org/10.16183/j.cnki.jsjtu.2023.652.

[14] Ding, L., Wu, H., and Li, X. Trajectory Tracking Control of Hexacopter Aircraft under Aggregate Interference. 2018, 40(05): 622-628. DOI:10.13374/j.issn2095-9389.2018.05.013.

[15] Chen, Y. Research on fault-tolerant flight control of hexacopter unmanned aerial vehicles, Nanjing University of Aeronautics and Astronautics, 2014.

International Journal of Advanced Engineering Research and Science (IJAERS)
Peer-Reviewed Journal
ISSN: 2349-6495(P) | 2456-1908(O)
Vol-11, Issue-11; Nov, 2024
Journal Home Page Available: https://ijaers.com/
Article DOI: https://dx.doi.org/10.22161/ijaers.1111.3

Challenges and Solutions for Implementing Humanitarian Slaughter of Cattle in Brazil: A Focus on Animal Welfare

Wanessa Soares Luiz Silva, André Reuter Lima Mota, Henrique Lopes Miranda, Felipe Rodrigues Pinto, Livia Santos da Rocha, Elane Soares da Silva Dalmasio, Ledivan Honofrio Marchiori, Lucas Prates da Silva Trindade, Luan Ferreira da Silva, Daniel Rodrigues Silva

Received: 28 Sep 2024,
Receive in revised form: 24 Oct 2024,
Accepted: 02 Nov 2024,
Available online: 08 Nov 2024

***Keywords*— Humane slaughter, Cattle, Animal welfare.**

***Abstract*—** *This study aimed to identify the main obstacles and solutions for the implementation of humane slaughter standards for cattle in Brazil, analyzing the challenges and proposing strategies to improve animal welfare in livestock production. A literature review was used to summarize the existing scientific and regulatory literature on the subject that addresses different aspects of the Brazilian context. The main challenges identified were the lack of adequate infrastructure and equipment, the lack of training programs, cultural resistance to humane practices, insufficient financial incentives and limited monitoring. The lack of appropriate infrastructure and lack of training were identified as direct causes of animal suffering and low quality of the slaughter process, while economic and cultural barriers hinder the acceptance and adoption of the standards. The analysis suggests that the full implementation of these standards requires a systemic approach that integrates financial incentives, awareness campaigns, robust monitoring and government support for training and infrastructure. In conclusion, the study highlights that an effective transition to humane practices depends on coordinated actions that address challenges in an interdependent manner, providing an environment where standards can be applied in a sustainable and ethical manner. The recommendations provide support for the formulation of public policies that promote animal welfare and meet market demands, positioning the Brazilian livestock sector in a competitive and responsible manner.*

I. INTRODUCTION

Animal welfare is an increasingly present topic in academic, social and ethical debates, especially in relation to livestock production. According to Fraser (2024), the concept of animal welfare encompasses ensuring the physical and psychological conditions of animals , so that they can express their natural behavior, avoiding unnecessary suffering.

This field of study has become central due to society's growing awareness of animal rights and the impact of human practices on the lives of these beings, especially with regard to their breeding and slaughter.

In Brazil, one of the largest producers and exporters of beef in the world, animal welfare in livestock farming is a relevant aspect for the sustainability of the production chain and for meeting the demands of international markets, which require increasingly higher

ethical standards (Brasileiro; Souza; Brasileiro- Assing , 2024).

One of the main focuses of these requirements is related to the humane slaughter of cattle, which aims to minimize the suffering of animals during the slaughter process, ensuring practices that reduce stress and pain (Souza; Ribeiro, 2021).

According to Moraes *et al.* (2024), humane slaughter, also called slaughter with humane methods, is regulated by international bodies, such as the World Organization for Animal Health (OIE), and includes a series of procedures to ensure that the slaughter of animals is done ethically, with minimal suffering.

In Brazil, Normative Instruction No. 3 of 2000 of the Ministry of Agriculture, Livestock and Supply (MAPA) establishes the parameters for the handling and slaughter of animals in accordance with welfare standards (Venâncio *et al.,* 2024).

Despite technological and regulatory advances in the livestock sector, the effective implementation of animal welfare practices, especially in relation to the humane slaughter of cattle, still faces significant challenges. In many cases, there is a gap between current regulations and practical implementation in slaughterhouses, resulting in procedures that can cause avoidable stress, pain or suffering to animals. In addition, there is a disparity in information and guidance between different regions and producers, which compromises the uniformity of recommended practices.

In view of this, the research problem that arises is: *What are the main obstacles to the effective implementation of humane cattle slaughter standards in Brazil, and how can animal welfare practices be improved in the context of livestock production?*

This problem seeks to understand the barriers that prevent the full adoption of humane practices in cattle slaughter, analyzing the technical, economic, social and cultural aspects that influence this issue. In addition, it proposes to investigate how the adoption of technologies, team training and awareness of animal welfare can contribute to overcoming these obstacles, promoting more ethical and sustainable livestock farming.

From an academic perspective, this research contributes to the enrichment of the literature on animal welfare, especially with regard to humane slaughter practices. Although studies on the subject already exist, there is a lack of more comprehensive analyses that consider the challenges and solutions specific to the Brazilian reality, one of the largest beef exporters in the world. Thus, this study may serve as a basis for future research that seeks to develop new methodologies, technologies or management strategies that reduce animal suffering and optimize industrial processes.

Scientifically, the research is relevant because it addresses critical issues in modern livestock farming, such as the need to reduce animal suffering without compromising production efficiency. The adoption of humane slaughter practices is directly related to the quality of the meat and the acceptance of the product by consumers, both in the domestic and foreign markets. The research, therefore, offers a significant contribution by providing data and analyses that can assist in the formulation of public policies and the development of more effective regulations for the sector.

In this context, this study aimed to identify the main challenges and solutions related to the implementation of humane cattle slaughter standards in Brazil. This research was developed through a qualitative approach, with an exploratory and descriptive character, based on a literature review. This method is suitable for a detailed and in-depth understanding of concepts, regulations and practices related to animal welfare and humane cattle slaughter. Therefore, the bibliographic study was carried out with the objective of gathering, analyzing and interpreting secondary data extracted from scientific publications.

II. OBSTACLES TO THE IMPLEMENTATION OF HUMANITARIAN SLAUGHTER STANDARDS

Animal welfare is a field of study that assesses the living conditions of animals, considering aspects such as health, behavior and emotions. According to Broom (2011), animal welfare refers to the state of the individual in its attempts to cope with the environment in which it is inserted, encompassing physiological, behavioral and emotional mechanisms. The assessment of welfare uses indicators such as the presence of natural behaviors, absence of pain and disease, as well as behavioral and physiological responses to the environment.

Scientific studies have demonstrated the importance of providing environments that allow the expression of natural behaviors to improve animal welfare. Ceballos and Sant'Anna (2018) highlight that applied ethology, the study of animal behavior, is essential to identify behavioral indicators of welfare, allowing the implementation of practices that meet the specific needs of each species.

The analysis of the obstacles to the implementation of humane cattle slaughter standards in Brazil, as discussed by Carvalho (2021), Roça (2021), Couto, Coqueiro and

Martins (2020), and Almeida (2024), reveals a network of interconnected and mutually reinforcing challenges, creating a complex and restrictive scenario for the adoption of adequate animal welfare practices. The literature indicates that these obstacles form a cycle that perpetuates inadequate practices, indicating that a fragmented approach would be insufficient to deal with the magnitude and interdependence of these problems.

> The methods of humane slaughter and bloody strangulation will differ mainly in relation to stunning, time and techniques during slaughter operations, number of animals slaughtered per day, tools used in slaughter and the efficiency of bleeding, subjects that will be discussed throughout the work (Mendonça; Caetano, 2017, p. 1197).

Animal welfare during slaughter is a central issue addressed by Mendonça and Caetano (2017), as well as in specific regulations, such as Normative Instruction No. 3, of January 17, 2000, of the Ministry of Agriculture, Livestock and Food Supply (MAPA) in Brazil. The regulation differentiates humane slaughter methods and bloodless jugulation mainly in relation to stunning practices, execution time, techniques used, number of animals slaughtered and bleeding efficiency. The regulation highlights the need for procedures that minimize animal suffering, which is consistent with studies that point to the importance of the environment and handling practices for welfare. At the same time, practices such as stunning ensure that animals do not experience pain and distress at the time of slaughter, reflecting a commitment to ethical and sustainable principles discussed in the scientific literature.

Upon critical analysis, it is clear that the regulation is in line with the animal welfare principles discussed by Mendonça and Caetano (2017) and Amaral *et al.* (2019), but its applicability and monitoring may still represent a challenge, especially considering the high volume of daily slaughters in some operations. Effective compliance with these guidelines requires that facilities and staff training be in line with modern practices and adequate equipment, as the absence of such conditions may compromise the expected result for animal welfare.

Legal requirements represent an important advance, but their effectiveness is directly linked to practical implementation and strict control, suggesting a continuous need for adaptation and investment in the sector to achieve the animal welfare standards recommended by scientific studies and established by regulations (Amaral *et al.,* 2019).

The lack of adequate facilities and equipment is a key issue, as highlighted by Carvalho (2021). The lack of appropriate infrastructure for procedures such as effective stunning directly compromises animal welfare and leads to a slaughter process that does not meet humane standards. Without the necessary equipment, animals experience additional stress and suffering, which, in addition to ethical issues, also affects meat quality and slaughterhouse performance.

Carvalho (2021) and Roça (2021) argue that this deficiency is exacerbated by the lack of effective oversight. Even with Ordinance No. 365 of 2021, which establishes guidelines on minimum infrastructure and management, the practical implementation of these standards depends on significant financial resources. This creates a scenario in which small and medium-sized slaughterhouses, which make up a large part of the sector, face difficulties in meeting the required standards due to the limited capacity to mobilize resources.

Couto, Coqueiro and Martins (2020) expand on this analysis by pointing out that adapting to animal welfare standards is financially unfeasible for many producers. The costs involved range from structural reforms in slaughterhouses to the acquisition of high-value equipment, such as stunning guns and adequate restraint systems. This scenario exposes a disparity between legal requirements and the economic reality faced by many producers and slaughterhouses in Brazil. By demanding high standards without providing financing or support mechanisms, the system creates an impasse where full compliance with standards becomes impractical for the smallest participants in the sector, which contributes to the persistence of inadequate and unsustainable practices.

Another crucial aspect is worker training, discussed by Roça (2021), which is essential for the practical application of humane slaughter standards. The lack of training programs leads to the application of ineffective or even cruel practices, which intensify animal suffering and harm the performance of slaughterhouses.

Roça (2021) notes that Normative Instruction No. 12 of 2017 seeks to accredit entities to provide training, but its applicability is limited by the lack of dissemination and national adoption. This scenario indicates that simply establishing guidelines for training is not enough without the support of broad programs and incentives that promote real awareness about animal welfare.

The literature suggests that the lack of training not only derives from the lack of financial resources, but also

from the low perception of the importance of animal welfare in the production chain, as discussed by Almeida (2024). This point implies that training initiatives must be aligned with a cultural and educational effort that reinforces the ethical and practical value of animal welfare.

Almeida (2024) also explores the impact of cultural resistance on the implementation of standards. In many regions, traditional handling and slaughter practices remain resistant to the adoption of more humane methods, becoming an additional challenge to the advancement of animal welfare. This resistance is, in part, the result of a lack of awareness and understanding of the benefits of these practices for both public health and product quality.

Furthermore, Almeida (2024) suggests that in areas where cultural resistance is stronger, the introduction of training programs may be seen as intrusive or unnecessary, reinforcing a view that animal welfare is a dispensable concept in the livestock context. This situation points to the need for educational and informational campaigns that demonstrate the positive impact of humane practices on the quality and commercial value of products.

The literature also indicates that the lack of adequate oversight is a critical element that contributes to the disconnect between legislation and the reality of slaughterhouses, as noted by Carvalho (2021). Insufficient oversight makes animal welfare standards merely formal, with no real impact on the practice of the sector. The scarcity of human and financial resources to carry out consistent inspections and the lack of trained personnel to identify violations make regulations vulnerable to ineffectiveness.

Thus, although formally established, standards do not guarantee a concrete transformation in slaughter practices without solid institutional support. The literature review indicates that, in order to be effective, standards require a support base that includes not only the presence of inspectors, but also the ongoing training of these professionals to ensure effective control.

In summarizing these perspectives, the literature suggests that the challenges are interdependent and that isolated approaches would likely have little impact on improving animal welfare. The lack of infrastructure and equipment, lack of training, cultural resistance and insufficient oversight create a system where barriers reinforce each other, making any significant progress difficult.

The complexity of the obstacles indicates that effective change requires an integrated effort that promotes financial incentives, expands awareness and training programs, and strengthens oversight. This integrated system would act to break the cycle of difficulties, allowing animal welfare practices to advance in a sustainable and ethical manner in the Brazilian context.

III. STRATEGIES TO IMPROVE ANIMAL WELFARE PRACTICES IN LIVESTOCK FARMING

The literature suggests that implementing animal welfare practices requires an integrated set of actions that include training, subsidies, monitoring, awareness-raising and research. Each of these interventions addresses specific aspects of the needs and challenges of the livestock sector, and a critical analysis of these points allows us to identify the complementarity between the recommendations, as well as the challenges and limitations.

First, Silva (2018) emphasizes the importance of comprehensive training programs. The lack of training in the sector is often associated with handling practices that end up causing stress and suffering to animals, whether during transportation or at the time of slaughter. An adequate training program not only provides practical instructions, but also raises awareness among workers and producers about the ethical and economic relevance of animal welfare.

The lack of this awareness, as observed by Almeida (2024), maintains a gap between local practices and market demands. Silva (2018) highlights that training programs also have the potential to improve operational efficiency and product quality, aspects that directly influence access to more demanding markets.

The issue of financial incentives, discussed by Lotti and Junior (2023), emerges as a response to the economic challenges faced by small and medium-sized producers. These authors argue that, without financial support, improvements in infrastructure and equipment to meet animal welfare standards become unfeasible for a large part of the sector. This point of view complements Silva's (2018) analysis by suggesting that, without incentives, training alone would not be enough.

Lotti and Junior (2023) reinforce that subsidies and credit lines enable compliance with standards, but also encourage a gradual change in the production culture, aligning with the objective of creating a more sustainable system. However , these authors also indicate that the impact of subsidies depends on efficient allocation and a clear fiscal policy, since insufficient or poorly targeted incentives could increase disparities between large and small producers.

Furthermore, Mendes and Martins (2022) highlight the importance of a robust monitoring system. Without effective monitoring, animal welfare standards

tend to lose their practical effect, becoming mere recommendations without consistent application. The literature suggests that monitoring is not just a matter of control, but an educational element that reinforces the value of established standards.

Mendes and Martins (2022) argue that a more rigorous inspection system could correct irregularities, promote compliance with standards, and educate stakeholders about the importance of animal welfare. However, implementing effective inspection faces logistical and financial obstacles, especially in remote regions where coverage may be patchy. Their analysis suggests that inspection needs to be accompanied by an incentive structure so that producers feel motivated to adhere to recommended practices.

Raising awareness among the public and those involved in the sector, as mentioned by Fraser (2024), is an essential measure to consolidate animal welfare as a cultural value. Cultural resistance, often observed in the livestock sector (Almeida, 2024), can be mitigated with campaigns that demonstrate the benefits of humane practices not only for animals, but also for producers and consumers.

Fraser (2024) emphasizes that awareness about animal welfare is linked to the image of the sector, since the demand for ethical products is growing both in the domestic and international markets. Analysis of these data suggests that educational campaigns could improve the acceptance of animal welfare standards and position Brazilian livestock farming in more demanding markets, expanding its economic reach.

Finally, Couto, Coqueiro and Martins (2020) argue that investing in research adapted to regional realities is a long-term strategy to sustain animal welfare practices. They note that management practices appropriate in one region may be ineffective or inadequate in others, due to climatic, structural and cultural variations.

Research enables the creation of specific solutions for the country's diverse realities, allowing animal welfare standards to be effectively implemented in different contexts. Couto, Coqueiro and Martins (2020) also suggest that innovation can facilitate the adoption of low-cost practices, which would be particularly useful for small producers facing financial constraints. In this sense, research can be seen as a tool that complements subsidies and incentives, enabling a gradual and more accessible transition to humane practices.

Therefore, it is clear that a critical analysis of the literature reveals that the success of animal welfare practices depends on a joint effort, where training, financial incentives, monitoring, awareness and research complement and reinforce each other. The isolated implementation of any of these strategies would probably have a limited impact, given the complexity of the challenges faced by the sector.

The literature suggests that the combination of these strategies creates an environment where animal welfare standards can be effectively enforced, promoting more ethical, sustainable and competitive livestock production.

IV. FINAL CONSIDERATIONS

Throughout this literature review, multifaceted, interconnected and structural challenges were identified that hinder the full implementation of animal welfare standards in cattle slaughter. The study also aimed to identify these challenges and propose possible solutions, an objective that was achieved through a critical analysis of the literature and practices adopted in Brazil.

The main barriers identified were categorized into aspects of infrastructure, worker training, cultural barriers, lack of financial incentives and insufficient monitoring. The lack of appropriate facilities and equipment was identified as a significant obstacle, since many slaughterhouses lack the resources to adapt their spaces and technologies to humane slaughter standards.

The lack of adequate infrastructure causes suffering to animals, compromising the welfare principles that these standards seek to ensure. To address this issue, we suggest structured investment and government support that will allow smaller slaughterhouses to adapt to the requirements in a viable and sustainable manner.

Another important challenge identified was the lack of training and capacity building for workers. Although Brazilian legislation includes the need for training in humane animal handling, its implementation is limited by the lack of comprehensive programs and specific resources to ensure compliance across the country. Without this training, workers are left without the necessary guidance to carry out appropriate procedures, resulting in animal suffering and detriment to product quality.

This aspect is reinforced by the need for cultural change, as resistance to new practices and values focused on animal welfare is observed in several regions of Brazil, where traditional management methods prevail.

The financial issue also stood out as an obstacle to the implementation of humane slaughter standards. Many producers, especially small and medium-sized ones, face difficulties in making investments, making full compliance with the standards unfeasible. The solution to this obstacle involves public policies that offer subsidies, credit lines and

tax incentives so that these producers can implement the necessary changes.

Insufficient monitoring was another key obstacle identified. Without rigorous and ongoing monitoring, humane slaughter standards become merely formal guidelines with little practical application. In order for the standards to be effectively enforced, it is necessary to increase the resources allocated to monitoring and ensure that inspectors are well trained to identify and correct irregularities.

Finally, the study presented some recommendations for improving animal welfare practices in Brazilian livestock production. In addition to financial incentives and monitoring, the study emphasized the importance of awareness campaigns that promote a new mindset regarding animal welfare. These campaigns could highlight not only the ethical benefits but also the positive economic impacts associated with compliance with humane slaughter standards, especially in a scenario where the consumer market, both nationally and internationally, values products that respect animal welfare.

In response to the research question, it is concluded that the effective implementation of humane slaughter standards in Brazil is hindered by a combination of economic, cultural, structural and operational challenges. The literature suggests that only an integrated approach, which includes financial support, training, monitoring and awareness, will be able to overcome these obstacles and promote an effective transition to sustainable and ethical animal welfare practices.

The study's objective – to identify the main challenges and solutions for implementing humane slaughter standards in Brazil – was successfully achieved. The literature review allowed us to map the main problems and identify possible solutions, offering a broad and well-founded view of animal welfare practices in the Brazilian livestock production sector.

This analysis could serve as a basis for future investigations and public policies aimed at strengthening animal welfare in Brazil, pointing out ways for the country to adopt practices that respect the principles of humanity and efficiency in the slaughter of cattle.

REFERENCES

[1] ALMEIDA, Bernardus Kelner Carvalho de et al. Animal welfare in beef cattle: literature review. Brazilian Journal of Health Review , vol. 7, no. 1, p. 3642-3653, 2024.

[2] AMARAL, Jackson Barros do et al. Humane slaughter and stunning in cattle from the perspective of forensic veterinary medicine: Review. Pubvet , v. 13, p. 148, 2019.

[3] BRAZIL. Normative Instruction No. 3 of January 17 , 2000. Provides for the technical regulation of stunning methods for the humane slaughter of butcher animals. Ministry of Agriculture and Food Supply, 2000.

[4] An approach to the financial impact of promoting animal welfare in cattle production: ... the financial impact of promoting animal welfare in cattle production . Coopex Magazine . , v. 15, no. 02, p. 4882-4903, 2024.

[5] BROOM, Donald M. Animal welfare. Animal Behavior , v. 2, p. 457-482, 2011.

[6] CARVALHO, Camila Lopes et al. Animal welfare of cattle and pigs at slaughter: ordinance 365. Science and animal health , v. 9, n. 2, p. 142-161, 2021.

[7] CEBALLOS, Maria Camila; SANT'ANNA, Aline Cristina. Evolution of animal welfare science: A brief review of conceptual and methodological aspects. Academic Journal of Animal Science , v. 16, p. 1-24, 2018.

[8] COUTO, Luzia Almeida; OUZA COQUEIRO, Jéssica S. Ouza ; MARTINS, Natalia Cristina Gonçalves. Animal welfare in beef cattle farming: a systematic review. Profiscientia , n. 14, p. 176-193, 2020.

[9] FRASER, David. Understanding Animal Welfare: science in its cultural context . Eduel , 2024.

[10] LOTTI, Juliana Tamires; JUNIOR, Edemar Ferrarezi. ANIMAL WELFARE IN BEEF CATTLE PRODUCTION: a bibliographic review. Interface Tecnológica Journal , v. 20, n. 2, p. 690-699, 2023.

[11] MENDES, Luiz Gustavo Ribeiro; MARTINS, Athila Damasceno. Rotational pasture management in beef cattle farming with emphasis on animal welfare: literature review. Facit Business and Technology Journal , v. 1, n. 37, 2022.

[12] MENDONCA, Pamela Stéfani Melo; CAETANO de Oliveira, Graciele Araújo. Slaughter of cattle: Considerations on humane slaughter and bloody jugulation . Pubvet , v. 11, p. 1188-1297, 2017.

[13] MORAES, Fernanda Jacobus et al. Welfare in pre-slaughter and humane slaughter management and quality characteristics of beef: a literature review. Brazilian Journal of Animal and Environmental Research , vol. 7, no. 2, p. e70051-e70051, 2024.

[14] ROÇA, Roberto de Oliveira. Humane slaughter of cattle. Journal of Continuing Education in Veterinary Medicine and Animal Science of CRMV-SP , v. 4, n. 2, p. 73-85, 2001.

[15] SILVA, Daniel Ferreira da. Good animal welfare practices in beef cattle production: review. Undergraduate Course Completion Work—University of Brasília, School of Agronomy and Veterinary Medicine. 2018.

[16] SOUZA, Suellen da Cunha; RIBEIRO, Laryssa Freitas. Application of animal welfare and humane slaughter of cattle to ensure meat quality. GeTeC Journal , v. 10, n. 28, 2021.

[17] VENANCIO, Salete Andrade et al. Assessment of animal welfare in pre-slaughter and slaughter of cattle in a slaughterhouse in the Purus-Acre region. Brazilian Journal of Animal and Environmental Research , vol. 7, no. 2, p. e69084-e69084, 2024.

International Journal of Advanced Engineering Research and Science (IJAERS)
Peer-Reviewed Journal
ISSN: 2349-6495(P) | 2456-1908(O)
Vol-11, Issue-11; Nov, 2024
Journal Home Page Available: https://ijaers.com/
Article DOI: https://dx.doi.org/10.22161/ijaers.1111.4

Periodic Water Waves: Cnoidal and Solitary Profiles

Syawaluddin Hutahaean

Ocean Engineering Program, Faculty of Civil and Environmental Engineering-Bandung Institute of Technology (ITB), Bandung 40132, Indonesia.
syawalf1@yahoo.co.id

Received: 02 Oct 2024,

Receive in revised form: 01 Nov 2024,

Accepted: 08 Nov 2024,

Available online: 12 Nov 2024

Keywords*— *cnoidal-solitary wave profile

Abstract— *This research formulates the water surface elevation equation for water waves, yielding periodic cnoidal and solitary wave profiles. The equation is derived by integrating the Kinematic Free Surface Boundary Condition with respect to time. The relationships among wave period, wave amplitude, and proportional wavelength facilitate the generation of both cnoidal and solitary wave profiles. In deep water, where wave dynamics are unaffected by the sea bottom, only cnoidal wave profiles are produced. In contrast, solitary profiles emerge through the shoaling-breaking process as waves approach shallower depths.*

I. INTRODUCTION

Wilson (1963) classifies wave profiles into four distinct categories: sinusoidal, Stokes, cnoidal, and solitary profiles. Sinusoidal and Stokes profiles are typically observed in waves with small amplitudes.

The theory of cnoidal waves was first developed by Korteweg and de Vries in 1895, based on observations of wave behavior in canals, thereby confirming their occurrence in natural environments. Cnoidal waves are characterized by a marked asymmetry between the crest and trough, with the wave surface predominantly elevated above the still-water level. The crest presents a steep gradient, while the trough descends below the still-water level more gradually.

Solitary wave profiles, in contrast, are defined by the fact that the entire wave surface remains above the still-water level. This phenomenon was first identified by John Scott Russell in 1844 during laboratory experiments, with the theoretical foundation later provided by Joseph Boussinesq in 1871. Like cnoidal waves, solitary wave profiles have been observed in nature.

Research on cnoidal waves is extensive, with Fenton (1979) contributing significantly to the development of cnoidal wave theory in the context of periodic waves. This research also extends the analysis of periodic cnoidal waves.

Both cnoidal and solitary wave profiles are distinguished by their high crest elevations, with most of the wave profile remaining above the still-water level. In the case of solitary waves, the entire profile stays above this level. Due to their high crest elevations, these wave profiles play a critical role in the design and elevation of coastal structures, as they exert significant forces on such structures. Thus, identifying the appropriate wave profile at a planned construction site is essential.

This research conducts a comprehensive analysis of wave profiles, including assessments in both deep and shallow water, specifically examining wave behavior before and after the breaking point. The water surface elevation equation used for analyzing wave profiles is derived by integrating the Kinematic Free Surface Boundary Condition equation.

II. PRELIMINARY

a. Axis System

In this research, an axis system was used, where x is the horizontal axis and z is the vertical axis.

b. Weighted Taylor Series

The Weighted Taylor series is a truncated form of the Taylor series, limited to the first-order term. In this formulation, coefficients are introduced to the first derivative term, referred to as weighing coefficients.

Weighted Taylor series on function $f(x,t)$,

$$f(x+\delta x, t+\delta t) = f(x,t) + \gamma_{t,2}\delta t \frac{\partial f}{\partial t} + \gamma_x \delta x \frac{\partial f}{\partial x} \quad \ldots\ldots(1)$$

Weighted Taylor series on function $f(x,z,t)$,

$$f(x+\delta x, z+\delta z, t+\delta t) = f(x,t) + \gamma_{t,3}\delta t \frac{\partial f}{\partial t} + \gamma_x \delta x \frac{\partial f}{\partial x} + \gamma_z \delta z \frac{\partial f}{\partial z} \quad \ldots\ldots\ldots\ldots(2)$$

$\gamma_{t,2}$, $\gamma_{t,3}$, γ_x and γ_z are weighting coefficients. This research employed the equation $\gamma_{t,2} = 1.999595$, $\gamma_{t,3} = 3.009774$, $\gamma_x = 0.997583$ and $\gamma_z = 1.022911$. No significant gap is found between γ_x on function $f(x,t)$ and γ_x on function $f(x,z,t)$.

The weighting coefficients and the values of the weighting coefficients were measured based on the formula proposed by Hutahaean (2023).

c. Kinematic free Surface Boundary Condition

Using the weighted Taylor series, the Kinematic Free Surface Boundary Condition is

$$w_\eta = \gamma_{t,2}\frac{\partial \eta}{\partial t} + \gamma_x u_\eta \frac{\partial \eta}{\partial x} \quad \ldots\ldots.(3)$$

Or

$$\gamma_{t,2}\frac{\partial \eta}{\partial t} = w_\eta - \gamma_x u_\eta \frac{\partial \eta}{\partial x} \quad \ldots\ldots.(4)$$

$\eta(x,t)$ represents the equation for the water surface elevation relative to the still water level, w_η is the surface vertical water particle velocity, and u_η is the surface horizontal water particle velocity.

d. Velocity potential

The velocity potential equation, which is the solution to the Laplace equation (Hutahaean, 2023) under the condition $\sin k_x x = \cos k_x x$, is

$$\phi(x,z,t) = 2\, G \cos k_x x \cosh k_z(h+z) \sin \sigma t \quad \ldots\ldots..(5)$$

$\phi(x,z,t)$ is velocity potential.

$\sigma = \frac{2\pi}{T}$ is angular frequency and T is wave period.

$k_x = \frac{k}{\sqrt{\gamma_x}}$ is wave number on horizontal axis

$k_z = \frac{k}{\sqrt{\gamma_z}}$ is wave number of the vertical axis

$k_x \approx k_z \approx k$, k is wave number. Although the difference between k_x and k_z is very small, in this research they are still distinguished to maintain calculation accuracy.

G is the wave constant, which, with dimensions of $m.m/sec$, can be referred to as the wave energy transmission rate.

By integrating the kinematic free surface boundary condition, Hutahaean (2024a) obtained the wave amplitude function as:

$$A = \frac{2Gk}{\gamma_{t,2}\sigma}\cosh\theta\pi\left(\frac{\tanh\theta\pi}{\sqrt{\gamma_z}} - \frac{kA}{2}\right) \quad \ldots\ldots(6)$$

θ is the deep water coefficient where $\tanh\theta\pi \approx 1$. In this research, $\theta = 3.0$ is used to reduce wave height near the coastline. In previous studies, $\theta = 1.94$ was used to obtain $\frac{H_b}{h_b} = 0.78$, where H_b is the breaking wave height and h_b is the breaking water depth. With this θ value, a large wave height is observed near and at the coastline, where for a wave with a period of 8 seconds, a wave height of 2.0 meters can occur at a water depth of 1.0 meter.

III. WATER SURFACE ELEVATION EQUATION

The equation for water surface elevation is derived from the integration of the Kinematic Free Surface Boundary Condition with respect to time, utilizing the complete velocity potential.

$$\phi(x,z,t) = G\ \cosh k_z(h+z)\,(\cos k_x + \sin k_x x)\sin\sigma t \quad \ldots\ldots.(7)$$

This equation is substituted into the Kinematic Free Surface Boundary Condition and integrated with respect to time t.

$$\eta(x,t) = \frac{Gk_z}{\gamma_{t,2}\sigma}\sinh\ k_z(h+\eta)\,(\cos k_x x + \sin k_x x)\cos\sigma t + \frac{\gamma_x G\, k_x}{\gamma_{t,2}\sigma}\cosh\ k_z(h+\eta)\frac{\partial\eta}{\partial x}(-\sin k_x x + \cos k_x x)\cos\sigma t \quad \ldots\ldots.(8)$$

This equation is highly implicit and nonlinear, where the right-hand side contains $\eta(x,t)$ as a hyperbolic function. The calculations are performed in a stepwise manner as follows.

$$\eta(x,t) = A(\cos k_x x + \sin k_x x)\cos\sigma t$$

$$\frac{\partial\eta}{\partial x} = k_x(-\sin k_x x + \cos k_x x)\cos\sigma t$$

$$\eta(x,t) = \frac{Gk_z}{\gamma_{t,2}\sigma}\sinh\ k_z(h+\eta)\,(\cos k_x x + \sin k_x x)\cos\sigma t + \frac{\gamma_x G\, k_x}{\gamma_{t,2}\sigma}\cosh\ k_z(h+\eta)\frac{\partial\eta}{\partial x}(-\sin k_x x + \cos k_x x)\cos\sigma t \quad \ldots..(9)$$

The wave profile is constructed at a specific value of $\cos\sigma t$ using $\cos\sigma t = 1$, over one wavelength, which is defined for $\pi \le k_x x \le 3.0\pi$.

IV. WAVE NUMBER OF DEEP WATER

In this section, the wave number equation for deep water is formulated using the water surface elevation equation, to obtain a wave number that is consistent with the water surface elevation equation.

The maximum water surface elevation is achieved when $\frac{\partial \eta}{\partial x} = 0$. Under this condition, the second term in (9) is zero:

$$\eta_{max} = \frac{Gk_z}{\gamma_{t,2}\sigma} \sinh\ k_z(h+\eta)\,(\cos k_x x + \sin k_x x)\cos \sigma t$$

The maximum water surface elevation relative to its stationary point or still water level is equal to the wave amplitude:

$$A = \frac{Gk_z}{\gamma_{t,2}\sigma} \sinh\ k_z(h+A)\,(\cos k_x x + \sin k_x x)\cos \sigma t$$

The maximum elevation occurs when $\cos \sigma t = 1$.

$$A = \frac{Gk_z}{\gamma_{t,2}\sigma} \sinh\ k_z(h+A)\,(\cos k_x x + \sin k_x x)$$

In (9), the second term is zero if $\cos kx = \sin kx$. Therefore, this condition provides an effect equivalent to $\frac{\partial \eta}{\partial x} = 0$. Under the condition of $\cos kx = \sin kx$,

$$A = \frac{2Gk_z}{\gamma_{t,2}\sigma} \sinh\ k_z(h+A)\cos k_x x$$

If $\cos kx = \sin kx$, the value of $\cos kx = \frac{1}{\sqrt{2}}$

$$A = \frac{\sqrt{2}Gk_z}{\gamma_{t,2}\sigma} \sinh\ k_z(h+A)$$

In the deep water, $k_z(h+A) = k_z h\left(1+\frac{A}{h}\right) \approx k_z h\left(1+\frac{A}{2h}\right) \approx \theta\pi$, where $\tanh \theta\pi \approx 1.0$,

$$A = \frac{\sqrt{2}Gk_z}{\gamma_{t,2}\sigma} \sinh\ \theta\pi$$

Since $k_z = \frac{k}{\sqrt{\gamma_z}}$,

$$A = \frac{\sqrt{2}Gk}{\gamma_{t,2}\sigma\sqrt{\gamma_z}} \sinh\ \theta\pi \qquad \text{.....(10)}$$

The wave amplitude in this equation must be equal to the wave amplitude in (6).

$$\frac{\sqrt{2}Gk}{\gamma_{t,2}\sigma\sqrt{\gamma_z}} \sinh\ \theta\pi = \frac{2Gk}{\gamma_{t,2}\sigma} \cosh \theta\pi \left(\frac{\tanh \theta\pi}{\sqrt{\gamma_z}} - \frac{kA}{2}\right)$$

$$\frac{\tanh\ \theta\pi}{\sqrt{\gamma_z}} = \sqrt{2}\left(\frac{\tanh \theta\pi}{\sqrt{\gamma_z}} - \frac{kA}{2}\right)$$

$$k_0 = \left(2-\sqrt{2}\right)\frac{\tanh \theta\pi}{A_0\sqrt{\gamma_z}} \qquad \text{.....(11)}$$

The equation provided represents the wave number equation applicable in deep water, with the index 0 indicating that the wave amplitude pertains to deep water conditions.

While Equation (11) is derived from Equation (9), it yields a water surface elevation characterized by $\eta_{max} - \eta_{min} < H$. To satisfy the condition $\eta_{max} - \eta_{min} = H$, thus equation (11) must be adjusted by introducing a coefficient given by:

$$k_0 = 1.142x\left(2-\sqrt{2}\right)\frac{\tanh \theta\pi}{A_0\sqrt{\gamma_z}} \qquad \text{.....(12)}$$

The coefficient 1.1421 is notably close to 1.0, indicating that Equation (11) aligns well with (9).

V. WAVE PROFILE IN DEEP WATER AT MAXIMUM WAVE HEIGHT

This section focuses on the analysis of wave profiles at maximum wave height during a specific wave period. The maximum wave height in deep water is defined by the Wiegel equation (1949-1964):

$$H_0 = \frac{gT^2}{15.6^2} \qquad \text{.....(13)}$$

Or Hutahaean (2024a),

$$H_0 = \left(\frac{\tanh \theta\pi}{\sqrt{\gamma_z}}\right)^2 \frac{g}{\sigma^2\,\gamma_{t,2}\,\gamma_{t,3}} \qquad \text{.....(14)}$$

Both formulations yield the same maximum wave height.

The calculated values of H_0 and L_0 across various wave periods, along with their wave profile characteristics including critical wave steepness and wave profile criteria based on Wilson (1963) are presented in Table 1.

Table 1: Wave Profile Characteristics in Deep Water

T (sec)	H_0 (m)	L_0 (m)	$\frac{H_0}{L_0}$	$\frac{\eta_{max}}{H_0}$
2	0.161	0.767	0.211	0.864
3	0.363	1.725	0.211	0.864
4	0.646	3.067	0.211	0.864
5	1.009	4.793	0.211	0.864
6	1.453	6.902	0.211	0.864
7	1.978	9.394	0.211	0.864
8	2.583	12.27	0.211	0.864
9	3.269	15.529	0.211	0.864
10	4.036	19.172	0.211	0.864
11	4.884	23.198	0.211	0.864
12	5.812	27.607	0.211	0.864
13	6.822	32.4	0.211	0.864
14	7.911	37.576	0.211	0.864
15	9.082	43.136	0.211	0.864

16	10.333	49.079	0.211	0.864
17	11.665	55.406	0.211	0.864
18	13.078	62.116	0.211	0.864

In Table (1), $\frac{H_0}{L_0}$ represents the wave steepness. Given that H_0 is defined as the maximum wave height, the resulting $\frac{H_0}{L_0}$ reflects the critical wave steepness. Research by Toffoli et al. (2010) established a critical wave steepness threshold of 0.170, recommending a value of 0.200. The critical wave steepness derived from this research is $\frac{H_0}{L_0} = 0.211$, indicating that the wavelength obtained aligns closely with the findings of Toffoli et al.

$\frac{\eta_{max}}{H_0}$ represents the wave profile criteria as defined by Wilson (1963). This criterion is detailed in Table 2 and illustrated in Fig 1. The value $\frac{\eta_{max}}{H_0}$ is 0.864, which, according to the Wilson criterion in Table 2, classifies the wave profile as a cnoidal profile.

Table 2: Water wave profile criteria (Wilson (1963)))

Wave type	$\frac{\eta_{max}}{H}$
Airy/sinusoidal waves	< 0.505
Stoke's waves	$0.505 - 0.635$
Cnoidal waves	$0.635 - 1$
Solitary waves	$= 1$

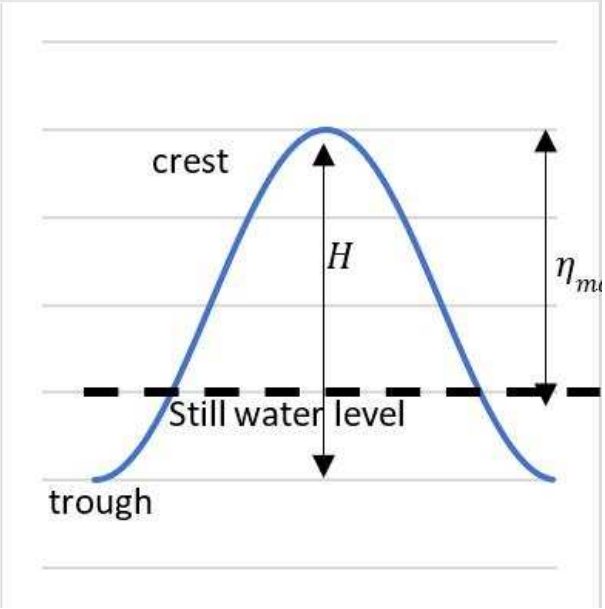

Fig.1: Wave profile for Wilson (1963) criteria.

In Figure 2, the wave profile is illustrated for a wave period of $T = 8.0$ sec with a wave height of $H_0 = 2.583\ m$. The resulting wave profile is identified as a cnoidal profile.

Waves with wave period $T = 2.0\ sec.$ and wave height $H_0 = 0.161\ m.$ are also cnoidal (Fig(3)).

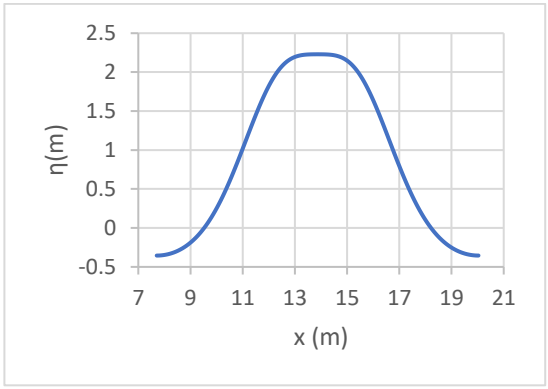

Fig.2: Wave profile, wave period $T = 8.0$, $H_0 = 2.583\ m$, $\frac{\eta_{max}}{H_0} = 0.864\ m.$

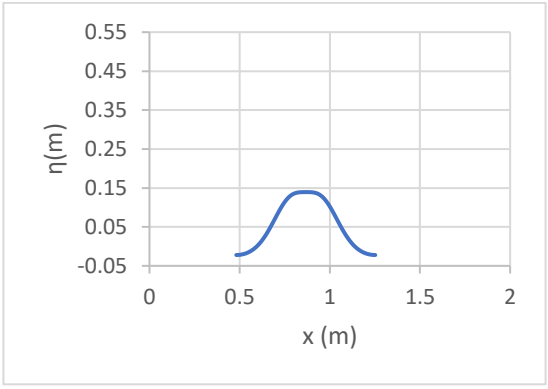

Fig.3: Wave profile, wave period $T = 2.0$, $H_0 = 0.161\ m$, $\frac{\eta_{max}}{H_0} = 0.864.$

The findings of this section indicate that the wave profile generated by the system of equations specifically, the maximum wave height equation, the wave number equation, and the water surface elevation equation in deep water yields a cnoidal wave profile.

VI. SHOALING-BREAKING MODEL

The shoaling-breaking model employed in this research is based on the framework developed by Hutahaean (2023). As waves propagate from point x with water depth h_x towards $x + \delta x$, at small δx, with water depth $h_{x+\delta x}$ show changes in the parameters as follows.

$$\frac{\partial k}{\partial x} = -\frac{4k}{(4h+3A)}\frac{dh}{dx} \qquad \text{.....(15)}$$

$$k_{x+\delta x} = k_x + \delta x \frac{\partial k}{\partial x}$$

$$\frac{\partial A}{\partial x} = \frac{G}{\sigma \gamma_{t,2}} \frac{\partial k}{\partial x} \left(\frac{1}{\sqrt{\gamma_z}} - \frac{kA}{2} \right) \cosh(\theta \pi) \quad \text{.....(16)}$$

$$A_{x+\delta x} = A_x + \delta x \frac{\partial A}{\partial x}$$

$$G_{x+\delta x} = e^{\ln G_x - \frac{1}{2}(\ln k_{x+\delta x} - \ln k_x)} \quad \text{.....(17)}$$

a. Results of Shoaling-Breaking Analysis with Wave Profile

In this section, a shoaling-breaking analysis is conducted on waves characterized by a wave period of $T = 8.0\ sec.$, wave height $H_0 = 2.583m.$, deep water depth $h_0 = 17.759$ m. The findings from this analysis are illustrated in Figure 4, where the breaking wave height is $H_b = 3.298$ m at a breaker depth $h_b = 6.921\ m$, $\frac{H_b}{h_b} = 0.477$. In this research, the traditional criterion of $\frac{H_b}{h_b} = 0.78$, has been set aside, as adherence to this standard resulted in excessively large wave heights near the coastline. If the criterion of $\frac{H_b}{h_b} = 0.78$ d were to be utilized, it would necessitate a deep water coefficient $\theta = 1.94$. However, to ensure that the wave height near the coastline remains manageable, a deep water coefficient of $\theta = 3.0$ was employed in this analysis.

It is important to note that the breaking wave height observed in this research differs from findings in previous research, such as Hutahaean (2024b). This discrepancy can be attributed to the longer wavelength in deep water present in this research, which consequently leads to an increase in wave energy.

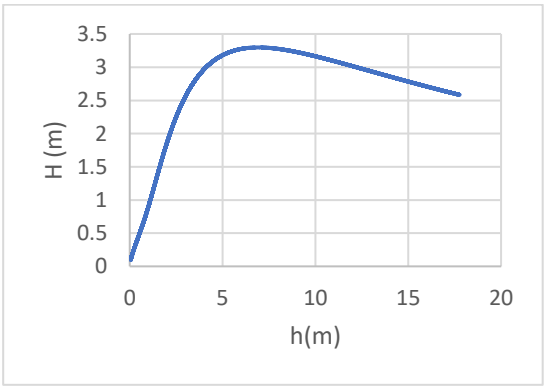

Fig.4: The results of shoaling-breaking analysis

Subsequently, a wave profile analysis was carried out in shallow water at a water depth. h, 12.0 m, 6.921 m (breaking point), 3.0 m ,1.0 m and 0.50 m .

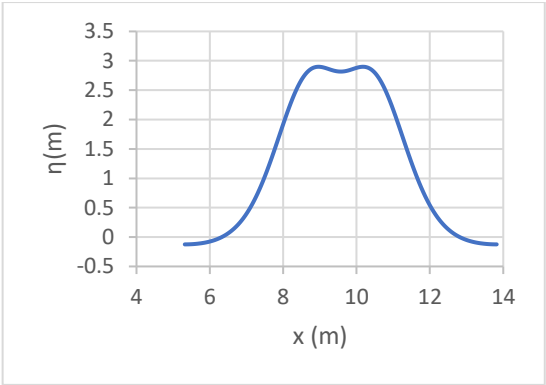

Fig.5: Wave profile at $h = 12.0\ m$, $\frac{\eta_{max}}{H} = 0.959$, $H = 3.016\ m$

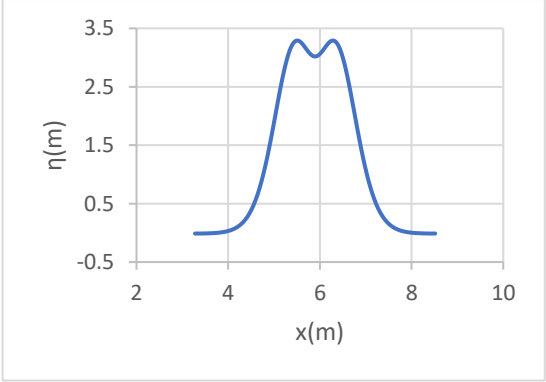

Fig.6: Wave profile at $h = 6.921\ m$ (breaker depth), $\frac{\eta_{max}}{H} = 1.0$, $H = 3.298\ m$

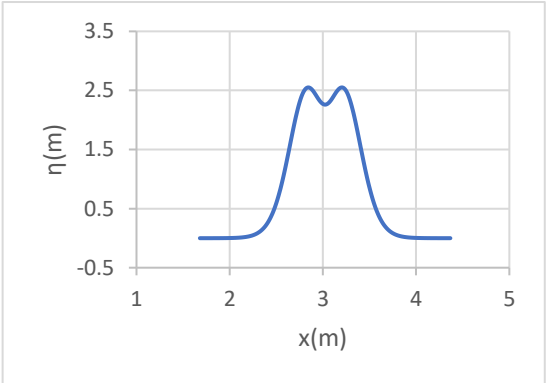

Fig.7: Wave profile at $h = 3.0\ m$, $\frac{\eta_{max}}{H} = 1.0$, $H = 2.560\ m$

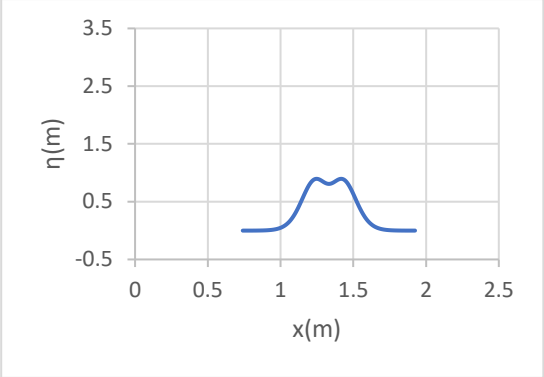

Fig.8: Wave profile at $h = 1.0\ m$, $\frac{\eta_{max}}{H} = 1.00$, $H = 0.895\ m$

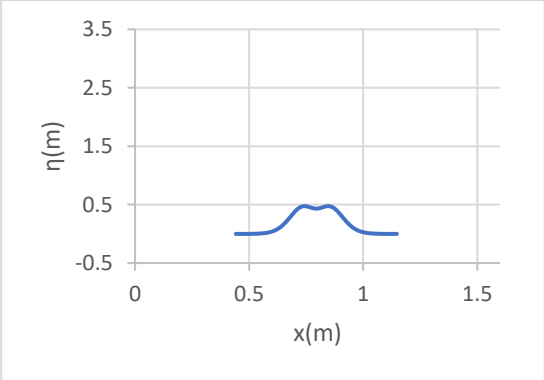

Fig.9: Wave profile at $h = 0.5\ m$, $\frac{\eta_{max}}{H} = 1.00$, $H = 0.475\ m$

Table 3: Wave Profile Summary

h (m)	H (m)	$\frac{\eta_{max}}{H}$	Profile
17.87	2.583	0.864	Cnoidal
12.0	3.016	0.959	Cnoidal
6.921	3.298	1.0	Solitary
3.0	2.560	1.0	Solitary
1.0	0.895	1.0	Solitary
0.5	0.475	1.0	Solitary

In deep water, as illustrated in Figure 2, the wave profile is characterized as cnoidal, with a ratio of $\frac{\eta_{max}}{H_0} = 0.864$. As the wave progresses towards the coastline, this cnoidal profile undergoes significant evolution, primarily through an increase in the value of $\frac{\eta_{max}}{H}$ as presented in Table 2. This transformation ultimately leads to the formation of a solitary wave profile. At the breaking point, where $\frac{\eta_{max}}{H} = 0.996$ the wave can be classified distinctly as a solitary profile.

In a time series model, Hutahaean (2024b) corroborated these findings, demonstrating that the cnoidal profile observed in deep water evolves into a solitary profile as it transitions into shallower waters.

VII. CONCLUSION

The first conclusion drawn from this research is that the system of equations, which includes the dispersion equation, wave height equation, and surface elevation equation, generates both cnoidal and solitary wave profiles. These profiles are characteristic of short waves commonly observed in nature.

As cnoidal waves propagate from deep to shallow water, they undergo a profile evolution, transitioning from a cnoidal to a solitary wave form. This evolution is marked by an increase in the parameters governing the wave profile.

In shallow water, wave profiles are predominantly cnoidal and/or solitary. For structural design in shallow water, it is recommended to use the solitary wave profile for both elevation planning and wave force calculations. In contrast, for deep-water conditions, the cnoidal profile can be applied when the Wilson criterion exceeds 0.8. However, for enhanced safety, it is advisable to use the solitary wave profile, regardless of the water depth, to account for potential extreme wave forces.

REFERENCES

[1] Wilson, B.W. (1963). Condition of Existence for Types of Tsunami Waves, paper presented at XIIIth Assembly IUGG, Berkeley, California, August 1963 (unpublish).

[2] Korteweg, D.J. and De Vries, J. (1895). On the Change of Form of Longwaves Advancing, in a Rectangular Canal, and on a New Type of Long stationary Waves. Phil.Mag., 5th Series, Vol. 39, pp. 422-443.

[3] Russel, J.S., 1844. Report on Waves. 14th Meeting Brit. Assoc. Adv. Sci., pp. 311-390.

[4] Boussinesq, J. , 1871. Theori de L'intumesence Liquide , Apelee Onde Solitaire ou de Translation se Propageant Dans un Canal Rectangulaire. Comptes Rendus Acad . Sci., Paris, Vol.72, pp.755-759.

[5] Fenton, J.D. (1979). A High Order Cnoidal Wave Theory. J. Fluid Mechanic. 94, 129-161.

[6] Hutahaean, S. (2023). Method for Determining Weighting Coefficients in Weighted Taylor Series Applied to Water Wave Modeling. International Journal of Advance Engineering Research and Science (IJAERS). Vol. 10, Issue 12; Dec, 2023, pp 105-114. Article DOI: https://dx.doi.org/10.22161/ijaers.1012.11.

[7] Hutahaean, S. (2024a). The Relationship Between Wave Period, Deep Water Wave and Breaking Wave Heights,

Formulated Using Wave Amplitude Function . Journal of Advance Engineering Research and Science (IJAERS). Vol. 11, Issue 9; Sep, 2024, pp 8-15. Article DOI: https://dx.doi.org/10.22161/ijaers.119.1.

[8] Wiegel,R.L. (1949). An Analysisis of Data from Wave Recorders on the Pacific Coast of tht United States, Trans.Am. Geophys. Union, Vol.30, pp.700-704.

[9] Wiegel,R.L. (1964). Oceanographical Engineering, Prentice-Hall, Englewoods Cliffs, N.J.

[10] Toffoli, A., Babanin, A., Onaroto, M. and Wased, T. (2010). Maximum steepness of oceanic waves : Field and laboratory experiments.Geophysical Research Letters. First published 09 March 2010.https://doi.org/10.1029/2009GL.0441771

[11] Hutahaean, S. (2024b). Applying Weighted Taylor Series on Time Series Water Wave Modeling. International Journal of Advance Engineering Research and Science (IJAERS). Vol. 11, Issue 2; Feb, 2024, pp 38-47. Article DOI: https://dx.doi..org/10.22161/ijaers.112.6.

International Journal of Advanced Engineering Research and Science (IJAERS)
Peer-Reviewed Journal
ISSN: 2349-6495(P) | 2456-1908(O)
Vol-11, Issue-11; Nov, 2024
Journal Home Page Available: https://ijaers.com/
Article DOI: https://dx.doi.org/10.22161/ijaers.1111.5

The Science Behind the Wind: Materials Driving Wind Energy's Future - Overview

Charitidis J. Panagiotis

Department of Environmental Engineering, Democritus University of Thrace, Xanthi, Greece
pchariti@env.duth.gr

Received: 05 Oct 2024,
Receive in revised form: 03 Nov 2024,
Accepted: 10 Nov 2024,
Available online: 15 Nov 2024

***Keywords*— composite materials, failure mechanisms, renewable energy, lifespan, risk assessment.**

***Abstract*—** *The relentless pursuit of renewable energy has driven significant advancements in wind turbine technology, with material innovation playing a pivotal role. This paper explores the intricate relationship between materials and wind turbine performance, exploring the properties, advantages, limitations, and risks associated with traditional and emerging materials, including fiberglass, carbon fiber, bio-based composites, nanomaterials, and hybrid composites. The paper examines the complex interplay between material selection and blade design. Optimized designs can mitigate failure mechanisms like delamination, cracking, and erosion. By analyzing case studies and leveraging advanced simulation techniques, the paper assesses the impact of various materials on blade lifespan, performance, and environmental impact. As we look to the future, sustainability and recyclability emerge as critical considerations. The paper discusses the potential of bio-based materials and innovative manufacturing techniques to reduce the environmental footprint of wind energy. By understanding the materials science, we can unlock the full potential of wind power and accelerate the transition to a cleaner, more sustainable energy future.*

I. INTRODUCTION

The global shift toward renewable energy sources has underscored the importance of wind power as a sustainable solution for reducing greenhouse gas emissions and combating climate change [**1, 2**]. As wind energy becomes an increasingly significant contributor to the energy mix, the performance and longevity of wind turbine components, particularly the blades, have gained critical attention. Wind turbine blades are subjected to a wide range of mechanical and environmental stresses, leading to issues such as cyclic deformation, erosion, and material degradation over time [**3-10**]. These challenges not only impact the operational efficiency of wind turbines but also result in significant maintenance costs and downtimes [**11, 12**]. Material selection plays a pivotal role in determining the durability and overall performance of wind turbine blades, directly influencing factors such as weight, stiffness, resistance to fatigue, and susceptibility to environmental degradation [**13-21**]. Traditional materials like fiberglass and wood have been widely used, but their limitations often necessitate the exploration of advanced materials, including carbon fiber composites and bio-based alternatives [**22, 23**]. Each material presents unique advantages and challenges, making the decision process complex and multifaceted. Combining one or more fiber materials in a single composite creates a hybrid composite material with additional advanced properties compared to

single-material fiber composites. The bonding parameters of these different fibers and resins significantly influence the properties of the hybrid composite [**24, 25**]. Incorporating nanomaterials into composites can further enhance their properties, resulting in lightweight, high-strength, and smart materials that are ideal for wind turbine blades [**26-31**].

This paper aims to provide a comprehensive overview of material selection strategies aimed at extending the lifespan of wind turbine blades. By analyzing the mechanical properties, failure mechanisms, and innovative materials available in the current landscape, this study will highlight best practices in material selection that can enhance blade durability and performance. Additionally, it will discuss the implications of these choices for maintenance practices and the economic viability of wind energy projects. Ultimately, this research seeks to contribute to the ongoing efforts to optimize wind turbine design and operation, ensuring that wind power remains a reliable and sustainable energy source for the future.

II. MATERIALS

The selection of materials for wind turbine blades is critical to ensuring optimal performance, durability, and cost-effectiveness throughout their lifecycle. This section outlines the properties of commonly used materials, such as fiberglass, carbon fiber, wood, and advanced composites. Due to its favorable balance of mechanical properties and cost, fiberglass is one of the most widely used materials for wind turbine blades. With tensile strengths of approximately 350–500 MPa and a modulus of elasticity between 30 and 40 GPa, fiberglass provides adequate strength and stiffness for many applications. Its shear strength typically ranges from 40 to 60 MPa, and it exhibits good fatigue resistance, making it suitable for dynamic loading conditions encountered in wind applications. However, fiberglass can experience performance degradation under high-stress cycles over extended periods. Its relatively low weight helps reduce the overall mass of turbine structures, enhancing efficiency. E-glass fibers, commonly used as reinforcement in fiberglass composites, provide high electrical resistance and adequate stiffness, while S-glass fibers offer superior tensile strength and durability, suitable for high-stress applications, albeit at a higher cost [**32**]. In composites with high fiber volume content (above 65%), dry areas without resin can form, reducing the composite's fatigue strength. Typically, glass/epoxy composites used in wind blades contain up to 75% glass by weight [**33**].

Carbon fiber offers a high-performance alternative to fiberglass, with significantly higher tensile strength (600–900 MPa) and modulus of elasticity (70–150 GPa), allowing for thinner, more efficient blade designs [**34**]. Its shear strength, generally around 70–100 MPa, and excellent fatigue resistance make it ideal for withstanding fluctuating wind conditions. Although, carbon fiber's high production costs limit its use. It is primarily used in specialized components or high-performance turbines [**35, 36**]. While carbon fiber has advantages in strength-to-weight ratio, it also has limitations in compressive strength and damage tolerance, making fiber alignment critical for optimal performance. Companies like Vestas and Siemens Gamesa incorporate carbon fiber in the spar caps of large blades, leveraging its strength despite the cost constraints [**35**].

Wood, once a traditional engineering material, has limited applications in modern turbine blades. Its tensile strength depends on species, typically ranging from 50 to 100 MPa, with a modulus of elasticity between 10 and 20 GPa. Though wood can be a cost-effective choice, particularly when sustainably sourced, its properties are generally inferior to synthetic materials. While relatively lightweight, wood is sometimes heavier than fiberglass or carbon fiber, which can affect efficiency in turbine applications.

Aramid and basalt fibers provide alternative reinforcements to glass fibers. Aramid fibers, such as Kevlar, are known for high mechanical strength, toughness, and damage tolerance. However, they exhibit low compressive strength, poor adhesion to polymer resins, and are susceptible to moisture absorption and UV degradation [**37**]. Basalt fibers, approximately 30% stronger and 15–20% stiffer than E-glass fibers while being 8–10% lighter, offer a cost-effective, lightweight solution for small turbine applications [**35, 38, 39**].

Advanced composites, often combining multiple materials for enhanced performance, emerge for wind turbine blades. These composites typically have tensile strengths between 400 and 800 MPa and moduli of elasticity from 40 to 120 GPa. The enhanced fatigue resistance and strength of advanced composites make them a promising, though costly, choice for high-performance applications.

Hybrid composites that combine materials like E-glass with carbon or aramid fibers offer a balanced option. Replacing all glass fibers with carbon fiber can reduce weight by up to 80%, though this approach increases costs by about 150%. Partial replacement can achieve a 50% weight reduction with a 90% cost increase, making it practical for smaller turbines [**40**]. The 88.4-meter blade by LM Wind Power, the longest blade globally, utilizes

carbon/glass hybrid composites, demonstrating this approach's effectiveness in large-scale applications [**41**].

Growing awareness of synthetic materials' environmental impact has spurred research into biodegradable alternatives. Natural fiber composites, including sisal, flax, hemp, and jute, offer renewable, low-cost options with partial biodegradability. These materials show potential, with bamboo-poplar epoxy laminates emerging as particularly promising due to bamboo's rapid growth and availability [**42, 43**]. However, moisture absorption in natural fibers can lead to composite weakening, especially in offshore environments where exposure to humidity is high. Quality control also remains challenging due to variability in natural fibers' properties, which can impact performance predictability. Despite limitations in tensile strength and durability compared to synthetic fibers, natural fibers are promising for applications where eco-friendliness is prioritized [**44**].

In selecting matrix materials, thermosetting polymers, such as epoxy, polyester, and vinyl ester, are common due to their strength, rigidity, and thermal stability, which are critical for withstanding the high loads on turbine blades. However, these matrices are non-recyclable, posing environmental challenges at the end of life [**45**]. Thermoplastic matrices, like polypropylene and polyamide, offer recyclability and better impact resistance, which enhances durability. They can be remelted and reformed, facilitating high-throughput production and repairs, though they generally exhibit lower fatigue resistance compared to thermosets [**46**].

Optimizing natural fiber composites for wind turbines often involves thermosetting matrices to provide structural durability. Thermoplastic matrices, while recyclable and offering some flexibility in manufacturing, may perform better in smaller turbines, where high loads are less demanding. Although thermosetting matrices are more durable, thermoplastics contribute significantly to sustainability efforts in wind energy applications, particularly when paired with natural fibers. The mechanical properties of reinforcement and matrix materials as well as the advantages and applications of material properties for wind turbine blades are summarized in Table 1 and 2.

Table. 1: Material Properties of Reinforcements and Matrices Used in Wind Turbine Blades.

Composites	**Tensile Strength (MPa)**	**Young's Modulus (GPa)**	**Density (g/cm³)**
Fiberglass	700-1500	35-80	2.5
Carbon Fiber	3000-6000	230-600	1.6
Aramid (Kevlar)	2500-3000	70-120	1.44
Basalt Fiber	2000-4000	80-110	2.7
Advanced Composites (Carbon Nanotubes)	6000-20000	500-1000	1.3-1.8
Hybrid	Varies	Varies	Varies
Sisal/Epoxy	200–500	5–10	1.2-1.5
Flax/Epoxy	100–300	6–13	1.4
Nanomaterials (e.g., Graphene)	Up to 130,000	1000	1.3
Thermoset Matrices (e.g., Epoxy)	40–100	3-5	1.1-1.2
Thermoplastic Matrices (e.g., Polyethylene, PEEK)	50–150	2-4	1.0-1.4

Table. 2: Advantages and Applications of Material Properties of Reinforcements and Matrices Used in Wind Turbine Blades.

Composites	Advantages	Applications
Fiberglass	Cost-effective, corrosion-resistant, moderate strength	Widely used in wind turbine blades
Carbon Fiber	High strength-to-weight ratio, excellent stiffness	High-stress areas, premium blade designs
Aramid (Kevlar)	Lightweight, high toughness, good impact resistance	Parts needing impact resistance
Basalt Fiber	Sustainable, cost-effective, good thermal and chemical stability	Sustainable wind turbine projects
Advanced Composites (Carbon Nanotubes)	Extremely high strength and stiffness (e.g., carbon nanotubes)	Primarily in research; future reinforcement applications
Hybrid	Tailored performance, balance of cost and strength	Optimized performance areas in blade regions
Sisal/Epoxy	Renewable, eco-friendly	Non-load-bearing parts, eco-friendly projects
Flax/Epoxy	Renewable, eco-friendly, moderate mechanical properties	Non-load-bearing parts, eco-friendly projects
Nanomaterials (e.g., Graphene)	Increases matrix properties, high thermal/electrical conductivity	Reinforcement to improve fatigue life and stiffness
Thermoset Matrices (e.g., Epoxy)	High strength, thermal stability, excellent adhesion, resistance to deformation under heat	Matrix for most fiberglass and carbon fiber composites
Thermoplastic Matrices (e.g., Polyethylene, PEEK)	Tough, recyclable, lower processing time, adaptable for lightweight applications	Matrix for recyclable composites, flexible wind turbine parts

III. FAILURE MECHANISMS

Wind turbine blades are subjected to various mechanical and environmental stresses throughout their operational lifespan, making them vulnerable to a range of failure mechanisms. Understanding these failure modes is essential for improving blade design, selecting appropriate materials, and enhancing the overall reliability of wind energy systems. This section examines common failure modes such as delamination, cracking, and erosion, highlighting how material choices influence these mechanisms and providing insights into the response of different materials to environmental conditions (**figure 1**).

3.1 Delamination and Cracking

Delamination in wind turbine blades, particularly in fiber-reinforced composites, represents a critical failure mode. Key factors influencing delamination include energy release rates (ERR), which quantify the force driving crack growth. Mode-I (G_I) characterizes crack opening under tensile stress, while Mode-II (G_{II}) describes shear-driven delamination. The critical fracture toughness values (G_{IC} and G_{IIC}) mark the thresholds at which delamination begins. For unidirectional carbon fiber-reinforced epoxy composites, G_{IC} and G_{IIC} were found to be 273 J/m² and 1177 J/m², respectively [**47, 48**].

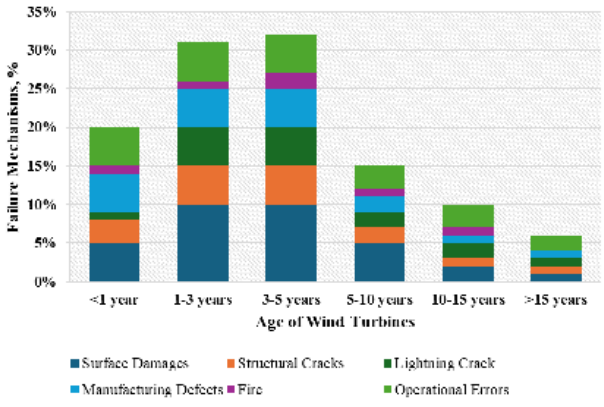

Fig. 1: Frequency of wind turbine blade failure mechanisms depending on the age of wind turbines [7].

In composite laminates, mixed-mode delamination, involving both tensile and shear forces, is common. The

mode ratio (G_{II}/G) expresses the contribution of these forces, with a range of 65% to 75%, indicating a dominant role of shear forces [**49**]. Delamination testing, particularly the End Notched Flexure with Roller (ENFR) method, assesses both modes simultaneously, allowing for mixed-mode delamination analysis by adjusting roller placement and initial crack length. The fracture behavior is analyzed through a fracture envelope relating G_I and G_{II}, which predicts crack propagation, described by the linear failure criterion:

$$\frac{G_I}{G_{II}} + \frac{G_{II}}{G_{III}} = 1$$

The total ERR exceeds a critical threshold (Geq), initiating delamination. Aerodynamic forces also impact delamination, as cyclic loads from varying wind speeds and turbulence lead to repeated stresses, heightening fatigue and delamination risk. High dynamic pressures near the leading edge and loads at the spar caps, which bear the blade's primary load, further contribute to delamination due to constant bending [**50, 51**]. Stress concentrations at the blade root (**figure 2**) from torque and aerodynamic forces, especially in tapered regions and ply-drop transitions, exacerbate delamination under fatigue loading [**52**].

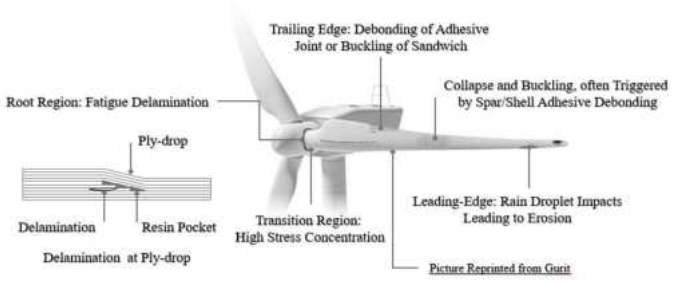

Fig. 2: The blade root, where high-stress concentrations exist due to torque and aerodynamic loads, also experiences delamination under these conditions.

Fig. 3: Preventive measures against delamination using (a) staggered ply drops and (b) chamfered edges.

Areas prone to delamination, like ply drop-off regions, experience interlaminar stresses due to ply termination. Staggering ply drops, chamfering edges, and reinforcement techniques such as Z-spiking reduce delamination risks, especially in carbon fiber laminates, which are more prone to delamination due to higher modulus and lower compression strength than glass fiber laminates [**53, 54, 55**] (**figure 3**). Carbon fiber laminates with ply-drop terminations, resin pockets, and stress concentrators benefit from these preventive measures, which improve blade integrity by optimizing the laminate structure.

In Glass Fiber Reinforced Polymer (GFRP), manufacturing defects like out-of-plane wrinkles critically reduce fatigue life, with specimens showing a 66% reduction compared to pristine laminates [**56**]. Due to higher stiffness, crack initiation driven by fiber misalignment and matrix or fiber interface propagation, advances more quickly in Carbon Fiber Reinforced Polymer (CFRP) (**figure 4**). This effect leads to earlier delamination and faster crack growth, significantly impacting blade fatigue life. In tension-compression fatigue tests, CFRP laminates with wrinkles showed a tenfold reduction in fatigue life compared to wrinkle-free specimens [**56–59**].

The root region, where blade load transfers to the hub, is particularly susceptible to delamination and adhesive debonding. Stress concentrations due to abrupt laminate transitions are amplified in areas near T-bolt connections, posing risks of blade detachment if debonding occurs [**60**].

Effective distribution around these connections helps alleviate stress concentrations, extending blade life (**figure 5**).

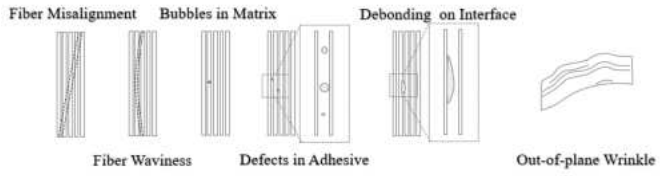

Fig. 4. Types of defects that cause cracking, and delamination.

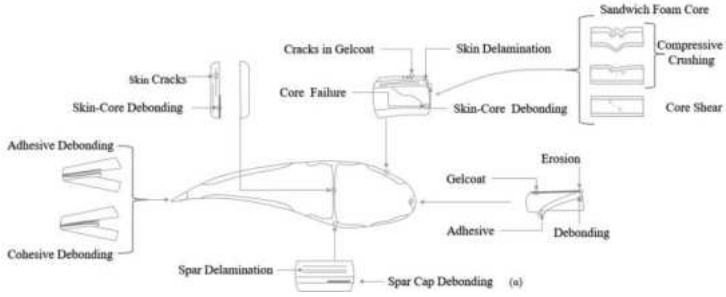

Fig. 5: Adhesive debonding and delamination zones on a wind turbine blade.

Unsteady aerodynamic effects from turbulence and gusts worsen delamination at mid-span and trailing edges, where shear flow shifts quickly. Larger, more flexible modern blades are especially prone to these effects, as

increased flexing generates interlaminar shear forces. Addressing these factors through design and material selection is essential to enhance the durability of wind turbine blades

3.2 Erosion

A mix of meteorological, material, and aerodynamic factors significantly affect the erosion of wind turbine blades. Rainfall intensity and drop size distribution (DSD) are critical. Larger raindrops, characteristic of convective rain, exert a greater force on blades, leading to surface degradation [**61-67**]. Erosion severity escalates with higher wind speeds during rain, as raindrop impact velocity raises contact pressure on the blade surface, causing wave propagation through protective layers that can result in cracks and delamination [**68**]. For instance, increasing impact speeds from 120 to 160 m/s can amplify peak stress thrice or more [**69**]. Over time, surface erosion leads to cracks in laminate layers and water ingress into bond lines, reducing structural integrity and enabling more severe damage if unaddressed [**70, 71**]. This erosion process also diminishes the blade's fatigue resistance, compounding the risk of structural failures (**figure 6**).

Material resistance to erosion depends on durability and the capacity to withstand prolonged raindrop impact without delamination. Thermoplastic polyurethane (TPU), with its high mechanical resilience, shows promise for leading-edge protection, providing superior durability compared to other materials [**72**]. Environmental factors like hail and airborne particles such as sand or dust worsen erosion, especially in coastal and offshore environments where solid particles combined with rain hasten surface wear. The leading edge, being most exposed to environmental impacts, is particularly vulnerable to these effects. Besides erosion, lightning strikes are a significant threat, especially near the blade tip, where they can cause the debonding of skins from shear webs, leading to structural weaknesses that, without timely repairs, risk catastrophic failure. Additionally, rain erosion is a primary cause of degradation, potentially lowering energy production by 5% or more if left unrepaired [**7**].

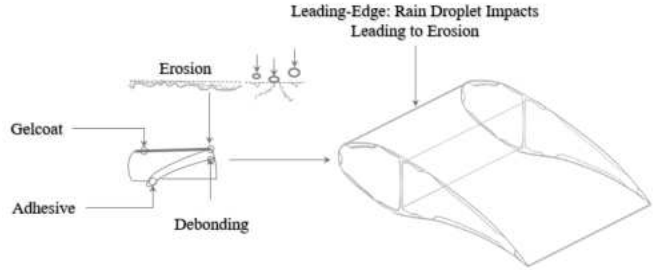

Fig: 6: Leading edge: rain droplet impacts leading to erosion.

Surface roughness also affects erosion rates. Rougher surfaces experience higher concentrations of stress , accelerating wear relative to smoother ones. Multilayered protective coatings, particularly those with flexible materials like TPU, help absorb impact stresses and resist delamination when adhered effectively. Computational models simulate droplet impacts and track stress progression within laminate and coating layers, allowing for optimized protective solutions [**73, 74**].

Aerodynamic performance further impacts erosion, especially on the leading edge, which faces high aerodynamic forces and pressure shifts. High-speed airflow over the blade generates lift, but combined with raindrops and particle impacts, it accelerates surface wear [**8**]. Leading-edge roughness from erosion not only lowers aerodynamic efficiency by increasing drag but also amplifies erosion by introducing turbulence and stress on the surface, potentially reducing annual energy production (AEP) by 2-25% and increasing maintenance demands [**75**]. Solutions like in-mold TPU coatings and enhanced bonding aim to counter erosion and extend blade service life, although these coatings may add aerodynamic drag.

Rain erosion testing, including rain erosion testers and impact tests, evaluates material resistance to erosive damage by simulating real-world impacts. These tests provide essential data on long-term material durability for the leading edge. Preventive strategies, such as advanced coatings, leading-edge shields, and protective tapes, are employed to minimize erosion damage and enhance blade durability [**8**]. Implementing these measures supports blade longevity and operational efficiency.

3.3 Environmental Effects

Wind turbine blades are continually exposed to varying environmental conditions, including temperature fluctuations and moisture. Different materials respond uniquely to these changes, influencing their long-term performance and reliability. Thermal fluctuations create stresses within the blade material. These stresses potentially lead to delamination or cracking. For example, carbon fiber composites typically have a lower coefficient of thermal expansion compared to fiberglass, making them less susceptible to dimensional changes with temperature fluctuations. Even so, if not properly engineered, the rigidity of carbon fiber can lead to issues when bonded with materials that expand differently, resulting in stress concentrations. Fiberglass, while more flexible, may absorb moisture, which can also lead to thermal issues when combined with temperature changes. In cases of extreme temperature will increase the internal blade stress and reduce the stability of stress concentration positions [**76**].

Moisture exposure can lead to swelling, reduced mechanical properties, and increased susceptibility to delamination in composite materials [**77**]. Swelling can cause microcracking in resin weakened by hydrolysis, which contributes to interfacial debonding at the hydrolyzed interface and may accelerate physio-mechanical degradation. [**78-80**]. For instance, fiberglass can absorb water, which may degrade its mechanical properties over time [**81**]. Carbon fiber, on the other hand, is less hygroscopic but may still experience interfacial degradation if the matrix material is not moisture-resistant [**82**]. Advanced composites can be engineered with hydrophobic properties or protective barriers to mitigate moisture ingress, enhancing durability and lifespan [**83**].

Icing significantly impacts wind turbine performance and safety. The formation of ice on the blade alters its aerodynamic profile, reducing power output and potentially compromising structural integrity [**84-87**]. The severity of icing varies with temperature. Typically, it occurs between -6°C and -14°C, with streamlined icing prevalent at -20°C. The most vulnerable area is the blade tip and the region extending 70% towards the root [**88**]. Key parameters influencing icing severity include icing area, stationary thickness, and icing volume [**89**]. The shape of the ice accretion tends to be more pronounced near the blade tip. Between -16°C and -18°C, a hybrid ice shape, combining characteristics of both horn and streamlined icing, is often observed.

IV. INNOVATIVE MATERIALS AND TECHNOLOGIES

The ongoing quest for improved performance and sustainability in wind turbine blades has led to the exploration of innovative materials and technologies. Among these, bio-based composites and nanomaterials are gaining significant attention for their potential to enhance longevity and performance. This section explores these new materials and discusses recent advancements in material science that could further improve wind turbine blade design.

4.1 Exploration of New Materials

4.1.1 Bio-based Composites

Bio-based composites emerge as sustainable alternatives for wind turbine blades. They are made from renewable natural fibers like flax, jute, and hemp, combined with bio-resins. These materials offer reduced environmental impact, lower weight, and competitive mechanical properties compared to traditional synthetic materials. Studies have demonstrated that natural fibers provide adequate tensile and flexural strength while remaining lightweight, essential for minimizing gravitational loads and reducing tip deflection. For instance, flax blades have shown to be 10% lighter than glass fiber blades while maintaining durability under operational loads [**90**]. Hemp and graphene-coated jute fibers have also displayed mechanical properties comparable to or better than synthetic materials, with the added environmental benefit of carbon absorption [**91**].

However, challenges such as moisture absorption and variability in fiber properties pose obstacles to fully replacing synthetic composites. Hydrophilic natural fibers can weaken the fiber-matrix interface. Their mechanical properties may vary depending on environmental conditions and fiber extraction methods [**92**].

Chemical surface treatments and nanomaterial enhancements have been explored to improve adhesion between fibers and matrices, thereby enhancing the performance of bio-based composites [**91, 93-96**]. Research into bio-resins like Greenpoxy and EcoPoxy has also shown promise in improving the mechanical strength and sustainability of turbine blades, though these resins are not yet fully biodegradable [**97**].

Moreover, bio-inspired adhesive solutions combining mechanical interlocking and chemical bonding have been developed, mimicking natural structures like nacre [**98**]. These engineered adhesives not only enhance the strength and durability of the blade during operation but also allow for disassembly and reuse at the end of its lifecycle. By increasing shear modulus and damage tolerance through mechanisms like fiber bridging, these adhesives improve both the performance and sustainability of wind turbine blades, supporting longer lifespans and recyclability.

Future advancements will focus on improving fiber treatment, resin formulation, and optimizing fiber orientation to maximize strength and stiffness. Leveraging the mechanical advantages of bio-based composites, while drawing inspiration from natural materials with tough and resilient structures, could lead to more durable, efficient, and environmentally friendly wind turbine blades. These innovations aim to ensure the long-term reliability and sustainability of wind energy systems.

4.1.2 Nanomaterials

Nanomaterials, characterized by their unique properties at the nanoscale, are being explored for wind turbine blade applications. Incorporating nanomaterials, such as carbon nanotubes (CNTs) or graphene, into traditional composite matrices can significantly enhance mechanical properties, fatigue resistance, and thermal stability [**45**]. For instance, carbon nanotubes improve tensile strength and stiffness while reducing weight [**99, 100**], leading to more efficient and resilient blade designs [**101, 102**]. However, it should

be noted that CNTs have a significant impact on interlaminar fracture toughness and flexural strength, while their effects on tensile strength and stiffness are comparatively lower [**103**].

Additionally, nanomaterials provide enhanced resistance to moisture and environmental degradation, which helps extend the lifespan of blades [**104**]. Nanoparticles are commonly used as fillers or additives in surface coatings, incorporating materials like clay, carbon (such as SWCNT, MWCNT, and CNF), and glass fibers [**105, 106**]. Furthermore, specific nanomaterials such as Al_2O_3, SiO_2, and ZrO_2 are used to increase mechanical and scratch resistance, while CuO, TiO_2, and ZnO are employed to create antimicrobial surfaces. Nanoclay and graphene are also used to improve gas barrier properties [**105**], offering further protective benefits for the turbine blades.

Table 3: Material Properties of Bio-Based Composites and Nanomaterial Reinforcements for Wind Turbine Blades.

Material	Tensile Strength (MPa)	Young's Modulus (GPa)	Density (g/cm³)
Bio-based Composites (e.g., Flax/Jute/Hemp with Bio-Resin)	50–500	5–30	~1.2–1.5
Carbon Nanotubes (CNTs) – Single-Walled (SWCNT)	Up to 130,000	~1,000	~1.3
Carbon Nanotubes (CNTs) – Multi-Walled (MWCNT)	3,000–7,000	~600	~1.8
Graphene	Up to 130,000	~1,000	~1.3
Carbon Nanofibers (CNF)	~1,200	200–500	~1.3
Aluminum Oxide (Al_2O_3)	300–500	70–400	~3.9
Silicon Dioxide (SiO_2)	70–130	50–75	~2.2
Zirconium Dioxide (ZrO_2)	300–700	~200	~5.6
Copper Oxide (CuO)	70–100	50–70	~6.3
Titanium Dioxide (TiO_2)	30–60	~50	~4.2
Zinc Oxide (ZnO)	40–70	~60	~5.6
Nanoclay	30–90	1–10	~2.3

Recent studies have demonstrated that the addition of nanomaterials can improve interfacial bonding between fibers and matrices in composite materials. This enhanced bonding is critical in reducing delamination and strengthening the overall structural integrity of blades under the cyclic loading conditions typical in wind turbine operations. Even small amounts of CNTs (e.g., 0.2 wt%) have shown remarkable improvements, increasing fatigue life by over 1500% compared to traditional epoxy systems [**107**]. Moreover, CNTs improve fracture toughness by up to 60%, making the blades more resistant to crack propagation and mechanical failure under stress [**108**]. The large surface area and high aspect ratio of CNTs enable superior stress transfer, thereby enhancing overall durability. SiO_2 and Al_2O_3 nanocomposites with varying percentages of nanoparticles have also been fabricated and tested to assess their feasibility in wind turbine blade construction. According to the results [**109**], nanocomposites with 1% Al_2O_3 have demonstrated the highest tensile strength, fatigue resistance, and optimum hardness, marking them as a promising option for reinforcing wind turbine blade materials. Although manufacturing processes for nanocomposites can be complex and costly, ongoing advancements aim to optimize these processes, making them more viable for large-scale applications. As larger wind turbines are developed, the lightweight yet robust properties of CNT-based nanocomposites offer a promising solution for creating longer-lasting, high-performance blades that can withstand demanding environmental and mechanical loads over extended periods. The mechanical properties of bio-based composites and nanomaterials as well as the advantages and disadvantages of material properties for wind turbine blades are summarized in Table 3 and 4

Table., 4: Advantages and Disadvantages of Bio-Based and Nanomaterial-Reinforced Composites in Wind Turbine Blades.

Material	Advantages	Disadvantages
Bio-based Composites (e.g., Flax/Jute/Hemp with Bio-Resin)	Renewable, low-cost, lower environmental impact, biodegradability	Lower strength and durability than synthetic composites, potential for moisture absorption
Carbon Nanotubes (CNTs) – Single-Walled (SWCNT)	Extremely high strength, excellent electrical and thermal conductivity	Expensive, challenging to disperse in resins, inconsistent availability
Carbon Nanotubes (CNTs) – Multi-Walled (MWCNT)	High strength and flexibility, good electrical and thermal properties	Higher cost, more difficult to uniformly distribute
Graphene	Exceptional mechanical and thermal properties, increases resin strength and conductivity	Costly, difficult to disperse evenly, requires precise processing
Carbon Nanofibers (CNF)	Lightweight, high tensile strength, enhances durability and stiffness	Relatively expensive, agglomeration in resins
Aluminum Oxide (Al_2O_3)	High hardness, improves scratch resistance and thermal stability	Adds weight, cost may increase with higher loading
Silicon Dioxide (SiO_2)	Increases scratch resistance, chemical durability, and UV resistance	Adds density, performance highly dependent on resin dispersion
Zirconium Dioxide (ZrO_2)	Excellent mechanical reinforcement, high hardness, thermal resistance	Heavy, maybe costly, adds weight to the composite
Copper Oxide (CuO)	Antimicrobial properties, thermal stability	High density, potential health/environmental concerns
Titanium Dioxide (TiO_2)	Provides UV protection, antimicrobial properties, increases hardness	Increases composite density, requires careful handling
Zinc Oxide (ZnO)	UV-blocking and antimicrobial properties, improves weather resistance	Potential environmental concerns, limited strength contribution
Nanoclay	Increases stiffness, improves barrier properties, low cost	Can affect processing, relatively low mechanical strength

4.1.3 Recent Advancements in Material Science

Recent advancements in material science have also contributed significantly to enhancing wind turbine blade performance. One notable development is the application of advanced manufacturing techniques, such as additive manufacturing (3D printing), which allows for greater design flexibility and the creation of complex geometries that optimize aerodynamic performance [**101**]. These techniques enable the production of lightweight and structurally efficient components. This can reduce the overall weight of the blades and improve energy capture [**110**].

Another significant advancement is the development of smart materials that can respond to environmental stimuli. These materials can change properties in response to changes in temperature, moisture, or mechanical stress [**91**]. For example, incorporating self-healing polymers into blade materials can enable the repair of micro-cracks that may form during operation, extending the lifespan of the blades and reducing maintenance costs [**111**].

Furthermore, ongoing research into hybrid materials that combine the benefits of different material classes is showing promise. For instance, integrating bio-based fibers with advanced synthetic resins can create a composite that leverages the sustainability of natural materials while maintaining the superior performance characteristics of traditional composites [**112**]. These hybrid materials can lead to more sustainable wind turbine blades without compromising performance [**113**].

In conclusion, the exploration of innovative materials and technologies is pivotal for advancing the performance and sustainability of wind turbine blades. Bio-based composites and nanomaterials offer exciting possibilities for enhancing blade longevity, while recent advancements

in material science are paving the way for improved manufacturing processes and the development of smart materials [**101**]. As research continues to evolve, these innovations will play a crucial role in optimizing wind turbine design, ultimately contributing to the growth and reliability of renewable energy sources [**114**].

V. RISK ASSESSMENT

The risk assessment of wind turbine blades depends heavily on the choice of materials, as each material type presents distinct mechanical, environmental, and manufacturing-related risks. This section evaluates the risks associated with glass fiber reinforced polymer (GFRP), carbon nanotube (CNT) composites, natural fiber composites, carbon fiber reinforced polymer (CFRP), and hybrid composites, with attention to their implications for blade performance, environmental impact, and recyclability.

5.1 Mechanical Performance Risk

Each material used in wind turbine blades carries risks related to its mechanical behavior under operational stresses. Widely used due to its affordability and satisfactory strength (tensile strength ~1,100 MPa), GFRP still faces risks of fatigue and material degradation. These risks include potential blade failure due to dynamic loading or environmental exposure, such as UV radiation and saltwater, which can weaken the material over time. For example, GFRP blades installed offshore often degrade from moisture and saltwater, leading to crack propagation and delamination [**115**]. Inadequate risk assessments that fail to account for these environmental factors may result in premature blade failures, increasing repair costs and reducing turbine efficiency. CNT composites offer exceptional mechanical properties, including tensile strengths up to 7,000 MPa and superior fatigue resistance, potentially extending the operational lifespan of blades. However, long-term performance data for CNT composites is limited. There are concerns about their behavior under cyclic loads in harsh environments, introducing uncertainties regarding durability [**116**]. Premature failure due to unforeseen material degradation or fatigue poses a significant risk for CNT-based blades [**101**].

Natural fiber composites, such as flax fiber reinforced polymers, have tensile strengths ranging from 500-900 MPa, which limits their use to smaller, onshore turbines. The primary risk associated with these materials is their lower mechanical performance compared to synthetic fibers, increasing the likelihood of mechanical failure under high loads or fatigue over time. Moisture absorption is also a concern, as it can degrade the material's structural integrity [**117**].

CFRP, known for its high strength-to-weight ratio (tensile strength >3,500 MPa), is suitable for large offshore turbines. However, CFRP blades are prone to brittle failure without significant deformation, making any undetected flaws or stress concentrations critical risks that could lead to catastrophic failure. Additionally, despite its excellent fatigue resistance, the sudden and unpredictable nature of CFRP failures poses a significant safety risk in high-demand applications [**118**].

Hybrid composites, combining GFRP and CFRP, offer a balance of cost and mechanical performance (~2,500 MPa tensile strength). However, material incompatibility between fiberglass and carbon fibers can lead to internal stresses and delamination, particularly under cyclic loads. This presents a potential failure risk over time, especially in offshore applications where exposure to varying environmental conditions could exacerbate such issues [**119**].

5.2 Environmental Risk

The environmental impact of wind turbine blades, particularly concerning the materials used, is another critical factor in risk assessment. While cost-effective, GFRP blades produce significant CO2 emissions during production (5-7 kg CO2/kg) and are difficult to recycle at the end of their life. Most GFRP blades are disposed of in landfills, contributing to long-term environmental degradation [**120**]. Regulatory risks are also a concern, as future legislation may impose restrictions on landfill use or introduce stricter recycling mandates, which would increase the lifecycle cost and environmental burden of GFRP blades. CNT composites, despite their excellent performance characteristics, present significant environmental risks due to their high production energy demands (200+ MJ/kg) and the unresolved issue of nanomaterial toxicity in the environment [**121**]. The risks associated with their disposal or potential degradation in the environment are not fully understood, and their recyclability remains underdeveloped. This uncertainty creates a significant environmental risk in adopting CNT composites for large-scale turbine use [**122**].

Natural fiber composites, on the other hand, offer a more sustainable alternative with lower CO2 emissions during production (1-2 kg CO2/kg) and biodegradability at the end of their life [**123**]. The main environmental risks with natural fiber composites are related to resource sustainability, as large-scale production could pressure agricultural systems [**124**]. However, from a lifecycle perspective, these materials present the lowest environmental risks among the options considered.

CFRP is associated with high CO2 emissions during production (29 kg CO2/kg), largely due to the energy-intensive manufacturing process, which consumes up to 180 MJ/kg [**125**]. End-of-life disposal presents a significant risk, as the recyclability of CFRP is limited, and most blades are either incinerated or sent to landfills [**126**]. The long-term environmental risks of CFRP disposal, combined with potential regulatory shifts toward stricter environmental policies, present substantial challenges for the use of CFRP in wind turbine blades [**127**].

Hybrid composites mitigate some environmental risks by combining materials with lower production energy requirements, but they still face challenges in terms of recycling [**128**]. As hybrid blades reach the end of their operational life, the combination of different materials makes recycling difficult, and most blades will likely be landfilled or incinerated, contributing to environmental harm [**129**].

5.3 Manufacturing Risk

Manufacturing processes for wind turbine blade materials are complex and energy-intensive, introducing additional risks [**130**]. GFRP, produced through resin transfer molding (RTM) at energy levels of around 30 MJ/kg, is relatively straightforward to manufacture. Quality control during production is critical, as any defects could result in premature blade failure, increasing maintenance costs and reducing operational efficiency.

CNT composites present significant manufacturing risks due to the complexity and high energy demands of their production processes. Techniques such as high shear mixing and the incorporation of nanomaterials require precise control and specialized equipment [**131**]. The high cost and risk of manufacturing defects, such as inconsistent CNT dispersion, make these materials less appealing for large-scale production at present.

Natural fiber composites are less energy-intensive to produce (10-20 MJ/kg), but their production risks include inconsistent fiber quality and performance variability. Natural fibers are subject to environmental factors during growth, leading to batch-to-batch variations in mechanical properties [**132**]. Ensuring uniformity in the final composite is challenging, and poor-quality control during production could lead to blades with suboptimal performance or premature failure.

CFRP production is highly energy-intensive (150-180 MJ/kg) and involves complex processes such as high-temperature curing. Risks during manufacturing include fiber misalignment, incomplete resin curing, and the formation of voids, all of which can weaken the blade and reduce its lifespan [**133**]. The high costs and energy demand of CFRP production also introduce financial risks, particularly for large-scale offshore turbines, where cost efficiency is paramount [**134**].

Hybrid composites reduce some of the manufacturing complexities of CFRP but still require careful control of fiber alignment and resin curing. One risk is the potential for material incompatibility between the fiberglass and carbon fiber components, which can lead to internal stresses and delamination during operation. This necessitates stringent quality control measures to avoid defects that could compromise blade performance [**135**].

Each material used in wind turbine blades carries risks related to its mechanical behavior under operational stresses. GFRP, widely used due to its affordability and satisfactory strength (tensile strength ~1,100 MPa), still faces risks of fatigue and material degradation, especially under offshore conditions. These risks include potential blade failure due to dynamic loading or environmental exposure, such as UV radiation and saltwater, which can weaken the material over time. For example, GFRP blades installed offshore often degrade from moisture and saltwater, leading to crack propagation and delamination [**115**]. Inadequate risk assessments that fail to account for these environmental factors may result in premature blade failures, increasing repair costs and reducing turbine efficiency. CNT composites offer exceptional mechanical properties, including tensile strengths up to 7,000 MPa and superior fatigue resistance, potentially extending the operational lifespan of blades. However, long-term performance data for CNT composites is limited, and there are concerns about their behavior under cyclic loads in harsh environments, introducing uncertainties regarding durability [**116**]. Premature failure due to unforeseen material degradation or fatigue poses a significant risk for CNT-based blades [**101**].

Natural fiber composites, such as flax fiber reinforced polymers, have tensile strengths ranging from 500-900 MPa, which limits their use to smaller, onshore turbines. The primary risk associated with these materials is their lower mechanical performance compared to synthetic fibers, increasing the likelihood of mechanical failure under high loads or fatigue over time. Moisture absorption is also a concern, as it can degrade the material's structural integrity [**117**].

CFRP, known for its high strength-to-weight ratio (tensile strength >3,500 MPa), is suitable for large offshore turbines. However, CFRP blades are prone to brittle failure without significant deformation, making any undetected flaws or stress concentrations critical risks that could lead to catastrophic failure. Additionally, despite its excellent fatigue resistance, the sudden and unpredictable nature of

CFRP failures poses a significant safety risk in high-demand applications [**118**].

Hybrid composites, combining GFRP and CFRP, offer a balance of cost and mechanical performance (~2,500 MPa tensile strength). However, material incompatibility between fiberglass and carbon fibers can lead to internal stresses and delamination, particularly under cyclic loads. This presents a potential failure risk over time, especially in offshore applications where exposure to varying environmental conditions could exacerbate such issues [**117**].

VI. CONCLUSION

In summary, this study highlights the importance of material selection and design optimization in extending the lifespan of wind turbine blades. Traditional composites like glass fiber reinforced polymers (GFRP) and carbon fiber reinforced polymers (CFRP) continue to offer high strength-to-weight ratios and fatigue resistance. However, their environmental impact, particularly in terms of energy consumption during production and challenges in recyclability, remains a concern. Nanomaterials, such as carbon nanotubes (CNTs), present a promising pathway to enhance blade performance. These materials significantly improve mechanical properties, especially in terms of fatigue resistance and durability under cyclic loads. Despite these advancements, the high cost and complex manufacturing processes of nanomaterials pose barriers to large-scale adoption.

Bio-based composites, on the other hand, present a more sustainable alternative, with lower carbon footprints and potential for biodegradability. These materials offer comparable performance to GFRP in specific applications, particularly for small- to medium-sized turbines. The ongoing research into bio-based resins and improved fiber treatments further positions natural fiber composites as viable options for the future, although their mechanical limitations restrict their use in large, offshore turbines. From an environmental perspective, hybrid composites offer a middle ground by balancing the performance benefits of both fiberglass and carbon fiber while somewhat reducing the environmental burden of their production. However, recyclability challenges remain an issue for all synthetic composites. Moving forward, continued research and development in material science, particularly in enhancing the mechanical properties of bio-based materials and optimizing the production processes for nanocomposites, will be critical in achieving both high-performance wind turbine blades and sustainability goals. These advancements will greatly enhance the long-term viability of wind energy systems by boosting blade durability, lowering maintenance costs, and reducing the environmental impact of wind turbine components.

REFERENCES

[1] IPCC. Climate Change 2014: Mitigation of Climate Change. Contribution of Working Group III to the Fifth Assessment Report of the Intergovernmental Panel on Climate Change. Cambridge University Press, Cambridge, UK, 2014.

[2] High-Level Commission on Carbon Prices. Report of the High-Level Commission on Carbon Prices. World Bank, Washington, DC, USA, 2017.

[3] Carroll, J., McDonald, A., & McMillan, D. (2016). Failure rate, repair time and unscheduled O&M cost analysis of offshore wind turbines. Wind Energy, 19, 1107–1119. doi.org/10.1002/we.1887

[4] Mishnaevsky L., Jr. (2019). Repair of wind turbine blades: Review of methods and related computational mechanics problems. Renew. Energy, 140, 828–839. 10.1016/j.renene.2019.03.113

[5] Chen, X. (2018). Fracture of wind turbine blades in operation—Part I: A comprehensive forensic investigation. Wind Energy. 21, 1046–1063. doi.org/10.1002/we.2212

[6] Li D., Ho S.C.M., Song G., Ren L., Li H. (2015). A review of damage detection methods for wind turbine blades. Smart Materials and Structures. 24, 1–24. 10.1088/0964-1726/24/3/033001

[7] Boopathi, K., Mishnaevsky Jr., L., Sumantraa, B., Premkumar, S. A., Thamodharan, K., & Balaraman, K. (2022). Failure mechanisms of wind turbine blades in India: Climatic, regional, and seasonal variability. Wind Energy, *25*(5), 968-979. doi.org/10.1002/we.2706

[8] Mishnaevsky, L., & Hasager, Charlotte Bay & Bak, Christian & Tilg, Anna-Maria & Bech, Jakob I. & Doagou Rad, Saeed & Fæster, Søren (2021). Leading edge erosion of wind turbine blades: Understanding, prevention and protection, Renewable Energy, Elsevier, vol. 169(C), 953-969. 10.1016/j.renene.2021.01.044

[9] Herring R, Domenech L, Renau J, Šakalytė A, Ward C, Dyer K, Sánchez F. (2021). Assessment of a Wind Turbine Blade Erosion Lifetime Prediction Model with Industrial Protection Materials and Testing Methods. Coatings.11(7),767.doi.org/10.3390/coatings11070767

[10] Herring, R., Dyer, K., Martin, F., Ward, C. (2019). The increasing importance of leading edge erosion and a review of existing protection solutions. Renewable and Sustainable Energy Reviews, 115, 109382, doi.org/10.1016/j.rser.2019.109382

[11] Mishnaevsky L., Jr., Thomsen K. (2020). Costs of repair of wind turbine blades: Influence of technology aspects. Wind Energy, 23, 2247–2255. doi.org/10.1002/we.2552

[12] Unplanned Wind Turbine Repairs to Cost Industry $8 Billion+ in 2019. [(accessed on 11 April 2022)].

Available online: https://www.woodmac.com/press-releases

[13] Yinyao, Q., Xu, I., Zhang, Y. (2009). Bamboo as a potential material used for wind turbine blades, Technological and socio-Economic Planning Technical Report, Roskilde University, 1-55.

[14] Bakri, S. Chandrabakty, R. Alfriansyah, A. Dahyar, (2016). Potential coir fiber composite for small wind turbine blade application. International Symposium on Smart Material and Mechatronics, 2(1), 42-44, 107-109.10.20342/IJSMM.2.1.44

[15] Kishore, D., Inderdeep, S, Akshay Dvivedi, A., Kumar, P. (2013). Natural fiber reinforced polymer composite for wind turbine blades: Challenges and Opportunities. Recent Advances In Composite Materials For Wind Turbine Blade, 25-39.

[16] Thirumalai, D. (2012). Future Material For Wind Turbine Blades- A Critical Review, Section of Composites and Materials Mechanics, Department of Wind Energy, Technical University of Denmark.

[17] Banga, H. Singh, V.K., Sushil and Choudhary, K. Fabrication and study of mechanical properties of bamboo fiber reinforced Biocomposites. Innovative systems design and engineering, 6(1), 84-98, 2015.

[18] Brøndsted, P., Holmes, J.W., B.F. Sørensen, B.F. Bamboo Based Composites For Wind Turbine Blades. Materials Research Division, Risø DTU, The Technical University of Denmark.

[19] Abdul Nasir, A.A., Azmi, A.I.., A.N.M. Khalil, A.N.M. (2015). Measurement and optimization of residual tensile strength and delamination damage of drilled flax fibre reinforced composites. Measurement, 75(1), 298-307. doi.org/10.1016/j.measurement.2015.07.046

[20] www. Flax composites.com

[21] Sparnins, E. Mechanical properties of flax fiber and their composites, Division of Polymer Engineering Department of Materials and Manufacturing Engineering Luleå University of Technology, 2006.

[22] Vijaya Kumar, K., Safiulla, M., Khaleel Ahmed, A.N. (2013). An Experimental Evaluation of Fiber Reinforced Polypropylene Thermoplastics For Aerospace Applications. Journal of Mechanical Engineering, 43(2), 92-97. 10.3329/jme.v43i2.17832

[23] Velmurugan, G., Venkatesan, S.P., Prakash, P.V., Sathish Kumar, N., Vijaya Kumar, N. (2014). Mechanical Testing of Hybrid Composite Material. International Journal of Scientific and Research Publications, 4(7), 1-6. http://www.ijsrp.org/research-paper-0714.php?rp=P312890

[24] Bortolotti, P. (2012). Carbon Glass Hybrid Materials For Wind Turbine Rotor Blades, wind turbine materials and constructions.

[25] Girish, K. G., Anil, K. C., & Akash. (2014). Mechanical Properties of Jute and Hemp Reinforced Epoxy/Polyester Hybrid Composites. International Journal of Research in Engineering & Technology, 2(4), 245-248.

[26] Yang, J. (2012). Carbon Nanotubes Reinforced Composites for Wind Turbine Blades. Department of Macromolecular Science and Engineering, Case Western Reserve University.

[27] Loos, M., Yang, J., Feke, D., & Manas-Zloczower, I. (n.d.). Carbon Nanotubes in Wind Turbine Blades. Society of Plastic Engineers. doi:10.1002/spepro.004173.

[28] Mittal, V. (n.d.). (2010). Polymer Nanocomposites: Synthesis, Microstructure, and Properties. 10.1002/9783527629275.ch1

[29] Ahmed, M., Hasnain, S.-U., Khan, W. A., & Ahmed, Z. (2012). Improving Wind Turbine Performance Using Nano Materials. University of South Asia, Lahore.

[30] Bhanushali, H., & Bradford, P. D. (2016). Woven Glass Fiber Composites with Aligned Carbon Nanotube Sheet Interlayers. Journal of Nanomaterials, 2016, Article ID 9705257.

[31] Van Rijswijk, K. (2007). Thermoplastic Composite Wind Turbine Blades (Doctoral dissertation, Technical University of Delft, Netherlands).

[32] Mishnaevsky, L., Jr., & Brøndsted, P. (2009). Statistical Modelling of Compression and Fatigue Damage of Unidirectional Fiber Reinforced Composites. Composites Science and Technology, 69, 477–484. doi.org/10.1016/j.compscitech.2008.11.024

[33] Lamhour, K., Rouway, M., Tizliouine, A., Omari, L. E. H., Salhi, H., & Cherkaoui, O. (2022). Experimental Study on the Properties of Alfa/Wool Woven Fabrics Reinforced Epoxy Composite as an Application in Wind Turbine Blades. Journal of Composite Materials, 56, 3253–3268. doi.org/10.1177/00219983221111493

[34] Rajad, O.; Mounir, H.; El Marjani, A.; Fertahi, S.E.-D. (2022). Nonlinear Modeling Analysis of the Coupled Mechanical Strength and Stiffness Enhancement of Composite Materials of a Horizontal Axis Wind Turbine Blade (HAWTB). International Journal on Interactive Design and Manufacturing. 16, 469–492 doi:10.1007/s12008-021-00790-0

[35] Grande, J.A. (2008) Wind Power Blades Energize Composites Manufacturing. Plastics Technology. https://www.ptonline.com/articles/wind-power-blades-energize-composites-manufacturing

[36] Carbon Fiber vs. Fiberglass: A Comparison between the Two Materials Which Material Is Superior? Available online: https://infogr.am/carbon-fiber-vs-fiberglass (accessed on 8 November 2017).

[37] Haberkern, H. (2006). Tailor-made reinforcements. Reinforced Plastics, 50(4), 28–33. doi:10.1016/S0034-3617(06)70974-2

[38] Mengal, A.N.; Karuppanan, S.; Wahab, A.A. (2014). Basalt Carbon Hybrid Composite for Wind Turbine Rotor Blades: A Short Review. *Advanced Materials. Research, 970*, 67–73. doi:10.4028/www.scientific.net/AMR.970.67

[39] Abashidze, S.; Marquis, F.D.; Abashidze, G.S. Hybrid fiber and nanopowder reinforced composites for wind turbine blades. Journal of Materials Research and Technology, 4, 60–67. doi:10.1016/j.jmrt.2015.01.002

[40] Ong, C.-H.; Tsai, S.W. The Use of Carbon Fibers in Wind Turbine Blade Design: A SERI-8 Blade Example. SAND2000-0478; Sandia National Laboratories

Contractor Report; Sandia NL: Albuquerque, NM, USA, 2000.

[41] Wind Power Monthly Webpage. Available online: https://www.windpowermonthly.com/article/1419306/turbines-year-rotor-blades (accessed on 8 November 2017).

[42] Holmes, J.W.; Sørensen, B.F.; Brøndsted, P. Reliability of Wind Turbine Blades: An Overview of Materials Testing. In Proceedings of the Wind Power Shanghai 2007, Shanghai, China, 1–3 November 2007.

[43] Holmes, J.W.; Brøndsted, P.; Sørensen, B.F.; Jiang, Z.H.; Sun, Z.H.; Chen, X.H. (2009). Development of a Bamboo-Based Composite as a Sustainable Green Material for Wind Turbine Blades. Journal of Wind Engineering and Industrial Aerodynamics, 33, 197–210. doi.org/10.1260/030952409789141053

[44] Pender, K.; Bacharoudis, K.; Romoli, F.; Greaves, P.; Fuller, J. (2024). Feasibility of Natural Fibre Usage for Wind Turbine Blade Components: A Structural and Environmental Assessment. Sustainability, 16(13), 5533. doi.org/10.3390/su16135533

[45] Mishnaevsky, L.; Branner, K.; Petersen, H.N.; Beauson, J.; McGugan, M.; Sørensen, B.F. (2017). Materials for Wind Turbine Blades: An Overview. Materials, 10(11), 1285. doi.org/10.3390/ma10111285

[46] Pinto, T.H.L.; Gul, W.; Torres, L.A.G.; Cimini, C.A., Jr.; Ha, S.K. (2021). Experimental and Numerical Comparison of Impact Behavior between Thermoplastic and Thermoset Composite for Wind Turbine Blades. Materials, 14(21), 6377. doi.org/10.3390/ma14216377

[47] Arrese, A.; Carbajal, N.; Vargas, G.; Mujika, F. (2010). A New Method for Determining Mode II R-Curve by the End-Notched Flexure Test. Engineering Fracture Mechanics, 77(1), 51–70. doi:10.1016/j.engfracmech.2009.09.008

[48] Gracia, J.D.; Boyano, A.; Arrese, A.; Mujika, F. (2015). A New Approach for Determining the R-Curve in DCB Tests without Optical Measurements. Engineering Fracture Mechanics, 135, 274–285. doi.org/10.1016/j.engfracmech.2015.01.016

[49] Boyano, A.; Lopez-Guede, J.M., Torre-Tojal, L., Fernandez-Gamiz, U., Zulueta, E., Mujika, F. (2021) Delamination Fracture Behavior of Unidirectional Carbon Reinforced Composites Applied to Wind Turbine Blades. Materials, 14(3), 593. doi.org/10.3390/ma14030593

[50] Overgaard, L.C.T.; Lund, E. (2010). Structural Collapse of a Wind Turbine Blade. Part B: Progressive Interlaminar Failure Models. Composites Part A Applied Science and Manufacturing, 41(2), 271–283. doi:10.1016/j.compositesa.2009.10.012

[51] Haselbach, P.U.; Bitsche, R.D.; Branner, K. (2016) The Effect of Delaminations on Local Buckling in Wind Turbine Blades. Renewable Energy, *85*, 295–305. doi:10.1016/j.renene.2015.06.053

[52] He, K., Hoa, S.V., & Ganesan, R. (2000). The study of tapered laminated composite structures: A review. Composite Science and Technology, 60(14), 2643–2657.doi:10.1016/S0266-3538(00)00138-X

[53] Seyed, A.R.H., & Johnny, J. (2016). Local fatigue behavior in tapered areas of large offshore wind turbine blades. In Madsen, B., Biel, A., Kusano, Y., Lilholt, H., Mikkelsen, L.P., Mishnaevsky, L., Jr., & Sørensen, B.F. (Eds.), Proceedings of the 37th Risø International Symposium on Materials Science (pp. 237–244). IOP Publishing: Bristol, UK.

[54] Cairns, D.S., Mandell, J.F., Scott, M.E., & Maccagnano, J.Z. (1999). Design and manufacturing considerations for ply drops in composite structures. Composite Part B: Engineering, *30*, 523–534. doi.org/10.1016/S1359-8368(98)00043-2

[55] Samborsky, D.D., Wilson, T.J., Agastra, P., & Mandell, J.F. (2008). Delamination at thick ply drops in carbon and glass fiber laminates under fatigue loading. Journal of Solar Energy Engineering, 130(3), 031001. doi:10.1115/1.2931496

[56] Mendonça, H.G., Mikkelsen, L.P., Zhang, B., Allegri, G., & Hallett, S.R. (2023). Fatigue delaminations in composites for wind turbine blades with artificial wrinkle defects. International Journal of Fatigue, 175(10), 107822. doi:10.1016/j.ijfatigue.2023.107822

[57] Wang, J., Potter, K.D., Hazra, K., & Wisnom, M.R. (2012). Experimental fabrication and characterization of out-of-plane fiber waviness in continuous fiber-reinforced composites. Journal of Composite Materials, 46(17), 2041–2053. doi:10.1177/0021998311429877

[58] Thor, M., Mandel, U., Nagler, M., Maier, F., Tauchner, J., & Sause, M.G. et al. (2021). Numerical and experimental investigation of out-of-plane fiber waviness on the mechanical properties of composite materials. International Journal of Material Forming, 14(20), 19–37. doi:10.1007/s12289-020-01540-5

[59] Mukhopadhyay, S., Jones, M.I., & Hallett, S.R. (2015). Compressive failure of laminates containing an embedded wrinkle; experimental and numerical study. Composites A, 73, 132–142. doi.org/10.1016/j.compositesa.2015.03.012

[60] Lee, H.G., Kang, M.G., & Park, J.S. (2015). Fatigue failure of a composite wind turbine blade at its root end. Composite Structures, 133, 878–885. doi:10.1016/j.compstruct.2015.08.010

[61] Bringi, V.N., Chandrasekar, V., Hubbert, J., Gorgucci, E., Randeu, W.L., & Schoenhuber, M. (2003). Raindrop size distribution in different climatic regimes from disdrometer and dual-polarized radar analysis. Journal of Atmospheric Sciences, 60, 354–365. doi:10.1175/1520-0469

[62] Kathiravelu, G., Lucke, T., & Nichols, P. (2016). Rain drop measurement techniques: A review. Water Switzerland, 8(1), 29. doi.org/10.3390/w8010029

[63] Das, S., & Chatterjee, C. (2018). Rain characterization based on maritime and continental origin at a tropical location. Journal of Atmospheric and Solar-Terrestrial Physics, 173, 109–118. doi:10.1016/j.jastp.2018.02.011

[64] Montopoli, M., Vulpiani, G., Anagnostou, M.N., Anagnostou, E.N., & Marzano, F.S. (2007). Processing disdrometer raindrop spectra time series from various

climatological regions using estimation and autoregressive methods. International Geoscience and Remote Sensing Symposium (IGARSS), 2268–2271.

[65] Suh, S.-H., You, C.-H., & Lee, D.-I. (2016). Climatological characteristics of raindrop size distributions in Busan, Republic of Korea. Hydrology and Earth System Sciences, 20, 193–207. doi.org/10.5194/hess-20-193-2016

[66] Seela, B.K., Janapati, J., Lin, P.-L., Wang, P.K., & Lee, M.-T. (2018). Raindrop size distribution characteristics of summer and winter season rainfall over North Taiwan. Journal of Geophysical Research: Atmospheres 123(20), 11602-11624.doi.org/10.1029/2018JD028307

[67] Wen, L., Zhao, K., Wang, M.Y., & Zhang, G.F. (2019). Seasonal variations of observed raindrop size distribution in East China. Advances in Atmospheric Sciences, 36(4), 346–362. doi:10.1007/s00376-018-8107-5

[68] Amirzadeh, B., Louhghalam, A., Raessi, M., & Tootkaboni, M. (2017). A computational framework for the analysis of rain-induced erosion in wind turbine blades, part I: stochastic rain texture model and drop impact simulations. Journal of Wind Engineering and Industrial Aerodynamics, 163, 33–43. doi.org/10.1016/j.jweia.2016.12.006

[69] Mishnaevsky, L., Tempelis, A., Kuthe, N., & Mahajan, P. (2023). Recent developments in the protection of wind turbine blades against leading edge erosion: Materials solutions and predictive modelling. Renewable Energy, 215(5), 118966. doi:10.1016/j.renene.2023.118966

[70] Papanicolaou, G., Charitidis, P., Mouzakis, D., & Jiga, G. (2016). Experimental and numerical investigation of unbalanced boron/epoxy-aluminum single lap joints subjected to a corrosive environment. Journal of Composite Materials, 50(2), 145–157. doi.org/10.1177/0021998315571773

[71] Papanicolaou, G.C., Charitidis, P., Mouzakis, D.E., Karachalios, E., Jiga, G., & Portan, D.V. (2016). Experimental and numerical investigation of balanced Boron/Epoxy single lap joints subjected to salt spray aging. International Journal of Adhesion and Adhesives, 68, 9–18. doi.org/10.1016/j.ijadhadh.2016.01.009

[72] Finnegan, W., Flanagan, M., Ó Coistealbha, R., Dasan Keeryadath, P., Meier, P., Chi Hung, L., Flanagan, T., & Goggins, J. (2021). A novel solution for preventing leading edge erosion in wind turbine blades. Journal of Structural Integrity and Maintenance, 6(3), 136–147. doi:10.1080/24705314.2021.1906091

[73] Cortés, E., Sánchez, F., Domenech, L., Olivares, A., Young, T.M., & O'Carroll, A. (2017). Manufacturing issues which affect coating erosion performance in wind turbine blades. In AIP Conference Proceedings, 1896, p. 030023. doi:10.1063/1.5008010

[74] Rad, S.D., & Mishnaevsky, L., Jr. (2020). Rain erosion of wind turbine blades: Computational analysis of parameters controlling the surface degradation. Meccanica, 55(11), 725–743. doi:10.1007/s11012-019-01089-x

[75] Budinski, K.G. (2007). Guide to friction, wear and erosion testing. ASTM International.

[76] Yang, J., & Wenjun, Q. (2012). Effect of Extreme Temperature on The Performance of Wind Turbine Blade. Key Engineering Materials, 522, 457–461. doi:10.4028/www.scientific.net/KEM.522.457

[77] Hassanpour, B., & Karbhari, V.M. (2024). Characteristics and Models of Moisture Uptake in Fiber-Reinforced Composites: A Topical Review. Polymers, 16(16), 2265. Hassanpour, B., & Karbhari, V.M. (2024). doi.org/10.3390/polym16162265

[78] Sousa, J.M., Correia, J.R., & Cabral-Fonseca, S. (2016). Durability of glass fibre reinforced polymer pultruded profiles: Comparison between QUV accelerated exposure and natural weathering in a Mediterranean climate. Experimental Techniques, 40(1), 207–218. doi:10.1007/s40799-016-0024-x

[79] Cabral-Fonseca, S., Correia, J.R., Rodrigues, M.P., & Branco, F.A. (2012). Artificial accelerated ageing of GFRP pultruded profiles made of polyester and vinylester resins: Characterisation of physical–chemical and mechanical damage. Strain, 48, 162–173. doi: 10.1111/j.1475-1305.2011.00810.x

[80] Grammatikos, S.A., Zafari, B., Evernden, M.C., Mottram, J.T., & Mitchels, J.M. (2015). Moisture uptake characteristics of a pultruded fibre reinforced polymer flat sheet subjected to hot/wet aging. Polymer Degradation and Stability, 121, 407–419. doi:10.1016/j.polymdegradstab.2015.10.001

[81] Tefera, G., Bright, G., & Adali, S. (2024). Influence of Long-Term Moisture Exposure and Temperature on the Mechanical Properties of Hybrid FRP Composite Specimens. Journal of Composite Science, 8(8), 312. doi.org/10.3390/jcs8080312

[82] Aranha, R., Filho, M.A.A., Santos, C.L., de Andrade, T.H.F., Fonseca, V.M., Rivera, J.L.V., dos Santos, M.A., de Lima, A.G.B., de Amorim, W.F. Jr., & de Carvalho, L.H. (2024). Effect of Water Absorption and Stacking Sequences on the Tensile Properties and Damage Mechanisms of Hybrid Polyester/Glass/Jute Composites. Polymers, 16(7), 92. doi.org/10.3390/polym16070925

[83] Mokobia, K., Jonathan, E.M., Oyiborhoro, G., Maliki, M., & Ifijen, I.H. (2024). Environmental Degradation of Polymer-Based Composite Materials: Challenges and Mitigation Strategies. In TMS 2024 153rd Annual Meeting & Exhibition Supplemental Proceedings, The Minerals, Metals & Materials Series. Springer, Cham. doi:10.1007/978-3-031-50349-8_106

[84] Zhang, Y., Liu, K., Xian, H., et al. (2018). A review of methods for vortex identification in hydroturbines. Renewable and Sustainable Energy Reviews, 81, 1269–1285.doi: 10.1016/j.rser.2017.05.058

[85] Zeng, J., & Song, B. (2017). Research on experiment and numerical simulation of ultrasonic de-icing for wind turbine blades. Renewable Energy, 113, 706–712. doi: 10.1016/j.renene.2017.06.045

[86] Ruff, G.A. (2002). Quantitative comparison of ice accretion shapes on airfoils. Journal of Aircraft, 39, 418–426. doi: 10.2514/2.2967

[87] Hu, L., Zhu, X., Chen, J., et al. (2018). Numerical simulation of rime ice on NREL phase VI blade. Journal of Wind Engineering and Industrial Aerodynamics, 178, 57–68.

[88] Li, Y., Sun, C., Jiang, Y., Yi, X., Xu, Z., & Guo, W. (2018). Temperature effect on icing distribution near blade tip of large-scale horizontal-axis wind turbine by numerical simulation. Advances in Mechanical Engineering, 10(11), 1-13. doi:10.1177/1687814018812247

[89] Wang, S. (2017). Numerical simulation and icing wind tunnel test study on icing distribution on rotating blade of horizontal axis wind turbine. Northeast Agricultural University, Harbin, China.

[90] Shah, D., Schubel, P., & Clifford, M. (2013). Can flax replace E-glass in structural composites? A small wind turbine blade case study. Composites Part B: Engineering, 52, 172–181. doi.org/10.1016/j.compositesb.2013.04.027

[91] Karim, N., Sarker, F., Afroj, S., Zhang, M., Potluri, P., & Novoselov, K.S. (2021). Sustainable and multifunctional composites of graphene-based natural jute fibers. Wiley Online Library. doi:10.1002/adsu.202000228

[92] Ku, H., Wang, H., Pattarachaiyakoop, N., & Trada, M. (2011). A review on the tensile properties of natural fiber reinforced polymer composites. Composites Part B: Engineering, 42(4), 856-873. doi:10.1016/j.compositesb.2011.01.010

[93] Ngo, T.-D. (2017). Natural fibers for sustainable bio-composites. IntechOpen. doi: 10.5772/intechopen.71012

[94] Midani, M. (2019). Natural fiber composites: What's holding them back? CompositesWorld.

[95] Shivamurthy, B., Naik, N., Thimappa, B.H.S., & Bhat, R. (2020). Mechanical property evaluation of alkali-treated jute fiber reinforced bio-epoxy composite materials. Manipal Academy of Higher Education, Manipal, India. doi:10.1016/j.matpr.2020.04.016

[96] Shalwan, A., & Yousif, B.F. (2013). In state of art: Mechanical and tribological behaviour of polymeric composites based on natural fibres. Materials & Design, 48, 14-24. doi:10.1016/j.matdes.2012.07.014

[97] Bertomeu, D., García-Sanoguera, D., Fenollar, O., Boronat, T., & Balart, R. (2012). Use of eco-friendly epoxy resins from renewable resources as potential substitutes of petrochemical epoxy resins for ambient cured composites with flax reinforcements. Wiley Online Library.doi.org/10.1002/pc.22192

[98] Mishnaevsky, L., Jr., Jafarpour, M., Krüger, J., & Gorb, S.N. (2023). A New Concept of Sustainable Wind Turbine Blades: Bio-Inspired Design with Engineered Adhesives. Biomimetics, 8(6), 448. doi.org/10.3390/biomimetics8060448

[99] Merugula, L., Khanna, V., & Bakshi, B.R. (2012). Reinforced Wind Turbine Blades—An Environmental Life Cycle Evaluation. Environmental Science & Technology, 46(17), 9785–9792. doi:10.1021/es301343p

[100] Merugula, L.V., Khanna, V., & Bakshi, B.R. (2010). Comparative life cycle assessment: Reinforcing wind turbine blades with carbon nanofibres. In Proceedings of the 2010 IEEE Symposium on Sustainable Systems and Technology, Washington, DC, USA, 1–6. doi:10.1109/ISSST.2010.5507724

[101] Firoozi, A.A., Firoozi, A.A., & Hejazi, F. (2024). Innovations in Wind Turbine Blade Engineering: Exploring Materials. Sustainability, and Market Dynamics. Sustainability, 16(19), 8564. doi.org/10.3390/su16198564

[102] Ma, P.-C., & Zhang, Y. (2014). Perspectives of carbon nanotubes/polymer nanocomposites for wind blade materials. Renewable and Sustainable Energy Reviews, 30, 651–660. doi:10.1016/j.rser.2013.11.008

[103] Dıez-Pascual, A.M., Naffakh, M., Marco, C., Gomez-Fatou, M.A., & Ellis, G.J. (2014). Multiscale fiber-reinforced thermoplastic composites incorporating carbon nanotubes: A review. Current Opinion in Solid State and Materials Science, 18(2), 62–80. doi:10.1016/j.cossms.2013.06.003

[104] Frost-Jensen Johansen, N., Mishnaevsky, L., Jr., Dashtkar, A., Williams, N.A., Fæster, S., Silvello, A., Cano, I.G., & Hadavinia, H. (2021). Nanoengineered Graphene-Reinforced Coating for Leading Edge Protection of Wind Turbine Blades. Coatings, 11(9), 1104. doi.org/10.3390/coatings11091104

[105] Joshi, M., & Chatterjee, U. (2016). Polymer nanocomposite: an advanced material for aerospace applications. In Advanced Composite Materials for Aerospace Engineering: Processing, Properties, and Applications, 241.

[106] Slot, H.M., Gelinck, E.R.M., Rentrop, C., & van der Heide, E. (2015). Leading edge erosion of coated wind turbine blades: Review of coating life models. Renewable Energy, 80, 837–848. doi: 10.1016/j.renene.2015.02.036

[107] Loos, M., Yang, J., Feke, D., & Manas-Zloczower, I. (2012). Carbon nanotube-reinforced epoxy composites for wind turbine blades. Plastics Research Online.

[108] Gupta, N., Gupta, S.M., & Sharma, S.K. (2019). Carbon nanotubes: synthesis, properties and engineering applications. Carbon Letters, 29(5), 419–447. doi:10.1007/s42823-019-00068-2

[109] Muhammed, K.A., Kannan, C.R., & Stalin, B. (2020). Performance analysis of wind turbine blade materials using nanocomposites. Materials Today: Proceedings, 33(7), 4353–4361. doi:10.1016/j.matpr.2020.07.578

[110] Windcycle Energy (n.d.). Wind Turbine Technology: A Deep Dive into Blade Designs and Materials. Windcycle Energy Blog. Retrieved from https://windcycle.energy/wind-turbine-technology-2/

[111] Carron, W.S., Snowberg, D., Murdy, P., Hughes, S. (2023). Using Large-Scale Additive Manufacturing for Wind Turbine Blade Core Structures. National Renewable Energy Laboratory, Technical Report NREL/TP-5000-85673.

[112] National Renewable Energy Laboratory (NREL). (2021). NREL Explores Innovative Manufacturing Approach for

Next-Generation Wind Turbine Blades: Three-Dimensional Printing of Thermoplastic Blades Enables Thermal Welding, Improves Recyclability.

[113] Mishnaevsky Jr., L., Jafarpour, M., Krüger, J., Gorb, S.N. (2023). A New Concept of Sustainable Wind Turbine Blades: BioInspired Design with Engineered Adhesives. Biomimetics, 8(6), 448.

[114] National Renewable Energy Laboratory (NREL). (2021). NREL Explores Innovative Manufacturing Approach for Next Generation Wind Turbine Blades. Retrieved from NREL website.

[115] Rasool, G., Middleton, A.C., Stack, M.M. (2020). Mapping Raindrop Erosion of GFRP Composite Wind Turbine Blade Materials: Perspectives on Degradation Effects in Offshore and Acid Rain Environmental Conditions. ASME Journal of Tribology, 142(6), 061701.doi.org/10.1115/1.4046014

[116] Jang, Y.J., Jin, J.W., Lee, J.H., et al. (2020). Long-term durability of offshore wind turbine composite blades based on nonlinear load behavior due to pitch movement. Journal of Mechanical Science and Technology, 34, 2347–2355. doi.org/10.1007/s12206-020-0511-y

[117] Teng, H., Li, S., Cao, Z., Li, S., Li, C., Ko, T.J. (2023).Carbon Fiber Composites for Large-Scale Wind Turbine Blades: Applicability Study and Comprehensive Evaluation in China. Journal of Marine Science and Engineering, 11(3), 624. doi.org/10.3390/jmse11030624

[118] Ennis, B.L., Kelley, C.L., Naughton, B.T., Norris, R.E., Das, S., Lee, D. (2019). Optimized Carbon Fiber Composites in Wind Turbine Blade Design. Sandia Report SAND2019-14173.

[119] Yavuz, H. (2022). Hybrid Composites for Very Large Lightweight Wind Turbine Blades: Structural and Materials Aspects. In: Mazlan, N., Sapuan, S., Ilyas, R. (eds) Advanced Composites in Aerospace Engineering Applications. Springer, Cham. doi:10.1007/978-3-030-88192-4_21

[120] Jensen, J.P., Skelton, K. (2018). Wind turbine blade recycling: Experiences, challenges and possibilities in a circular economy. Renewable and Sustainable Energy Reviews, 97, 165-176. doi.org/10.1016/j.rser.2018.08.041

[121] Kim, M., Goerzen, D., Jena, P.V., et al. (2024). Human and environmental safety of carbon nanotubes across their life cycle. Nature Reviews Materials, 9, 63–81. doi:10.26434/chemrxiv-2023-psth7

[122] Jackson, P., Jacobsen, N.R., Baun, A., et al. (2013). Bioaccumulation and ecotoxicity of carbon nanotubes. Chemistry Central Journal, 7, 154. doi.org/10.1186/1752-153X-7-154

[123] de Beus, N., Carus, M., Barth, M. (2019). Carbon Footprint and Sustainability of Different Natural Fibres for Biocomposites and Insulation Material − Full Version (Update 2019).

[124] Nagaraja, S., Anand, P.B., Kumar, M.K., Ammarullah, M.I. (2024). Synergistic advances in natural fibre composites: A comprehensive review of eco-friendly bio-composite development, characterization, and diverse applications. Royal Society of Chemistry, 14, 28594-17611. doi.org/10.1039/D4RA00149D

[125] U.S. Department of Energy (DOE). (2017). Bandwidth Study on Energy Use and Potential Energy Saving Opportunities in U.S. Carbon Fiber Reinforced Polymer Manufacturing. DOE/EE-1662.

[126] Wu, J., Gao, X., Wu, Y., Wang, Y., Nguyen, T.T., Guo, M. (2023). Recycling Carbon Fiber from Carbon Fiber-Reinforced Polymer and Its Reuse in Photocatalysis: A Review. Polymers, 15(1), 170. doi.org/10.3390/polym15010170

[127] Meier, U. (2020). Sustainability of Carbon Fiber-Reinforced Polymers in Construction. In: Bumajdad, A., Bouhamra, W., Alsayegh, O., Kamal, H., Alhajraf, S. (eds) Gulf Conference on Sustainable Built Environment. Springer, Cham.

[128] Moahanty, A.K., Vivekanandhan, S., Pin, J.-M., Misra, M. (2018). Composites from renewable and sustainable resources: Challenges and innovations. Science, 362(6414), 536-542. doi: 10.1126/science.aat9072

[129] Korniejenko, K., Kozub, B., Bąk, A., Balamurugan, P., Uthayakumar, M., Furtos, G. (2021). Tackling the Circular Economy Challenges—Composites Recycling: Used Tyres, Wind Turbine Blades, and Solar Panels. Journal of Composite Science, 5(9), 243. doi:10.3390/jcs5090243

[130] Rajak, D.K., Wagh, P.H., Linul, E. (2021). Manufacturing Technologies of Carbon/Glass Fiber-Reinforced Polymer Composites and Their Properties: A Review. *Polymers*, 13(21), 3721. doi.org/10.3390/polym13213721

[131] Choudhary, M., Sharma, A., Raj, S.A., Hameed, M.T., Hui, D., Shah, A.U.M. (2022). Contemporary review on carbon nanotube (CNT) composites and their impact on multifarious applications. *Nanotechnology Reviews*, 11(1), 2632-2660. doi:10.1515/ntrev-2022-0146

[132] Gholampour, A., Ozbakkaloglu, T. (2020). A review of natural fiber composites: properties, modification and processing techniques, characterization, applications. Journal of Materials Science, 55, 829–892. doi.org/10.1007/s10853-019-03990-y

[133] Hannan, A.N., Seidlitz, H., Hartung, D., et al. (2024). Sustainability and Circular Economy in Carbon Fiber-Reinforced Plastics. Materials Circular Economy, 6, 26. doi.org/10.1007/s42824-024-00111-2

[134] Liu, W., Huang, H., Liu, Y., et al. (2021). Life cycle assessment and energy intensity of CFRP recycling using supercritical N-butanol. Journal of Materials Cycles and Waste Management, 23, 1303–1319. doi:10.1007/s10163-021-01206-7

[135] Binetruy, C., Michaud, V. (2021). Emerging, hybrid & smart composites. Functional Composite Materials, 2, 16. doi.org/10.1186/s42252-021-00028-y

International Journal of Advanced Engineering Research and Science (IJAERS)
Peer-Reviewed Journal
ISSN: 2349-6495(P) | 2456-1908(O)
Vol-11, Issue-11; Nov, 2024
Journal Home Page Available: https://ijaers.com/
Article DOI: https://dx.doi.org/10.22161/ijaers.1111.6

WSIC Criterion for Decomposition Level Selection of Orthogonal Wavelet Transform

Yimei Zheng[1], Cheng Liu[*2], Yan Fang[3]

[1,2]School of Mathematics, Southwest Jiaotong University, Chengdu 611756, China
1554047784@qq.com
[3]School of Electrical Engineering, Southwest Jiaotong University, Chengdu 611756, China
*Corresponding author

Received: 10 Oct 2024,

Receive in revised form: 12 Nov 2024,

Accepted: 18 Nov 2024,

Available online: 24 Nov 2024

***Keywords*— Wavelet Transform, Decomposition Level, Model Selection, WSIC**

***Abstract*—** *Wavelet transform is a widely used method in the field of signal analysis, and its application effect depends largely on the selection of wavelet decomposition level. In view of the unknown original signal, this paper transforms the selection of wavelet decomposition level into a model selection problem through statistical modeling, and then analyzes and presents wavelet selection information criteria (WSIC) of orthogonal wavelet transform level selection from the perspective of model selection. Finally, simulation experiments are conducted to verify and compare the effect of the WSIC information criteria with AIC and BIC criteria on wavelet level selection. The results show that the level accuracy of WSIC is up to 15.1% higher than that of AIC criterion and up to 14.3% higher than that of BIC criterion, indicating that WSIC criterion has better stability in selecting wavelet decomposition level than that of AIC and BIC criterion in existing literatures.*

I. INTRODUCTION

Wavelet transform is widely used in the field of signal analysis. It is a linear transform with wavelet function as its kernel. In the practical application of orthogonal wavelet transform, the signal containing noise is decomposed into different frequency components according to Mallat algorithm. In the signal reconstruction, some high frequency detail coefficients related to noise are set to zero, and the reconstructed signal after noise removal is obtained. The larger the level of wavelet decomposition, the more beneficial to noise removal, but will also lose more detailed signals, which may cause signal distortion. The smaller the level of wavelet decomposition, the noise can't be well eliminated. Therefore, in the process of using wavelet transform, choosing a suitable decomposition level is the key to improve the effect of wavelet denoising.

Under the condition that the original signal is known, the signal after wavelet transformation is usually compared with the original signal, and the optimal wavelet decomposition level is selected according to various evaluation indicators [1,2,3,4]. Under the condition that the original signal is unknown, only the observed signal containing noise can't be compared with the original signal after wavelet transform. Literature [5] uses blind estimation of SNR to analyze the changes of SNR and SNR gain by improving the index of SNR and SNR gain, and then evaluates the denoising effect of wavelet, thus solving the problem of selecting the optimal decomposition levels of wavelet transform when the original signal is unknown. Literature [6,7,8,9] takes energy and information entropy as evaluation indexes to determine the wavelet decomposition level, and uses the distribution characteristics of signals in different frequency

bands to estimate the effectiveness of the wavelet, essentially selecting the wavelet that is most similar to the signal of interest. However, the selection result of this method is easily affected by the noise distribution, and it is more suitable for signal diagnosis and recognition. When denoising deformation detection signals, literature [10] proposed that the wavelet decomposition level should be selected based on the minimum information criterion. Literature [11] and literature [12] used traditional information criteria such as AIC and BIC when selecting wavelet decomposition level. When analyzing large-level non-stationary data in civil and mechanical engineering applications, literature [13] proposes a new framework that comprehensively considers multiple indexes for selecting the most suitable wavelet base and decomposition level, and systematically applies existing evaluation indexes for selecting wavelet base and decomposition level. However, because of its systematicness, the process of this method is relatively complicated in actual operation, and it needs to calculate and analyze the signal in many aspects. Therefore, it is necessary to find a simple, reasonable and efficient method for the level selection of wavelet transform.

Most of the existing methods directly select some indicators for the selection of wavelet transform decomposition level, but this paper starts with the unknown "uncertainty" of the original signal and chooses to analyze this problem from the perspective of statistics. Firstly, the wavelet transform problem of the signal is modeled statistically, and the choice of optimal decomposition level is transformed into a model selection problem. Then, the Wavelet Selection Information Criterion (WSIC) is derived by reasonably balancing the goodness of fit and complexity of the model. Finally, it is verified by simulation experiments that WSIC criterion is more effective in selecting orthogonal wavelet transform models than AIC and BIC criteria used in literature [11]. The research in this paper provides the method and theory support for determining the optimal decomposition level of wavelet transform in practical application.

The rest of this paper is organized as follows. Some necessary preliminaries are introduced in Section 2. In Section 3, the orthogonal wavelet transform model selection criteria is introduced in detail. Simulation experiment is provided in Section 4 to verify the effectiveness of the proposed WSIC criterion for the selection of wavelet decomposition level. Finally, conclusions are drawn in Section 5.

II. PRELIMINARIES

2.1 Orthogonal Wavelet Transform Theory

The implementation of orthogonal wavelet transform is based on multi-resolution analysis (also known as multi-scale analysis). According to the finite precision multi-scale analysis and approximation [14], the signal $x(t)$ can be expressed as

$$x(t)=\sum_{k\in Z}c_{J,k}\phi_{J,k}(t)+\sum_{j=1}^{J}\sum_{k\in Z}d_{j,k}\psi_{j,k}(t) \tag{1}$$

where $\phi_{J,k}(t)$ and $\psi_{j,k}(t)$ are the functions obtained by the scale function $\phi(t)$ and the wavelet function $\psi(t)$ after translation and expansion transformation, respectively, and they are the basis functions of the scale space and the wavelet space under the corresponding scale.

The scale coefficient $c_{J,k}$ and the wavelet coefficient $d_{j,k}$ are the inner products of the signal and the scale basis function $\phi_{J,k}(t)$ and the wavelet basis function $\psi_{j,k}(t)$, respectively:

$$c_{J,k}=<x(t),\phi_{J,k}(t)> \tag{2}$$

$$d_{j,k}=<x(t),\psi_{j,k}(t)>$$

There is a step by step derivation relationship between the scale coefficient and the wavelet coefficient, and the calculation of $\{c_{j,k}\}_{j,k\in\mathbf{Z}}$ and $\{d_{j,k}\}_{j,k\in\mathbf{Z}}$ has the following transfer relationship for j:

$$c_{j,k}=\sum_{n\in Z}h(n-2k)c_{j-1,n} \tag{3}$$

$$d_{j,k}=\sum_{n\in Z}g(n-2k)c_{j-1,n} \tag{4}$$

where h and g are low-pass and high-pass filters of wavelet respectively. Equations (3) and (4) are the basis of Mallat algorithm. As can be seen from the two equations, as long as $\{h(n)\}_{n\in Z}$ and $\{g(n)\}_{n\in Z}$ are known, the scale coefficient and wavelet coefficient under each level j can be calculated by observing the $\{c_{0,n}\}_{n\in Z}$ obtained by the signal.

2.2 Statistical Model of Orthogonal Wavelet Transform

It is assumed that the observed signal $y(t)$ of length n consists of the original signal $f(t)$ and Gaussian white noise interference $\varepsilon(t)$:

$$y(t)=f(t)+\varepsilon(t),t=1,\cdots,n \tag{5}$$

where $\varepsilon(t)$ meets the conditions:

$$\varepsilon(t) \overset{i.i.d}{\sim} N(0,\sigma^2), t=1,\cdots,n$$

After the discrete wavelet transform, the signal can be expressed in the form of equation (1), assuming that the original signal is composed of the approximate signal obtained by the wavelet transform, that is,

$$f(t)=\sum_{k\in Z} c_{J,k}\phi_{J,k}(t)$$

According to the above assumptions, the statistical model of orthogonal wavelet transform can be given:

$$\begin{cases} y(t)=\sum_{k\in Z} c_{J,k}\phi_{J,k}(t)+\varepsilon(t), \\ \varepsilon(t) \overset{i.i.d}{\sim} N(0,\sigma^2), t=1,\cdots,n. \end{cases} \quad (6)$$

In the decomposition of level J, the signal $y(t) \sim N(\mu_J(t),\sigma^2)$, where

$$\mu_J(t)=E\big(y(t)\big)=E\left(\sum_{k\in Z} c_{J,k}\phi_{J,k}(t)+\varepsilon(t)\right)=\sum_{k\in Z} c_{J,k}\phi_{J,k}(t)$$

So $y(t) \sim N(\sum_{k\in Z} c_{J,k}\phi_{J,k}(t),\sigma^2)$. The density function of this distribution is

$$p(y\,|\,c_{J,k},\sigma^2)=\frac{1}{\sqrt{2\pi}\sigma}\exp\left\{-\frac{1}{2\sigma^2}\Big(y-\sum_{k\in Z} c_{J,k}\phi_{J,k}(t)\Big)^2\right\} \quad (7)$$

2.3 Monotone Property

The relevant properties of the orthogonal wavelet transform statistical model will be discussed in the following, which will serve as the basis for subsequent research.

Property 1 *The number of scale function $\phi_{J,k}(t)$ of the model in J level is $q(J)$, and for $\forall J_1 < J_2$, there is $q(J_1) > q(J_2)$.*

Proof According to the uniform monotonicity of the closed subspace $\{V_j\}_{j\in \mathbf{Z}}$ in multi-resolution analysis, the scale space decreases with the increase of the decomposition level, and the number of basic functions of the scale space decreases with the decrease of the scale space. Because of the frequency domain decomposition of the signal, the sampling rate of each level is halved, and the length of the new sequence is reduced by half. Therefore, the number of scale function $q(J)$ decreases with the increase of decomposition level J.

Property 2 *The variance of the residual of the model on the J level is $\hat{\sigma}^2(J)$, and for $\forall J_1 < J_2$, there is $\hat{\sigma}^2(J_1) < \hat{\sigma}^2(J_2)$.*

Proof According to equation (1), $\varepsilon(t)$ can be composed of a linear combination of wavelet functions, i.e.

$$\hat{\varepsilon}(t)=\sum_{j=1}^{J}\sum_{k\in Z} d_{j,k}\psi_{j,k}(t)=\sum_{j=1}^{J}\hat{\varepsilon}_j(t)$$

Since the wavelet function $\psi(t)$ is zero mean, let $\hat{\varepsilon}_j(t) \sim N(0,\hat{\sigma}_j^2)$, according to the mutually orthogonal property of the wavelet space at different levels, $\hat{\varepsilon}_j(t)$ can be independent of each other. From the additivity of the normal distribution, we know that

$$\hat{\varepsilon}(t)=\sum_{j=1}^{J}\hat{\varepsilon}_j(t) \sim N(0,\hat{\sigma}^2(J))$$

where $\hat{\sigma}^2(J)=\sum_{j=1}^{J}\hat{\sigma}_j^2$. It can be seen that the variance of model residuals increases with the increase of decomposition level.

III. ORTHOGONAL WAVELET TRANSFORM MODEL SELECTION CRITERIA

According to the principle of orthogonal wavelet transform, the trend information of the signal is mainly located in the scale space, and the detail information is mainly located in the wavelet space. If the scale space that completely contains the observation signal $y(t)$ is $\phi_{0,k}(t)$, that is, the space of scale 0, then the orthogonal wavelet transformation process of the signal is to decompose the space $\phi_{0,k}(t)$ again and again, and decompose the useful information such as the trend of the signal into the scale space, and decompose the interference information such as noise into the wavelet space. To determine the scale of wavelet decomposition is to determine the number of decomposition levels, so that the best decomposition effect can be achieved under the number of decomposition levels.

3.1 Measure of Model Goodness of Fit

Since the likelihood function is the most sensitive criterion for model parameters to deviate from the true value [15], the probability density function of the real model is $g(y)$, and it can be seen from equation (7) that the probability density function of the candidate submodel is $p(y\,|\,c_{J,k},\sigma^2)$. Suppose the parameter vector $\theta=(c_{J,k},\sigma^2)$, and consider the independent observed signal sequence $y_1, y_2, ..., y_n$ of length n, then the mean logarithmic likelihood is

$$\frac{1}{n}\sum_{i=1}^{n}\ln p(y_i \mid \theta)$$

According to the strong law of numbers, we get

$$\frac{1}{n}\sum_{i=1}^{n}\ln p(y_i \mid \theta) \xrightarrow{a.s.} \int g(y)\ln p(y \mid \theta)dy = S(g; p(y \mid \theta)) \quad (8)$$

assuming that the integral exists.

The Kullback-Leibler (KL) distance is a measure of the degree of difference between two probability distributions. If the density function of the candidate model is $p(\cdot \mid \theta)$ and the density function of the real model is g, then the KL distance between the distribution of the real model and the distribution of the candidate model is defined as [16]

$$\mathrm{KL}(g, p(\cdot \mid \theta)) = \int g(y)\ln\frac{g(y)}{p(y \mid \theta)}dy \quad (9)$$

By observing equations (8) and (9), it can be found that there is the following relationship between mean logarithmic likelihood and KL distance

$$\mathrm{KL}(g, p(\cdot \mid \theta)) = S(g; g) - S(g; p(\cdot \mid \theta)) \quad (10)$$

The KL distance represented by equation (10) is always greater than or equal to 0, and the KL distance is equal to 0 if and only if $g(y) = p(y \mid \theta)$. This shows that $S(g; p(\cdot \mid \theta))$ is a reasonable measure of the goodness of fit of a model, and by maximizing $S(g; p(\cdot \mid \theta))$, or minimizing $-S(g; p(\cdot \mid \theta)$, candidate submodels that are closest to the real model can be found. If the maximum likelihood estimator of θ is θ_0, then θ_0 is the parameter that minimizes the KL distance.

3.2 Deviation Correction

In the model selection problem, there are usually multiple candidate submodels, that is, there are multiple $p(y \mid \theta)$, and the parameter vector θ of different submodels is different. At this time, the maximum likelihood principle cannot provide a useful solution for this kind of problem, and a solution can be obtained by combining the basic idea of statistics with the maximum likelihood principle.

Let's consider the case where KL is equal to 0, which is $g(y) = p(y \mid \theta_0)$. $\mathrm{KL}(g, p(\cdot \mid \theta))$ and $S(g; p(\cdot \mid \theta))$ are respectively $\mathrm{KL}(\theta_0, \theta)$ and $S(\theta_0; \theta)$, and when θ is close enough to θ_0, $\mathrm{KL}(\theta_0, \theta)$ is approximately

$$\mathrm{KL}(\theta_0; \theta_0 + \triangle\theta) = \frac{1}{2}\|\triangle\theta\|_{J^2}$$

where $\|\triangle\theta\|_{J^2} = \triangle\theta' J \triangle\theta$, J is the Fisher information matrix, which is positive definite and defined as

$$J_{ij} = E\left\{\frac{\partial^2 \ln p(y \mid \theta)}{\partial\theta_i \partial\theta_j}\right\}$$

where J_{ij} represents the (i,j)th element of J, θ_i and θ_j are the ith and jth elements of θ, respectively. Thus, when θ is very close to the maximum likelihood estimator θ_0, the change of the distribution defined by $p(y \mid \theta)$ with the true distribution $p(y \mid \theta_0)$ over $S(\theta_0; \theta)$ can be measured by $\frac{1}{2}\|\theta - \theta_0\|_{J^2}$. Consider the case where the variation of θ that maximizes the likelihood function is confined to a low-dimensional subspace Θ that does not contain θ_0. For the maximum likelihood estimator $\hat{\theta}$ of θ_0 limited to in Θ, if the maximum $S(\theta_0; \theta)$ of θ is close enough to θ_0, then for a sufficiently large n, the distribution of $n\|\hat{\theta} - \theta\|_{J^2}$ is approximately the Chi-square distribution of degrees of freedom equal to the dimension of the restricted parameter space under certain regularity conditions [15]. So we have

$$E(X) 2n\mathrm{KL}(\theta_0; \hat{\theta}) = n\|\theta - \theta_0\|_{J^2} + k \quad (11)$$

where the distribution of the variable X is the same as the approximate distribution of $n\|\hat{\theta} - \theta\|_{J^2}$, and k is the dimension of the space Θ or the number of parameters independently adjusted to maximize the likelihood function. Equation (11) describes the prediction error based on statistical data.

When there are multiple candidate submodels, it is natural to choose the model that minimizes the $E\mathrm{KL}(\theta_0; \hat{\theta})$. Therefore, it is necessary to consider estimating $n\|\theta - \theta_0\|_{J^2}$ in equation (11). The asymptotic distribution of $\sqrt{n}(\hat{\theta} - \theta)$ is approximately a normal distribution with a mean of 0 and a variance matrix of J^{-1}. If

$$2\left(\sum_{i=1}^{n}\ln p(y_i \mid \theta_0) - \sum_{i=1}^{n}\ln p(y_i \mid \hat{\theta})\right) \quad (12)$$

is used as an estimate of $n\|\theta - \theta_0\|_{J^2}$, then the downward bias introduced by replacing θ with $\hat{\theta}$ needs to be corrected. This can be done by adding k to equation (12). When selecting the model, it is only necessary to compare the $E\mathrm{KL}(\theta_0; \hat{\theta})$ estimates of different candidate submodels.

Since the public items do not affect the comparison, the public items containing θ_0 can be discarded.

3.3 Model Parameter Estimation

For parameter vector $\theta = (c_{J,k}, \sigma^2)$, the estimator of $c_{J,k}(k \in Z)$ can be obtained as

$$\hat{c}_{J,k} =< y(t), \phi_{J,k}(t) >, (k \in Z)$$

according to equation (2).

The maximum likelihood estimator of σ^2 can be obtained by calculation as

$$\hat{\sigma}^2 = \frac{1}{n}\sum_{t=1}^{n}\left(y(t) - \sum_{k\in Z}\hat{c}_{J,k}\phi_{J,k}(t)\right)^2 \quad (13)$$

Using equation (13), it can be obtained that the maximum value of log-likelihood function $\ln L\left(y; c_{J,k}, \sigma^2\right)$ is

$$\ln L\left(y; c_{J,k}, \sigma^2\right) = -\frac{n}{2}\ln(2\pi) - \frac{n}{2}\ln\hat{\sigma}^2 - \frac{n}{2} \quad (14)$$

3.4 Determination of Model Selection Criteria

In order to calculate the estimates of $E\mathrm{KL}(\theta_0; \hat{\theta})$ for different candidate submodels, equation (14) is brought into equation (12), and the deviation correction term k is introduced, where k can be regarded as the dimension of scale space. According to property 1 of the orthogonal wavelet transform model, the number of scale function $\phi_{J,k}(t)$ on the J-level is $q(J)$, then the dimension of the scale space is also $q(J)$. Then discard the common term and the irrelevant constant term, and finally get the orthogonal wavelet transformation model selection criterion is

$$n\ln\hat{\sigma}^2 + 2q \quad (15)$$

where n is the signal length, according to the property 2 of the orthogonal wavelet transform model , $\hat{\sigma}^2$ is the variance of the cumulant of all detail noise signals obtained after J decomposition, and q is the dimension of the scale space under the level J, that is, the number of scale functions or the number of scale coefficients.

By observing equation (15), it can be found that this criterion is very similar to AIC criterion used in literature [11] in form, but the meanings expressed by variables are different. In order to distinguish, the criterion represented by equation (15) given in this paper is named the wavelet selection information criterion (WSIC).

According to the property of orthogonal wavelet transform model, q decreases with the increase of decomposition level, and $\hat{\sigma}^2$ increases with the increase of decomposition level, so a suitable J can always be found to make WSIC reach the minimum value, and the J satisfying this condition is the optimal decomposition level of the corresponding wavelet.

IV. SIMULATION EXPERIMENT

4.1 Experimental Setup

In order to verify the effectiveness of the WSIC criterion for the selection of wavelet decomposition level given in this paper, WSIC criterion, AIC criterion and BIC criterion are used to process the same data respectively, and the effects of different criteria for the selection of wavelet decomposition level are compared. In order to avoid the useful high-frequency detail signal as noise removal, stein unbiased risk estimation is selected to determine the threshold and soft threshold function is used to process the coefficient. The simulation experiment steps are as follows:

Step 1: Selecting a wavelet and generating the original signal $f(t)$ using the scale function of the wavelet obtained by 7 iterations.

Step 2: Adding Gaussian white noise interference $\varepsilon(t)$ to $f(t)$, to obtain a noise signal with a specific SNR.

Step 3: Decomposing the signal to the largest level with the selected wavelet and store the detail coefficients of each level.

Step 4: Calculating the stein unbiased risk estimation threshold for each level of detail coefficients.

Step 5: Processing the detail coefficients of each level by using the soft threshold function.

Step 6: Reconstructing the signal with the coefficient after threshold processing, to obtain the estimated signal.

Step 7: Calculating the values of WSIC, AIC and BIC under each level respectively, and selecting the level corresponding to the minimum value of each index as the optimal level under the index.

Step 8: Increasing the signal-to-noise ratio from -5dB to 35dB with an interval of 5dB. Repeating Step 2-Step 7 1000 times for each signal-to-noise ratio, and recording the results of each experiment.

4.2 Analysis of Experimental Results

In order to avoid the chance of the experiment, db6, sym7 and coif2 wavelets-three different types and representative of the experiment were selected at the same time. Among them, the signal length generated by db6 and coif2 wavelet is 1409, and the signal length generated by

sym7 wavelet is 1665. The above simulation experiments were carried out by matlab, and the level selected by each criterion and the number of experiments selected for this level were recorded. The frequency obtained by dividing the number of experiments of this level by the total number of experiments is taken as the probability of selecting this level. The level with the greatest probability is chosen as the optimal level of the criterion. The probability corresponding to the optimal level is denoted as the level accuracy, and the higher the value, the greater the probability that the selected level is the optimal level. The optimal level and the accuracy of level were compared between WSIC criterion, AIC criterion and BIC criterion. The experimental results are shown in TABLE 1 - TABLE 3.

Table.1: The selection level and corresponding probability of the three criteria under different SNR (db6 wavelet)

SNR/dB	-5	0	5	10	15	20	25	30	35
WSIC	**84.9%** (7)	**67.6%** (6)	**98.8%** (6)	**92.9%** (6)	53.6% (6)	**98.1%** (5)	**62.8%** (4)	99.9% (4)	**99.8%** (4)
	15.1% (6)	32.3% (7)	1.2% (5)	7.1% (5)	45.9% (5)	1.9% (4)	37.2% (5)	0.1% (3)	0.2% (3)
	/	0.1% (5)	/	/	0.5% (4)	/	/	/	/
AIC	**78.6%** (7)	**56.4%** (6)	**94.5%** (6)	**90.6%** (6)	63% (6)	**88.4%** (5)	**51.4%** (4)	99.9% (4)	**99.6%** (4)
	21.3% (6)	42.9% (7)	3.2% (5)	9.4% (5)	37% (5)	7.9% (6)	48.6% (5)	0.1% (3)	0.4% (3)
	0.1% (5)	0.7% (5)	2.3% (7)	/	/	3.7% (4)	/	/	/
BIC	**78.5%** (7)	**56.7%** (6)	**94.6%** (6)	**90.2%** (6)	62.7% (6)	**88.5%** (5)	**51.7%** (4)	99.9% (4)	**99.6%** (4)
	21.4% (6)	42.5% (7)	3.2% (5)	9.8% (5)	37.3% (5)	7.6% (6)	48.3% (5)	0.1% (3)	0.4% (3)
	0.1% (5)	0.8% (5)	2.2% (7)	/	/	3.9% (4)	/	/	/

Table.2: The selection level and corresponding probability of the three criteria under different SNR (sym7 wavelet)

SNR/dB	-5	0	5	10	15	20	25	30	35
WSIC	**79.8%** (7)	**80.8%** (6)	**99.3%** (6)	**97.3%** (6)	71% (6)	**98.4%** (5)	**90.3%** (5)	**98.3%** (4)	100% (4)
	20.2% (6)	18.8% (7)	0.7% (5)	2.7% (5)	29% (5)	1.5% (6)	9.7% (4)	1.7% (5)	/
	/	0.4% (5)	/	/	/	0.1% (4)	/	/	/
AIC	**71%** (7)	**75.7%** (6)	**96.6%** (6)	**93.3%** (6)	72.9% (6)	**89.5%** (5)	**88.7%** (5)	**92%** (4)	100% (4)
	29% (6)	23.5% (7)	3.3% (5)	6.7% (5)	27.1% (5)	10.3% (6)	11.3% (4)	8% (5)	/
	/	0.8%	0.1%	/	/	0.2%	/	/	/

		(5)	(7)			(4)			
BIC	**70.8%**	**76.1%**	**96.6%**	**93%**	72.3%	**89.6%**	**88.4%**	**92.1%**	100%
	(7)	(6)	(6)	(6)	(6)	(5)	(5)	(4)	(4)
	29.2%	23.1%	3.3%	7%	27.7%	10.2%	11.6%	7.9%	/
	(6)	(7)	(5)	(5)	(5)	(6)	(4)	(5)	
	/	0.8%	0.1%	/	/	0.2%	/	/	/
		(5)	(7)			(4)			

Table.3: The selection level and corresponding probability of the three criteria under different SNR (coif2 wavelet)

SNR/dB	-5	0	5	10	15	20	25	30	35
WSIC	**83.1%**	**68.2%**	**92%**	53.9%	**74.4%**	**99.6%**	97.2%	**93.6%**	100%
	(7)	(6)	(6)	(5)	(5)	(4)	(4)	(3)	(3)
	16.2%	30.3%	7.6%	45.8%	25.4%	0.3%	2.8%	6.4%	/
	(6)	(7)	(5)	(6)	(4)	(5)	(3)	(4)	
	0.7%	1.5%	0.3%	0.3%	0.2%	0.1%	/	/	/
	(5)	(5)	(7)	(4)	(6)	(3)			
	/	/	0.1%	/	/	/	/	/	/
			(4)						
AIC	**75.7%**	**57.3%**	**85.9%**	71.3%	**67.5%**	**94.7%**	97.9%	**78.5%**	100%
	(7)	(6)	(6)	(6)	(5)	(4)	(4)	(3)	(3)
	24.2%	40.7%	10.6%	28.6%	17.5%	5.2%	2.1%	21.5%	/
	(6)	(7)	(5)	(5)	(4)	(5)	(3)	(4)	
	0.1%	2%	3.5%	0.1%	15%	0.1%	/	/	/
	(5)	(5)	(7)	(4)	(6)	(3)			
BIC	**75.7%**	**57.4%**	**85.8%**	70.7%	**67.7%**	**94.8%**	97.9%	**79.3%**	100%
	(7)	(6)	(6)	(6)	(5)	(4)	(4)	(3)	(3)
	24.2%	40.6%	10.8%	29.2%	17.8%	5.1%	2.1%	20.7%	/
	(6)	(7)	(5)	(5)	(4)	(5)	(3)	(4)	
	0.1%	2%	3.4%	0.1%	14.5%	0.1%	/	/	/
	(5)	(5)	(7)	(4)	(6)	(3)			

In TABLE 1 to TABLE 3, the first line of each criterion is the optimal level and level accuracy selected by the criterion. TABLE 1 is taken as an example for analysis. The first column of data shows that the signal generated by db6 wavelet is interfered with by Gaussian white noise to obtain a noisy signal with a signal-to-noise ratio of -5dB. WSIC, AIC and BIC criteria are used to select the optimal decomposition level of the signal, and the optimal decomposition level selected by the three criteria is 7. However, the accuracy of WSIC, AIC and BIC criteria were 84.9%, 78.6% and 78.5%, respectively. It can be found that the level accuracy of WSIC criteria is higher than that of AIC and BIC criteria. Similarly, the level accuracy of the three criteria under other SNR and the experimental situation of other wavelet can be compared.

It can be seen from the results that the optimal level selected by WSIC criteria is basically the same as that selected by AIC and BIC criteria, but the level accuracy of WSIC criteria is greater than that of AIC and BIC criteria under most SNR conditions. The level accuracy of WSIC criterion is up to 15.1% higher than that of AIC criterion and up to 14.3% higher than that of BIC criterion. This

shows that WSIC criterion has higher stability than AIC and BIC criterion when selecting the optimal level.

V. CONCLUSION

The choice of wavelet transform decomposition level is the key to the effect of wavelet noise reduction. In the case that the original signal is unknown, this paper looks at the problem of wavelet level selection from the perspective of model selection from a statistical point of view, gives the WSIC criterion, and compares the application effect of WSIC criterion with AIC and BIC criteria through simulation experiments. The simulation results show that the level accuracy of WSIC criterion is up to 15.1% higher than that of AIC criterion and up to 14.3% higher than that of BIC criterion. The results show that WSIC criterion is more stable than AIC and BIC criterion in the selection of orthogonal wavelet transform model. It shows that WSIC criterion has higher level accuracy when the optimal level selected by the three criteria is the same. This criterion can reasonably balance the goodness of fit and the complexity of the model in the process of wavelet transformation, and can more accurately select the optimal decomposition level under different signal-to-noise ratio, so that the wavelet noise reduction can achieve better results. The research in this paper provides the method and theory support for determining the optimal decomposition level of wavelet transform in practical application. Further study can apply the WSIC criterion in this paper to practical problems.

REFERENCES

[1] Zhu, J. J., Zhang, Z. T., Kuang, C. L., & Pan, J.B. (2015). A reliable evaluation indicator of wavelet de-noising. *Geomatics and Information Science of Wuhan University*, 40(5), 688-694. doi: 10.13203/j. whugis20130417

[2] Rouis, M., Ouafi, A., & Sbaa, S. (2019). Optimal level and order detection in wavelet decomposition for PCG signal denoising. *Biomedical Engineering/ Biomedizinische Technik*, 64(2),163-176. doi: 10.1515/bmt-2018-0001

[3] Gao, Y. D., Wang, H. L., You, S. H., Feng, L., He, Y. Y., & Liu, K. (2020). A pulsar signal denoising algorithm based on wavelet basis function selection and improved threshold function. *Electronics Optics & Control*, 27(4),15-19. doi:10.3969/j.issn.1671-637X.2020.04.004

[4] Jang, Y. I., Sim, J. Y., Yang, J. -R., & Kwon, N. K. (2021). The optimal selection of mother wavelet function and decomposition level for denoising of DCG signal. *Sensors*, 21(5), 1851. doi: 10.3390/s21051851

[5] Zheng, Y., Chen, X. H., & Zhu, R. (2019). Research on improved optimal wavelet base selection method and frequency hopping signal detection. *Fire Control & Command Control*, 44(5), 102-106. doi: 10.3969/j.issn.1002-0640.2019.05.022

[6] Yan, R., & Gao, R. X. (2009). Base wavelet selection for bearing vibration signal analysis. *International Journal of Wavelets, Multiresolution and Information Processing*, 7(04), 411-426. doi: 10.1142/S0219691309002994

[7] Hafiz, F., Swain, A., Naik, C., Abecrombie, S., & Eaton, A. (2019). Identification of power quality events: selection of optimum base wavelet and machine learning algorithm. *IET Science, Measurement & Technology*, 13(2), 260-271. doi: 10.1049/iet-smt.2018.5044

[8] Kaplun, D., Voznesenskiy, A., Romanov, S., Nepomuceno, E., & Butusov, D. (2019). Optimal estimation of wavelet decomposition level for a matching pursuit algorithm. *Entropy*, 21(9), 843. doi: 10.3390/e21090843

[9] Freire, P. K. M. M., & Santos, C. A. G. (2020). Optimal level of wavelet decomposition for daily inflow forecasting. *Earth Science Informatics*, 13, 1163-1173. doi: 10.1007/s12145-020-00496-z

[10] Zhao, Q., & Huang, S. X. (2009). Determination of deformation-monitoring precision using wavelet transformation based on AIC criterions. *Journal of Geomatics*, 34(5), 46-47. doi: 10.14188/j.2095-6045.2009.05.012

[11] Xiang, D., & Gong, J. B. (2014). To determine the quantitative index for the optimal decomposition scale in wavelet de-noising of deformation series. *Geomatics and Information Science of Wuhan University*, 39(4), 467-470. doi: 10.13203/j. whugis20120216

[12] Zhao, F. Z. (2018). Wavelet denoising quality evaluation method and its application in deformation monitoring. *Shandong University of Science and Technology*. Shandong.

[13] Silik, A., Noori, M., Altabey, W. A., Dang, J., Ghiasi, R., Wu, Z. (2022). Optimum wavelet selection for nonparametric analysis toward structural health monitoring for processing big data from sensor network: A comparative study. *Structural Health Monitoring*, 21(3), 803-825. doi: 10.1177/14759217211010261

[14] Wang, H. Q. (2011). Wavelet Analysis and Application. *Beijing University of Posts and Telecommunications Press*, Beijing.

[15] Akaike, H. (1974). A new look at the statistical model identification. *IEEE Transactions on Automatic Control*, 19(6), 716-723.

[16] Claeskens, G., & Hjort, N. L. (2008). Model selection and model averaging. *Cambridge University Press*, Cambridge.

International Journal of Advanced Engineering Research and Science (IJAERS)
Peer-Reviewed Journal
ISSN: 2349-6495(P) | 2456-1908(O)
Vol-11, Issue-11; Nov, 2024
Journal Home Page Available: https://ijaers.com/
Article DOI: https://dx.doi.org/10.22161/ijaers.1111.7

Creativity process is Charge Neutralization Process

Pavle Vesić

Belgrade, Serbia

Received: 16 Oct 2024,

Receive in revised form: 15 Nov 2024,

Accepted: 21 Nov 2024,

Available online: 30 Nov 2024

Keywords*— *CNP, electron, proton, neutron, rna, dna, neuron.

***Abstract*—** *Charge Neutralization Process (CNP) unifies all forces in nature, creates matter and life and constantly keeps the whole universe in an equilibrium state. Electron and proton are elementary particles which estimated decay time is 65 billion years, what is the other name for eternity. This article argues that univese is governed by uniqe process - Charge Neutralization Process – CNP. CNP constantly acts through whole universe, forcing elementary particles (electrons and protons), to form and sustain elecrically neutral material products, listed in Periodic Table of Elements.*

After Hydrogen formation, two or more **electron- proton pairs** were forced to establish electricaly neutral structures (matter creation). That was not possible without additional particle-like energy constructs. CNP created nutron(s)-**temporary particles**, which were added to the nucleus structure in order to establish neutral products.

CNP unifies all forces, acting on the every level of dimension and complexity : atomic, molecular, cellular, planetar, galaxy,... creating neutrons, RNA, neurons, neuron bundles (brain), our planet core, and so on.

Elementary particles Electron has toroidal structure (2, 5) consisting of $\lambda_e/\lambda_x = 19206$ electric energy ($E = hf$) rings ($E = \hbar\omega$) - photons (λ_e is electron gravitational mass wavelength, λ_x is Duane-Hunt wavelength). Proton has the same structure as electron , but different mass, $m_p = 1836\, m_e$, consequently; 1836 time more rings (photons).

Electron model is shown on Fig. 1

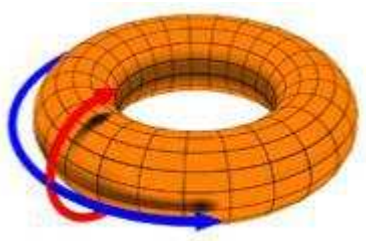

Fig. 1

Under the specific condition, similar to Big bang description, electron - proton pairs, formed hydrogen atoms.

In normal living condition thery last essentially forever. Electron (and proton) fine structure is established from two (electric and magnetic) traped and locked vortexes in resonant state (5). In hydrogen atom, electron-proton **energy circulates on such way that overall atomic charge is always neutral.** As charge is directly dipendent on vortex energy path (space energy distribution) it is obvious that hydrogen neutrality is mantained by adjustement of proton energy circulation path.

How electron - proton charge can be neutralised?

Electron and proton fine structure dictates what must happen to establish lasting charge neutral product. Proton energy circulation lenght is 1836 times longer than electron, what suggest that proton energy circulation lenght has to be adjusted („diminished“) to the electron energy circulating lenght. That is why proton is forced to the center of electron and that is criteria how nucleus and atom radius are determined.

If hydrogen atom is exposed to some source of neutrality disturbing energy (that energy will be sensed by electron thanks to the its position), which can not be compensated by proton circulation path adjustement, CNP will generate additional energy construct – **neutron**, which is sum of

electron and proton energy, concatenated in unique entity, placed in nucleus, forming deuterium, hydrogen isotope. Neutron function is to add/subtract needed amount of energy (charge) to sustain overall atom neutrality. If disturbing energy continues to violate established deuterium neutrality, CNP will add another neutron, forming tritium.

Free neutrons decay in 885 ± 15 s (1)

Neutron decay refers to the process where a free neutron outside the nucleus brakes down into **a proton, an electron, and an antineutrino**. This decay occurs due to the neutron's instability and has a very short lifetime.

We are also considering the neutron decaying to two or more particles, at least one of which is a new (dark) particle, from outside of the Standard Model, hence the name **neutron dark decay.**

If disturbing energy has pulse shape of high energy level, CNP will move hydrogen electron from ground level to the first uper energy level. Radius of uper electron energy circulation level is grater than graund radius, in order to diminish influence of incoming disturbing energy which is manifested as electron charge fluctuation. When such disturbance vanishes, electron will fall down on previous energy level, emitting amount of energy (photons) which caused change of his orbital position (energy conservation).

Matter

From the PTE we see that atomic numbers increase steady , one by one (from 1 to 118). How we can decipher neutron number within matter atom?

Number of neutrons is determined by CNP, based on atom **electron configuration**. When we look at the matter atom(s) we „see" electrons only, as protons and neutrons are deep inside (hydrogen electron and nucleus radius ratio is 10^5). For arbitrary number of electron - proton pairs, CNP will **create as many neutrons as needed** and add it to nucleus, resulting in atom neutrality (for example, Mercury atomic number is 80, but has 120 neutrons). Matter atoms, once created as neutral, are the subject if intensive CNP surveillance. Existing matter in whole universe is **simultaneosly** cheched and maintained in neutral state with **Compton frequency rate** (7.81×10^{20} Hz) !!! In case that incoming energy violates atom neutrality, making an impact on valence electrons, CNP will make reaction by adjusting neutron(s) – proton(s) circulation path(s) within nucleus, mantaining once established charge neutrality.

All matter products, (atoms, molecules, compaunds, lifecells, planets, stars, galaxies, universe) are the subject of CNP.

Earth's magnetic reversal is dictated by CNP.

Life

Single cell organisms are made of materia. All of them have the same principall structure : membrane, internal liquid and nucleus. F**unction of cell's nucleus is the same as function of nucleus in atom**: it contains such matter products whose function is to establish neutrality of its own cell membrane, which is exposed to the outher world. When cell is the subject of incoming energy, which we can value as disturbing (we refer to matter description above), membrane valence electrons will change their charge, and it will be compensated (neutralisated) by nucleus reaction (modification of neutron- proton energy circulation path in case of atom) , creating pre-RNA structure. Pre-RNA is made by CNP, principally in the same manner as neutrons, with the same purpose: to establish and mantain charge neutrality of membrane. In this case CNP acts on higher level of complexity.

When the disturbing energy stops (one example is sunlight energy during night) , existing pre-RNA becomes INTERNAL source of membrane valence electrons disturbance. CNP solution is : internal pre-RNA will be neutralised by conjugate bases **(A-T, C-G), thus creating pre-DNA.**

In process of evolution, at some point in time, pre-RNA, turned to the RNA and consequently to DNA structures.

Multicellular organisms are subject of CNP as well, on the higher level of complexity.

Sperm cells are electrically negative while egg cell is positively charged. They are subject to the CNP, on the very same principle as electron and proton during the hydrogen formation. Fusion of egg and sperm (fertilisation) is in fact CNP (crossover), resulting in neutral cell – zygote. When zygote reach threshold energy level it will undergo to division phase. CNP function is to ADD corresponding bases to RNA, forming DNA, where, as collaterall gain, we get reproduction.

In the case of homo sapiens, skin is membrane which divide body from external environment. Through evolution process, CNP created stabilisation vehicle : **neuron.** Brain function is equivalent to atom and cell nucleus function : establishing and maitaining membrane neutrality. That neutrality is realised by neuron's function.

Brain

Brain is memory made of neurons. All body neurons end up in brain. During the evolution process, neurons were organised according to assigned function (visual cortex for example). **Brain does not posses any processing ability**. Brain function is to store electric image generated **externally (our senses) and internally under free will (our desire).** Brain **electric image** is the source of

neurosignals which function is to establish charge neutrality of violated valence electons. Brain activity is under CNP's permanent dinamic control and influence.

Senses

Our senses emerged as CNP collateral gain. Let's take sense of sight. At the RNA time of life emergence, some of the outher membrane cells were more light sensitive, compared to others. That group of cells were modified by CNP as the consequences of higher light sensitivity. During replication, this modifications are transferred and improved from generation to generation (evolution) so some sort of pre-eye organs appeared.

How did nature decide to create sense of sight as we have it today?

There was not any knowledge regarding the structure and construction of visual cortex. DNA (RNA) was not the source of that knowledge. DNA was built from RNA in neutralisation process (CNP) as up to dated history of all sorts of cell's membrane valence electrons violated energy inputs. DNA role in heredity process is clear, simple and unavoidable. The final goal, in sense of sight creation, was, to built such mechanism which was able to sucesfully neutralise all eye's valence electrons, which are parts of rods and cones, when light enters the eye. Light has wide freqency spectar, each and every of them carries specific amount of energy ($E= h f$), which change valence electron charge, and, as a consequence, their neutality is violated. In order to response to **all** neutrality violation, CNP produced (evolution is time scale) universal frequency response mechanism- visual cortex which is connected by optic nerve with the eye.

What is the function of visual cortex?

Visual cortex generates electric signals as a respons to incoming frequencies which, as we know, causes eyes valence electrons charge to change. Respons signal's frequency MUST be equal to the input frequencies in order to cancel **that** electron charge change. That is the reason why we see red as red (David Chalmers, consciousness hard problem). So, our sense of sight is collateral gain of CNP. Our brain does not CONTROL sense of sight, as source of CNP is out of our body and mind. We can close our eyes, but we can not change the the content of incoming light energy.

The same mechanism explains all other senses.

Movement

In order to change our position we have to move. Who issues the order to our muscles how to move and when to stop? Every part of our body has many nerves which are neurons of different length and construction. Neurons, as we already explained, have the same function as neutrons in atoms.

Brain is the place where all neurons migrate. Under the control of our mind, in certain part of brain we generate request for movement (free will). That request is electric image of the complete motion path (where we want to move end how we want to get there). That internally created electric image causes violation of dedicated valence electrons in our body, which will be forced to change their physical position what, as a finall result, will cause cancelation of internally created image.

Recapitulation

The only long living particles in the universe are electrons and protons. In fact, they are eternal in normal living condition (temperature, pressure,...). If they are exposed to the high energy environment, like in CERN, they will be broken into indefinite energy chunks, various group of photons.

How electron and proton can manifest their charge, in fact, forever? Is the perpetuum mobile right explanation? Hydrogen atom can not be simulated on any digital computer, not only becouse of low processing power, but due to Turing halt problem, which Kurt Gedel, with his incompleteness theorem , definitely marked as unsolvable.

Will quantum mechanic help us?

It seams that it can. The immediate solution seems to be quantum computer. It performs **ALL instructions simultaneosly**. Seth Lloyd , MIT, describes quantum computer design as hacking the universe. On the question „ Is the universe in fact giant quantum computer „ Seth answer was „ It could be „.

Let's go hundred years back in time. It was proved that light travels forever , without any attenuation. What kind of material (ingredient) is empty space ? It is some sort of superconductor?

Physic nobel prize winner for 2004. Frank Wilczek, in his book Lightnes of Being , describing empty space wrote that it is: " The primery ingredient of physical reality, from which all else is formed, fills space and time. Every fragment, each space time element, has the same basic properties as every other element . The primary ingrediant of reality is allive with quantum activity. Quantum activity has special characteristics. It is spontaneous and unpredictable. And to observe quantum activity, you must disturbe it. The primary ingrediant of reality also contains enduring material components. This make the cosmos a multilayered, multicolored superconductor. The primery ingrediant of reality contains a metric field that gives space-time rigidity and causes gravity. The primery ingrediant of reality weighs, with universal density".

CONCLUSION

Universe is ether based , single instruction quantum computer .

That instruction is Charge Neutralization Process – CNP .

Universe has not Turing halt problem.

Universe ends processing when neutralization is complete .

REFERENCES

[1] S. Doe, "Neutron Dark Decay" *arXiv*, vol. 2306.11349, Jun. 2023. [Online]. Available: https://arxiv.org/pdf/2306.11349.

[2] Consa, O. (2014). Helical model of the electron. *The General Science Journal*, 1.

[3] Zakaria, H., Kamarudin, D., Fauzi, M. A., & Wider, W. (2023, March). Mapping the helix model of innovation influence on education: A bibliometric review. In *Frontiers in Education* (Vol. 8, p. 1142502). Frontiers Media SA.

[4] Câmara, A. S., Kubalová, I., & Schubert, V. (2024). Helical chromonema coiling is conserved in eukaryotes. *The Plant Journal*, *118*(5), 1284-1300.

[5] Gryziecki, G. (2023). The Toroidal Fine-Structure of the Electron (Republished from GJSFR). *Journal of Aetherometric Research*, *3*(4), 1-8.

[6] Stávek, J. Spin interpreted as the angular momentum curvature, electron g-factor interpreted as the ratio of toroidal torsion and curvature, unlocking of the fixed Planck constant h–new tests for old physics. *European Journal of Applied Physics*, *3*, 61-66.

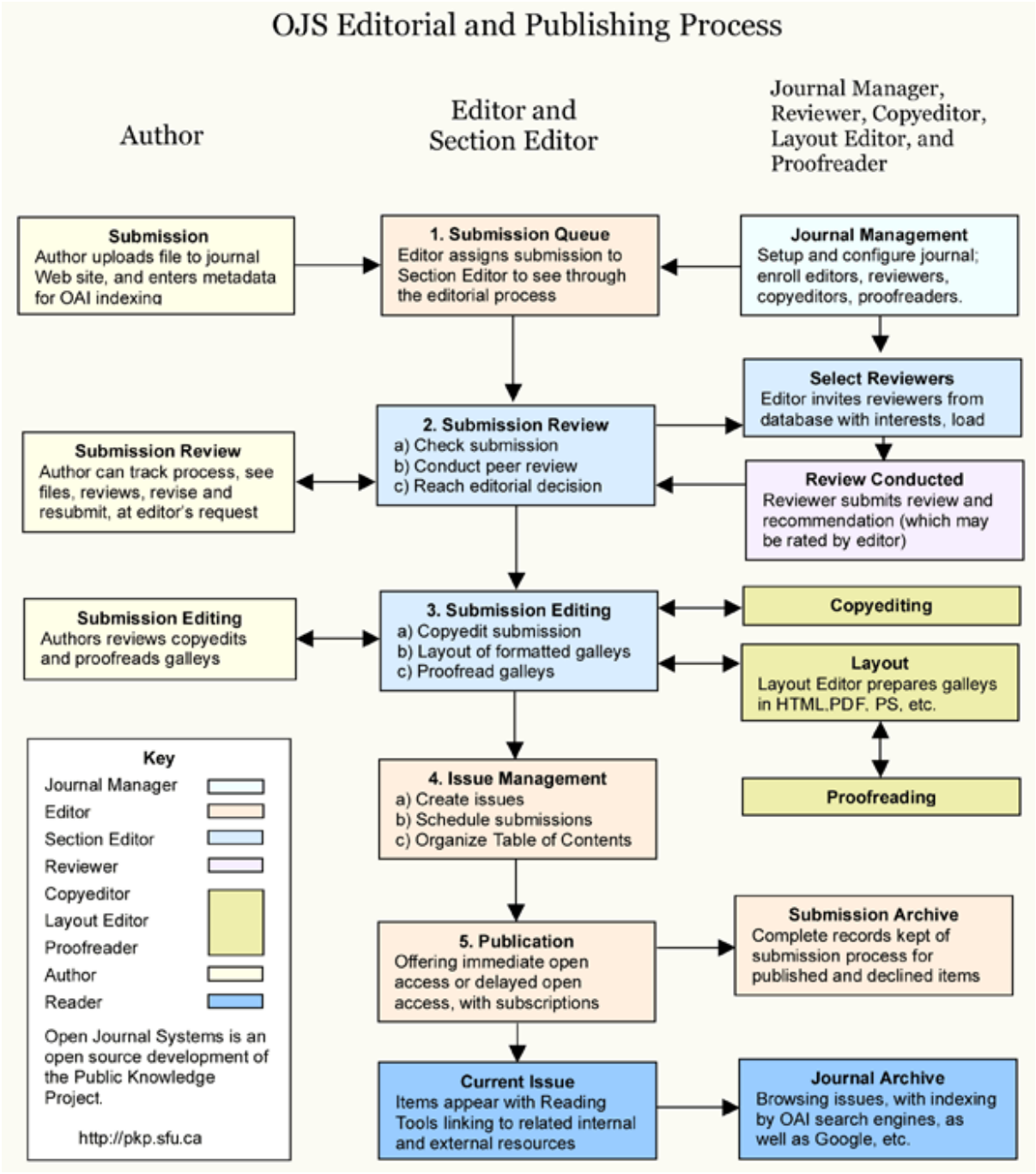

~IJAERS Workflow~

Important links:

Paper Submission Link:
https://ijaers.com/submit-paper/
Editorial Team:
https://ijaers.com/editorial-board/
Peer Review Process:
https://ijaers.com/peer-review-process/
Publication Ethics:
https://ijaers.com/publication-ethics-and-publication-malpractice-statement/
Author Guidelines:
https://ijaers.com/instruction-to-author/
Reviewer Guidelines:
https://ijaers.com/review-guidelines/

Journal Indexed and Abstracted in:

- Qualis-CAPES (A2)-Brazil
- Normatiza (Under Review-Ref.020191511)
- NAAS Score: 3.18
- Bielefeld Academic Search Engine(BASE)
- Aalborg University Library (Denmark)
- WorldCat: The World's Largest Library Catalog
- Semantic Scholar
- J-Gate
- Open J-Gate
- CORE-The world’s largest collection of open access research papers
- JURN
- Microsoft Academic Search
- Google Scholar
- Kopernio - powered by Web of Science
- Pol-Index
- PBN(Polish Scholarly Bibliography) Nauka Polaska
- Scilit, MDPI AG (Basel, Switzerland)
- Tyndale University College & Seminary
- Indiana Library WorldCat
- CrossRef DOI-10.22161/ijaers
- Neliti - Indonesia's Research Repository
- Journal TOC
- WIKI-CFP
- Scinapse- Academic Search Engine
- Mendeley-Reference Management Software & Researcher Network
- Dimensions.ai: Re-imagining discovery and access to research
- Index Copernicus Value(ICV): 81.49
- Citeseerx
- Massachusetts Institute of Technology (USA)
- Simpson University (USA)
- University of Louisville (USA)
- Biola University (USA)
- IE Library (Spain)
- Mount Saint Vincent University Library (Halifax, Nova Scotia Canada)
- University Of Arizona (USA)
- INDIANA UNIVERSITY-PURDUE UNIVERSITY INDIANAPOLIS (USA)
- Roderic Bowen Library and Archives (United Kingdom)
- University Library of Skövde (Sweden)
- Indiana University East (campuslibrary (USA))
- Tilburg University (The Netherlands)
- Williams College (USA)
- University of Connecticut (USA)
- Brandeis University (USA)
- Tufts University (USA)
- Boston University (USA)
- McGill University (Canada)
- Northeastern University (USA)
- BibSonomy-The blue social bookmark and publication sharing system
- Slide Share
- Academia
- Archive
- Scribd
- ISRJIF
- Cite Factor
- SJIF-InnoSpace
- ISSUU
- Research Bib
- infobaseindex
- I2OR
- DRJI journal-repository

AI Publication
International Journal of Advanced Engineering Research and Science (IJAERS)
104/108, Sector-10, Pratap Nagar, Jaipur, India